HOKKAIDO UNIVERSITY

Title	Study on Gas Separation Membrane Based on Covalent Organic Frameworks
Author(s)	加藤, 将貴
Degree Grantor	北海道大学
Degree Name	博士(工学)
Dissertation Number	甲第16379号
Issue Date	2025-03-25
DOI	https://doi.org/10.14943/doctoral.k16379
Doc URL	https://hdl.handle.net/2115/94888
Type	doctoral thesis
File Information	KATO_Masaki.pdf

Hokkaido University Collection of Scholarly and Academic Papers : HUSCAP

Doctoral thesis

Study on Gas Separation Membrane Based on Covalent Organic Frameworks

（共有結合性有機構造体を用いた気体分離膜に関する研究）

Masaki Kato

Graduate School of Chemical Sciences and Engineering,

Hokkaido University

Doctoral Supervisor: Prof. Toshihiro Shimada

Contents

Chapter 1 General Introduction

1.1 Separation of Substances

1.1.1 History and outline of separation

The separation of two or more mixtures into pure products has been performed since ancient times. It is estimated that balms, essences, and incense were produced by distillation in Mesopotamia approximately 4000 years ago [1]. Separation engineering is essential in modern chemical industries. For example, ultrapure water, which is necessary in the semiconductor industry, can be obtained through separation operations, such as membrane separation, distillation, and ion exchange.

Generally, the separation of mixtures does not proceed spontaneously because it is an entropy reduction process[2]. Therefore, it is necessary to apply energy, such as temperature or pressure, to the system or add a material that promotes separation. When the amount of energy input is reduced, the separation process becomes more efficient.

There are two main separation mechanisms, equilibrium and rate separation. The former includes distillation, extraction, and crystallization, whereas the latter includes sedimentation and membrane separation. Because each method has its advantages and disadvantages, it is important to select an appropriate method during the process.

1.1.2 Target of separation

Any mixture of the solid, liquid, and vapor phases can be targeted for separation. This thesis focuses on gas separation. For gas separation, the target gas must be extracted from a mixture of two or more gases. Table 1-1 summarizes the main target gas-mixture pairs and their sources. The separation of these gases can achieve several usefulness or reduce harmful effects.

Table 1-1. Typical separation targets for gas pairs [3–7].

Gas pairs	Target source	Composition
CO_2/N_2	Air	CO_2 400 ppm
	Fuel gas in post-combustion	CO_2 5–13%
CO_2/CH_4	Natural gas production	CO_2 30–40%
	Biogas production	CO_2 2–65%
O_2/N_2	Air	N_2 78 %
H_2/CH_4	Natural gas steam reforming	H_2 65–75%, CH_4 1–3%
H_2/CO_2	Water gas shift reaction	CO_2 36%
C_2H_4/C_3H_6	Naphtha decomposition	Ethylene (25–30%), propylene (15%)
VOC/N_2	Air	Trace level (10–100 ppb)

(1) CO_2

CO_2 has a large greenhouse effect, first proposed by Arrhenius in 1986. The large greenhouse effect of CO_2 is explained by the Fermi resonance between the symmetric stretch mode (1337 cm^{-1}) and the bending mode (667 cm^{-1})[8]. The resonance increased

the width of the bending mode peak, resulting in the absorption of wide range infrared wavelengths.

The concentration of CO_2 in the atmosphere increased from 280 ppm before the Industrial Revolution to 420 ppm by 2023[9]. This increase in concentration was quite influenced by the tremendous amount of CO_2 emissions by human activities (35.8 G tons in 2023[10]), inducing the global warming. The Intergovernmental Panel on Climate Change (IPCC) report in 2023 proposed several scenarios for the degree of increase in global average annual temperatures compared to pre-industrial times. The worst-case scenario (SSP5–8.5), i.e., the scenario in which no action is taken to address climate change, would result in an increase in the average annual global temperature of ca. 4.5 °C at 2100 (Fig. 1-1b) [11]. According to a report in 2018, if the average annual temperature increases by 2 °C in 2045, more than 1.5 billion people will be exposed to deadly heat waves and hundreds of millions of people will have contact with vector-borne diseases such as malaria [12]. Developed countries, including Japan, plan to balance the emission and removal of CO_2 from the atmosphere by approximately 2050. To achieve this goal, CO_2 capture and subsequent utilization or storage (CCUS) technologies are required. The effective CO_2 separation is important in this technique, including CO_2/N_2 separation from the post-combustion process[13], diluted CO_2 separation from the

atmosphere (direct air capture, DAC)[14], and CO_2/methane (CH_4) purification from natural gas or biogas[15].

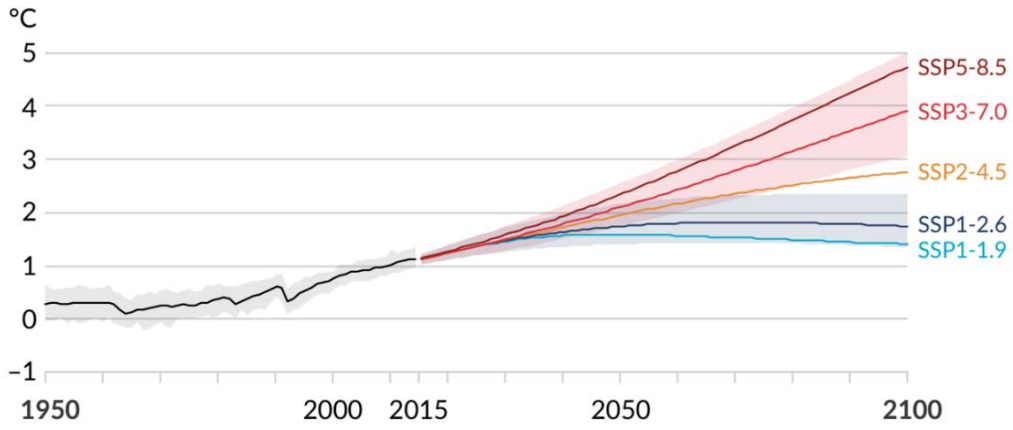

Fig. 1-1. Estimation of the increase in average annual temperature after the Industrial Revolution [2].

(2) Volatile organic compounds (VOC)

Volatile organic compounds (VOC), including toluene, chloroform, and ketone analogs, are widely used as solvents and fuels[16]. However, ingestion of large amounts of VOCs can cause health damage. For example, formaldehyde leakage from building materials in new constructions causes various illnesses, such as headaches and nausea, known as sick building syndrome[17]. In addition, it has been recognized as a major social problem in Japan when young workers at printing plants experience bile duct cancer due to long-term exposure to high concentrations of 1,2-dichloropropane vapor [18,19]. VOC are also harmful to the environment because they cause air pollution when decomposed by

light[20]. In order to reduce their hazardous effects, it is important to capture gaseous VOC from the exhaust gases.

1.1.3 Gas separation method

As mentioned above, separation of substances requires energy input. The worldwide total energy consumption reached 620 EJ (1 EJ = 10^{18} J) in 2023, 80% of which was generated by fossil fuels, including coal, oil, and natural gas [21], resulting in tremendous emission of CO_2. In Japan, the chemical industry accounts for 15% of CO_2 emissions from the industrial sector, and 40% of these emissions come from the separation process[22]. Thus, it is important to develop and choose energy-efficient gas separation methods for achieving a sustainable society. Typical gas separation methods are described below.

(1) Absorption separation

Absorption separation is a method of separating or concentrating a gas by absorbing it in an adsorbent. Adsorbents are mainly based on physical or chemical absorption. Physical adsorbents are generally chosen as porous materials, with pore diameters of ca. 0.2–2 nm such as porous carbon[23], zeolites[24], and metal organic frameworks (MOF)[25]. It is important to control the pore shape and size to increase gas adsorption

capacity and separation performance. In chemical absorption, gas is recovered by chemically reacting it with a specific gas to dissolve in an adsorbent. For the CO_2 separation from N_2–CO_2 mixture, alkali solutions[26], amine solutions[27–30], and ionic liquids[31,32] are often used. Pressure swing adsorption[33], vacuum swing adsorption[24,34,35], temperature swing adsorption[36,37], or a combination of temperature–pressure swings [38,39] are typically used to recover gases.

(2) Cryogenic separation

Cryogenic separation is a method of liquefying a multicomponent gas mixture by compression, cooling, and expansion, and separating each component in the gas mixture using distillation and condensation operations[39,40]. This method is industrially used for the production of medical oxygen from air[41]. A disadvantage of this method is the difficulty in separating gases with similar boiling points.

(3) Membrane separation

In membrane separation methods, a mixture of gases is separated based on the difference in the permeation rate through the membrane of each component[42]. The permeation rate can be controlled by the physical and chemical properties of the membrane materials.

In principle, the membrane separation method can separate gases using only a small differential pressure between the membranes. This is the advantage of saving energy and reducing the size of the facilities compared to other methods.

1.1.4 History of membrane gas separation

Figure 1-2 summarizes the historical milestones in membrane separation[43]. The theory of mass transport through boundary layers, which is a fundamental concept in membrane separation, began with Fick's law in 1855 and Thomas Graham's formulation of the solution–diffusion mechanism in 1866. During the 1960s–1980s, scientists gained much data about the correlations between the structure and gas permeation properties of membranes. In the 1980s, Monsanto Prism Corp. first achieved industrial commercialization of a membrane gas separation system for hydrogen purification [44]. In the 21st century, the development of CO_2 capture [45] or hydrogen production [46] using membrane separation techniques has attracted much attention due to the consideration of suppressing climate change caused by global warming. Gas separation membranes with various structures, geometries, and transport mechanisms are currently being developed. Figure 1-3 shows the classification of the membranes and membrane serration processes[47].

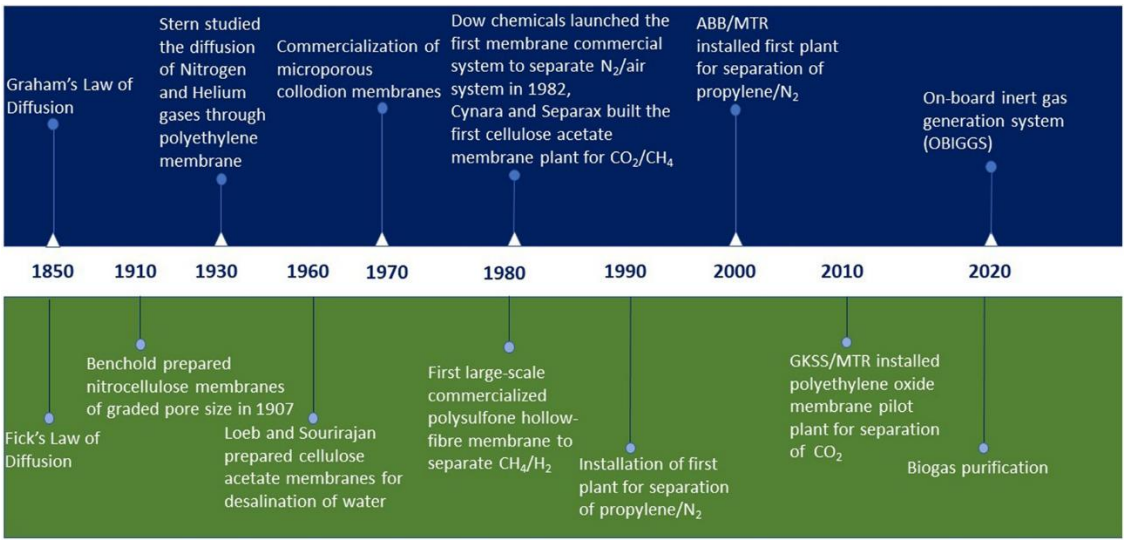

Fig. 1-2. Progress of the membrane separation system. This figure was reproduced from Ref. [43], with permission.

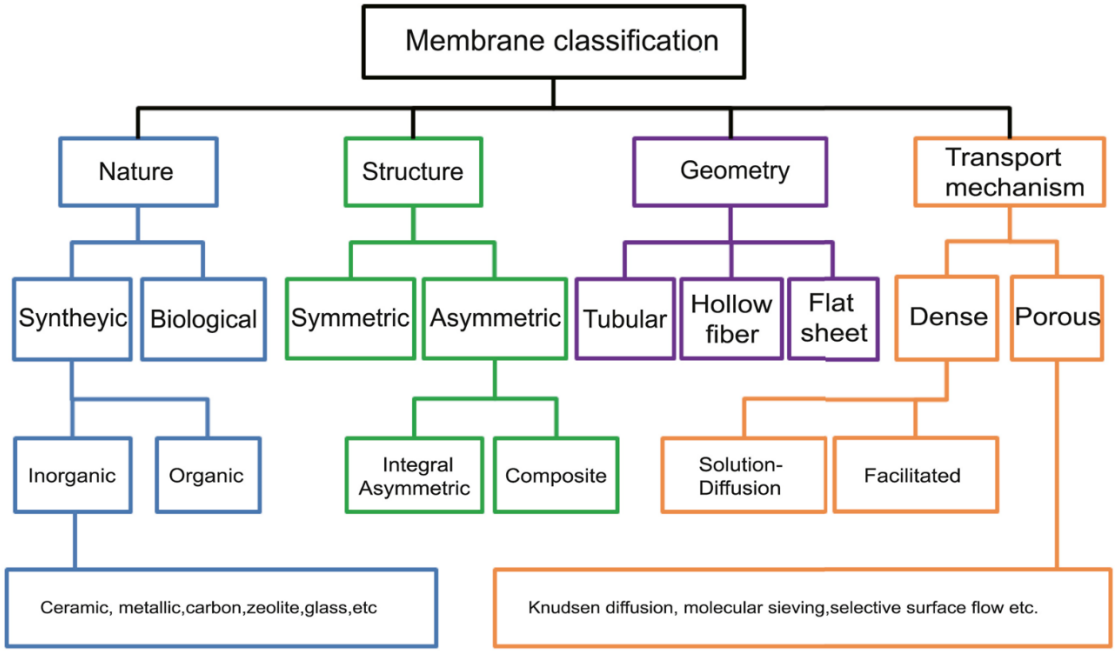

Fig. 1-3. Classification of the membrane and membrane separation processes. This figure was reproduced from Ref.[47], with permission.

1.1.5 Mechanism of membrane gas separation

The membrane gas separation mechanism is mainly based on two materials: porous and nonporous membranes. The gas-permeation mechanism of the former membrane depends on the pore size. When the pore size was sufficiently greater than the mean free path of the gas with laminar flow (Hagen–Poiseuille flow) permeation, the membrane could not separate the gas mixture (Fig. 1-4a). The pore diameter is ca. 2–50 nm, which is not negligible for the mean free path, and the gas permeation follows the Knudsen flow (Fig. 1-4b). In this case, the gas separation performance can be described as being inversely proportional to the square root of the molecular weight, e.g., $\sqrt{(16/44)} = 0.6$ for CO_2–CH_4 separation[48]. Furthermore, as the pore size decreases, the molecules adsorbed on the pore surface affect the permeation properties (surface diffusion). The gas permeability of *P* can be described by Eq. (1.1)

$$P = P_s + P_K + P_H \tag{1.1}$$

where P_s, P_K, and P_H are the gas permeabilities of the surface, Knudsen, and Hagen–Poiseuille flows, respectively. When P_s is negligible, *P* can be described using Eq. (1.2).

$$P = \frac{\varepsilon}{RTq}\left(\frac{2r}{3}\sqrt{\frac{8RT}{\pi M}} + \frac{r^2}{8\mu}p_{\mathrm{av}}\right) \tag{1.2}$$

where ε is the porosity, R is the gas constant, T is the absolute temperature, q is the

tortuosity, r is the pore radius, p_{av} is the average pressure, μ is the viscosity, and M is the molecular weight. When the pore size becomes even smaller than that of the gas molecules, the membrane can separate the gas mixtures depending on their differences in size, which is known as the molecular sieve effect (Fig. 1-4c).

On the other hand, nonporous membranes, such as polymeric or liquid membranes, can permeate gases via a solution–diffusion mechanism (Fig. 1-4d) [49]. In the solution–diffusion mechanism, gas permeation through the membrane occurs in the following three steps: 1) the feed gas arrives at the membrane surface and dissolves into the membrane; 2) the dissolved gas diffuses through the membrane along with the pressure difference between the membranes; and 3) the gas arrived at the low-pressure side, then desorbed. Gas permeability (P) can be expressed as the product of solubility (S) and diffusivity (D), as shown in Eq. (1.3).

$$P = S \times D \tag{1.3}$$

The permeation mechanism becomes more complicated when it is necessary to consider permeation through both pore and non-pore regions. One of the simplest formulations is dual-site sorption with a partial immobilization model (Fig. 1-4e) [50,51]. In the dual-site sorption model, Henry sorption (C_{D}) is the main mechanism of sorption into the matrix component, whereas Langmuir sorption (C_{H}) governed sorption into the

microvoid region [52]. The gas concentration in the polymer membrane (C) was expressed as their sum.

$$C = C_{\mathrm{D}} + C_{\mathrm{H}} = k_{\mathrm{D}} p + \frac{C'_{\mathrm{H}} bp}{1 + bp} \tag{1.4}$$

where k_{D} is the Henry's law constant, p is the feed gas pressure, C'_{H} is the Langmuir capacity of the voids, and b is the Langmuir affinity constant. The gas solubility coefficient (S) is expressed by Eq. (1.5):

$$S = \frac{C}{p} = k_{\mathrm{D}} + \frac{C'_{\mathrm{H}} b}{1 + bp} \tag{1.5}$$

When a gas diffuses into a polymer membrane, both Henry and Langmuir diffusion mechanisms are considered. It was assumed that the gas species trapped in the Langmuir site were relatively mobile in the polymer (partial immobilization). When the concentration of gas in the polymer membrane is estimated using Eq. (3.4), and Fick's first law is described by Eq. (1.6):

$$J = -D_{\mathrm{D}} \frac{\partial C_{\mathrm{D}}}{\partial x} - D_{\mathrm{H}} \frac{\partial C_{\mathrm{H}}}{\partial x} = -D_{\mathrm{D}} \left(\frac{1 + \frac{FK}{(1 + bp)^2}}{1 + \frac{K}{(1 + bp)^2}} \right) \frac{\partial C}{\partial x} \tag{1.6}$$

where J is the flux of the gas species, D_{D} and D_{H} are the diffusion coefficients under the Henry and Langmuir modes, respectively, F is the ratio of D_{D} and D_{H} ($D_{\mathrm{D}}/D_{\mathrm{H}}$), and K is equal to $C'_{\mathrm{H}} b/k_{\mathrm{D}}$.

By using Eq. (3.6), and Fick's second law is described by Eq. (1.7):

$$\frac{\partial C}{\partial t} = \frac{\partial J}{\partial x} = \frac{\partial}{\partial x}\left(-D_{\mathrm{D}} \left(\frac{1 + \dfrac{FK}{(1+bp)^2}}{1 + \dfrac{K}{(1+bp)^2}} \right) \frac{\partial C}{\partial x} \right) \tag{1.7}$$

Since P, D, S have the relationship of $P = D \times S$ (Eq.(1.3)), the average permeability (P_{a}) of the membrane is given by Eq. (1.8).

$$P_{\mathrm{a}} = D \times S = D_{\mathrm{D}} \left(\frac{1 + \dfrac{FK}{1+bp}}{1 + \dfrac{K}{1+bp}} \right) \times \left(k_{\mathrm{D}} + \frac{C_{\mathrm{H}}' b}{1+bp} \right) = k_{\mathrm{D}} D_{\mathrm{D}} \left(1 + \frac{FK}{1+bp} \right) \tag{1.8}$$

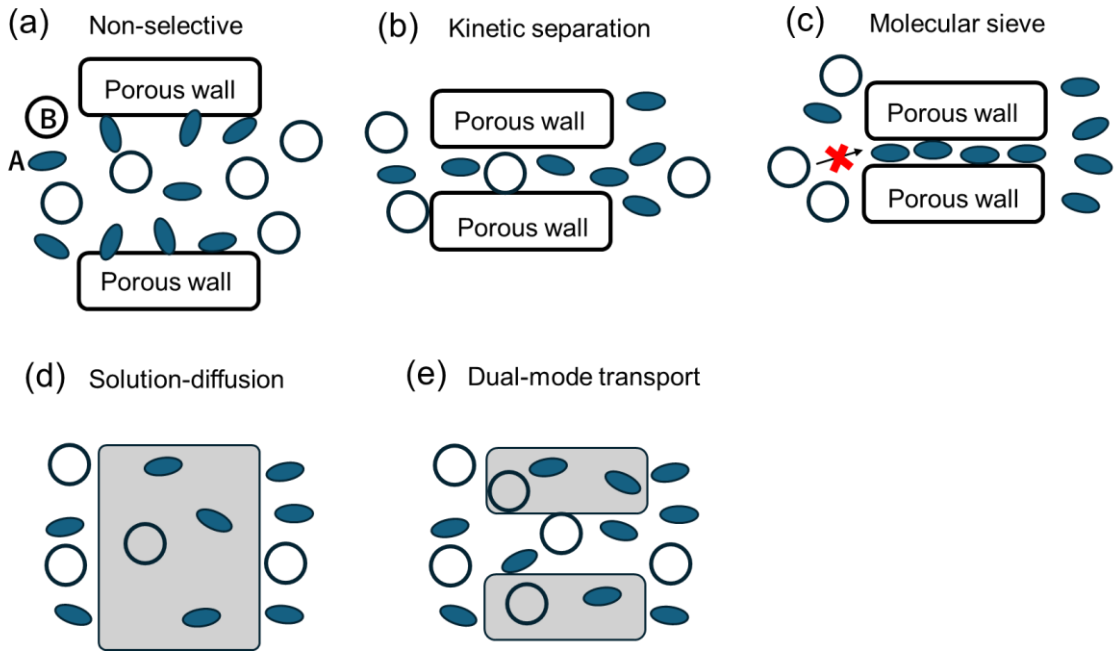

Fig. 1-4. Various gas permeation mechanisms. Porous membranes with a pore diameter (a) large enough (ca. <100 nm), (b) meso-size (2–50 nm), and nano-sized (below the size of the gas). Dense membranes (d) without and (e) with pores.

Gas separation membranes based on the following mechanisms have also been proposed: facilitated transport membranes exhibit high CO_2 separation performance [53–

56]. CO_2 reacts with the primary or secondary amines anchored to the membrane skeleton (Eq. (1.9) to (1.11)) [57].

$$CO_2 + RR'NH \rightleftharpoons RR'NH^+COO^- \quad (1.9)$$

$$RR'NH^+COO^- + RR'NH \rightleftharpoons RR'NCOO^- + RR'NH_2^+ \quad (1.10)$$

$$RR'NH^+COO^- + H_2O \rightleftharpoons RR'NCOO^- + H_3O^+ \quad (1.11)$$

where R is the alkyl group and R' is the alkyl group or hydrogen. This reaction increased the solubility of CO_2 in the membranes. The CO_2 diffuses through the membrane by "hopping" mechanism on amine functional groups, achieving greater CO_2 permeability than other gases such as N_2 or CH_4.

The "trap door" effect is also known as a type of zeolite called Chabazite. Cs (cesium) ions were arranged to block the center of the –O–Si–O– octagonal face of the zeolite backbone. When CO_2 approaches, Cs^+ repositions itself from the octagonal center, allowing CO_2 to pass through the pores [58]. Unfortunately, this method was not applied to membrane-based separation in 2024 because of a lack of development in the membrane preparation process.

The "gate-opening" effect is also a promising mechanism for high-performance gas separation applications [59]. Under the gate-opening effect, the CO_2 absorption

capacity changes drastically when the operating pressure increases. A composite membrane of a gate-opening MOF and graphene oxide has been reported to significantly improve CO_2/N_2 separation above the threshold pressure [60]. The construction of a CO_2 capture system based on an MOF with a gate opening effect was carried out by the New Energy and Industrial Technology Development Organization (NEDO) in Japan [61]. To achieve good gas separation properties, it is important to have a moderate degree of structural freedom.

1.1.6 Measurement of gas permeation performances

It is essential to measure the gas permeation performance of the membranes accurately. When the gas permeation rate is sufficiently high, classical methods, such as the Gurley or Frazier method, can be applied. When a highly sensitive method is necessary to evaluate the performance of membranes with low gas permeation, differential pressure, and equal pressure methods are often used to achieve this aim.

In the differential pressure method, a membrane is mounted in a test cell; one side is pressurized with gas, and the other side is depressurized, thereby creating a differential pressure on the membrane. The pressure difference acts as a driving force that allows gas to permeate the membrane. The basic arrangement of the apparatus is shown in Fig.

1-5. The typical measurement procedure is described as follows: (1) After valves B, C, D, and E were opened, the entire system was evacuated by a vacuum pump. (2) After evacuation, valves B and C are closed. (3) Gas or vapor is introduced into the gas manifold (A) using a mass flow controller (MFC). (4) Valves D and E were closed to disconnect from the vacuum pump. (5) Valve B was opened simultaneously to introduce the gas into one side of the membrane, while the pressure in the measurement room (F) was recorded. The variable leak valve (H) was opened slightly to analyze the gas composition ratio using a mass spectrometer.

A typical gas permeation curve in the measuring room (F) is shown in Fig. 1-6. From the slope of the curve dP/dt at steady state, the gas permeability coefficient (P) can be calculated using the following equation:

$$P = \frac{Vl}{A\Delta pRT}\left(\frac{\mathrm{d}P}{\mathrm{d}t}\right) \tag{1.12}$$

where V is the volume of the measurement room, A is the membrane area, l is the membrane thickness, Δp is the transmembrane pressure, R is the gas constant (8.31 J K^{-1} mol^{-1}), and T is the absolute temperature. dP/dt is the pressure increase per unit of time in the measuring room (F). Gas permeability is conventionally expressed using the "Barrer" unit named after the British scientist R. M. Barrer [104]. Gas permeance, which is not normalized by film thickness, is expressed in units of a Gas Permeance Unit

(GPU). The conversion of these units is as follows:

$$\mathrm{GPU} = 10^{-6} \times \frac{\mathrm{cm}^3(\mathrm{STP})}{\mathrm{cm}^2 \cdot \mathrm{s} \cdot \mathrm{cmHg}} = \frac{\mathrm{Barrer}}{\mu\mathrm{m}} = 7.5 \times 10^{-12} \times \frac{\mathrm{m}^3(\mathrm{STP})}{\mathrm{m}^2 \cdot \mathrm{s} \cdot \mathrm{Pa}} \qquad (1.13)$$

The gas diffusivity (D) can be calculated by the following eq.

$$D = \frac{l^2}{6\theta} \qquad (1.14)$$

The gas solubility (S) was estimated using Eq. (1.3), (1.12), and (1.14).

When the interaction between the target gas pairs was negligibly low, the gas selectivity was estimated by the ratio of the pure gas permeability between the gas pairs. This ratio is called the ideal gas selectivity and is calculated as follows (Eq. (1.15))

$$\text{Ideal selectivity} = \frac{P_\mathrm{A}}{P_\mathrm{B}} \qquad (1.15)$$

where P_A and P_B are the permeances of each gas pair. If the permeability of gases A and B are independent, their mixture selectivity can be estimated by Eq. (1.15).

When the gas mixture permeated through the membrane, the gas separation factor α was calculated as follows (Eq: (1.16))

$$\alpha = \frac{y_A/y_B}{x_A/x_B} \qquad (1.16)$$

where $y_\mathrm{A}/y_\mathrm{B}$ and $x_\mathrm{A}/x_\mathrm{B}$ are the molar fraction ratios of the permeate and feed sides, respectively.

The permeated gas composition was determined using gas chromatography in the

equimolar method. This method can be applied to membranes with low-pressure durability. However, gas solubility and diffusivity cannot be directly measured.

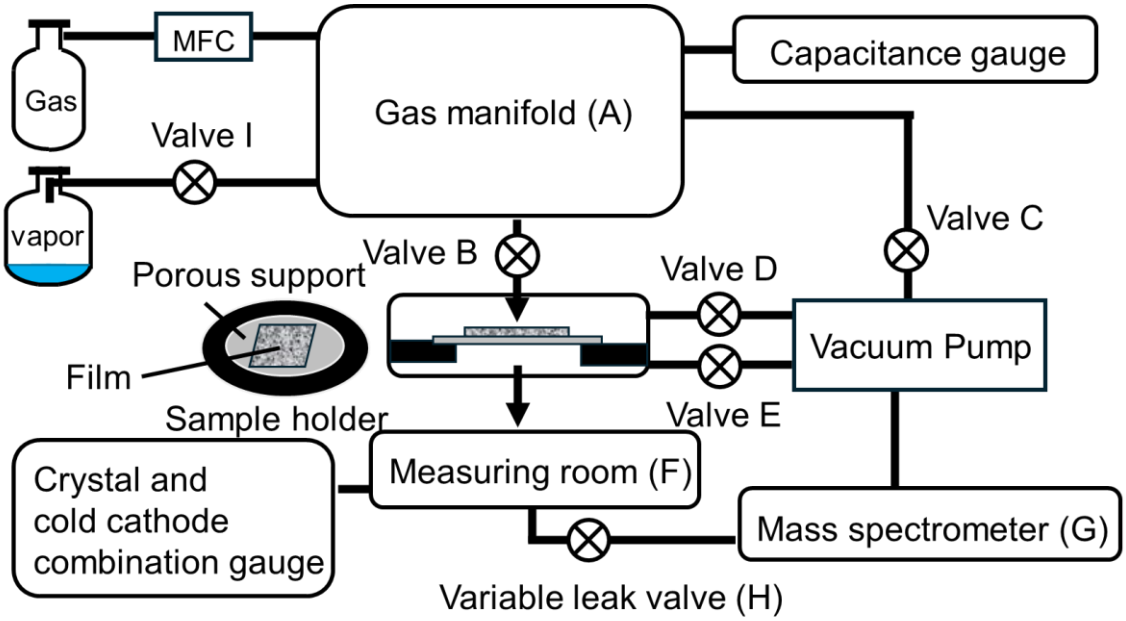

Fig. 1-5. Typical arrangement of gas permeation apparatus.

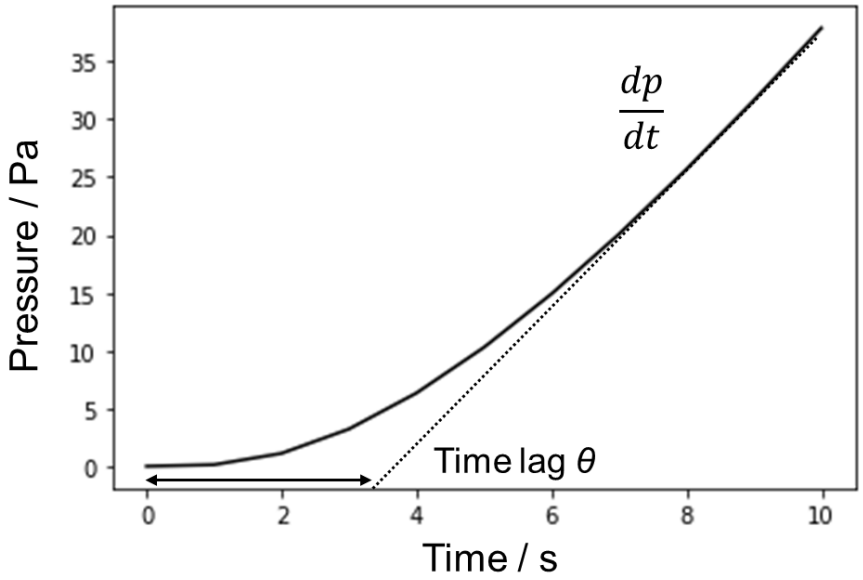

Fig. 1-6. Gas permeation curve in the measuring room (F).

1.1.7 Limitation of conventional polymer-based gas separation membranes

Polymers are the most widely used materials for gas-separation membranes [43]. However, they have the inherent characteristic of a trade-off between gas permeability and selectivity. This relationship was defined as "Robeson's upper bound," named after the proposer of L. M. Robeson. This bound is based on the activation energy theory related to gas molecular diameters and updated as the progress of performance for the polymeric membranes [62,63]. Figures 1-7 shows the latest upper bounds for O_2/N_2, H_2/N_2, CO_2/N_2, and CO_2/CH_4 separations reported in 2019 (red lines).

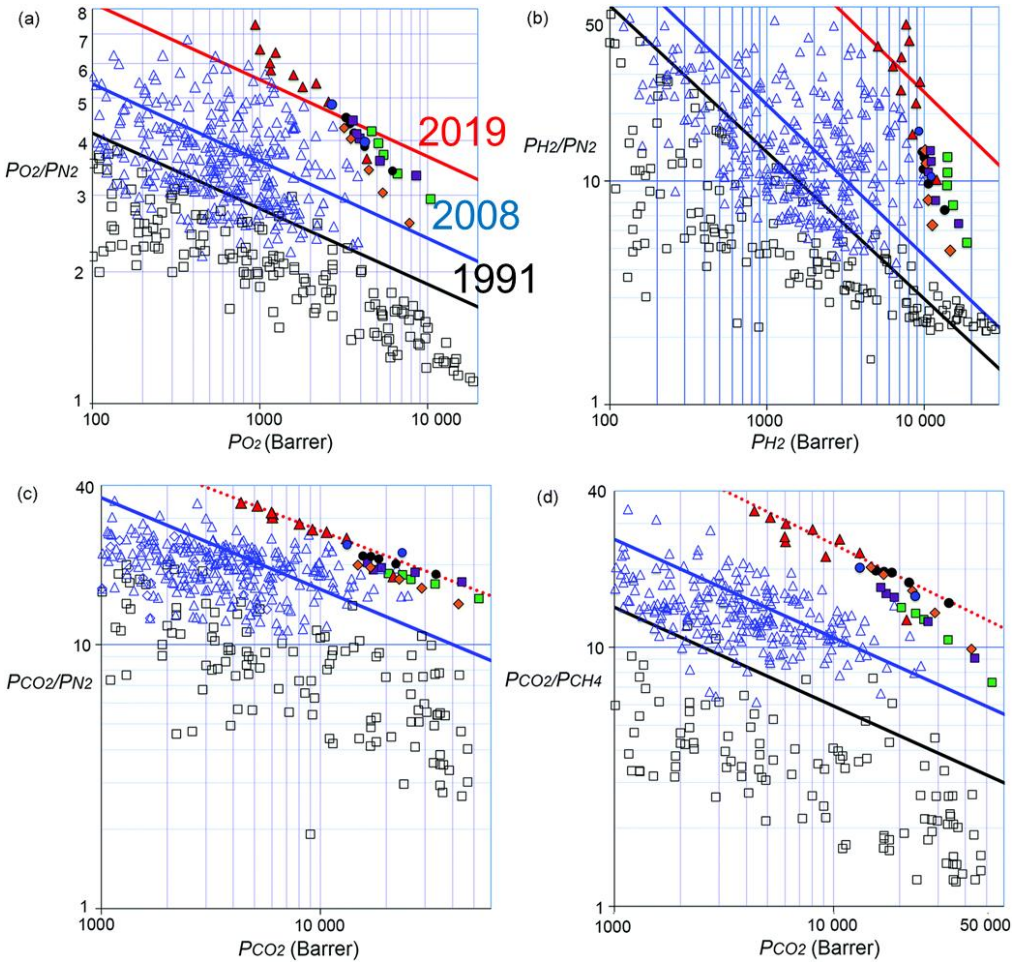

Fig. 1-7. The polymer upper bound for (a) O_2/N_2, (b) H_2/N_2, (c) CO_2/N_2, and (e) CO_2/CH_4 separation. The red, blue, and black lines represent the polymer upper bound in 2019, 2008, and 1991, respectively. The closed symbols represent polymer of intrinsic microporosity (PIM) related films, which are PIM–BTrip (▲), PIM–TMN–Trip (■), PIM–HMI–Trip (■), PIM–DM–BTrip (●), PIM–TFM–BTrip (●) and PIM–DTFM–BTrip (◆). Those data were reported after 2008. The closed symbols show non-PIM polymers (□) and previously reported PIMs (△). Figures were reproduced from Ref.[62].

1.1.8 Membrane materials for improving the gas separation performance

Many researchers have been exploring new membrane materials to overcome this upper bound. Some of these are as follows:

Liquid materials are widely developed by designing the improvement of gas

permeability by increasing gas solubility. Ionic liquids, which are liquid salts at room temperature, allow gas permeability to be controlled by designing their cations and anions, thus various structures of ionic liquids are being investigated for gas separation membrane[64–66]. It is necessary to immobilize the ionic liquid on a support such as a porous material, but stability is often an issue, such as leakage of ionic liquid due to high feed gas pressure.

Porous materials with oriented pore channels are also crucial for the design of high-performance gas-separation membranes. Zeolites are well-known inorganic porous membranes. Zeolite is an aluminosilicate material composed of 0.1 to several nanometer-diameter pores, which exhibit excellent corrosion and mechanical stability. Several zeolite membranes, such as Y-type [67] and DDR-type [68] membranes, have been synthesized, and some of them have been commercialized as gas separation membranes. MOFs with various structures have also been proposed as gas-separation membranes [69]. The design of ligands and central metal ions is essential for improving the gas separation performance of MOF membranes. Some of these materials exhibit very high gas separation and permeation performances, exceeding the upper bound. However, their rigid frameworks tend to form rigid crystals, which can generate grain boundaries that act as gas leakage pathways[70]. Thus, the development of defect-free membranes

remains a challenge. Recently, porous organic materials named as covalent organic frameworks (COF) have also been developed.

Composite materials are also important research topics. Mixed-matrix membranes are composite materials that disperse fillers into a polymeric matrix [71]. The performance of the membrane can be significantly controlled by changing the physical and chemical properties of the fillers or matrices [72,73]. When an excess filler is loaded into the matrix, the interfacial compatibility between the filler and matrix decreases, resulting in a decrease in gas separation performance.

1.2 Covalent Organic Frameworks (COF)

1.2.1 History and outline of COF

COF is a relatively new organic material, first reported in 2005 by O. M. Yaghi and co-workers[74]. It has a crystalline, flexibly oriented pore architecture composed of organic building blocks arranged by covalent bonds[75]. It is synthesized by arranging highly symmetric precursors, such as C_2, C_3, and C_4 symmetries, into geometric pore architectures (Fig. 1-8a). These precursors are linked by dynamic and reversible covalent bonds such as boronic esters, imines, and imides (Fig. 1-8b). COF skeletons can be arbitrarily designed by modifying the precursor molecules, allowing us to control their

physical and chemical properties for designated applications, such as catalysts[76,77], actuators[78,79], or molecular separation[80–83].

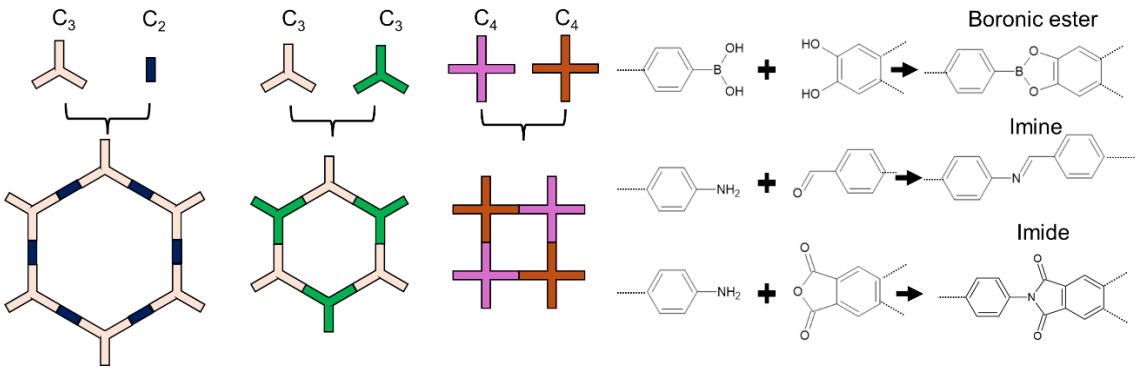

Fig. 1-8 (a) Schematic illustration of the geometric architecture of COF and its precursors. (b) Typical covalent bonds for COF formation reaction.

1.2.2 Preparation of COF-based membranes

COF is usually obtained by an organic synthetic method (hydrothermal synthesis). However, synthesizing COF as a thin film for applications such as separation membranes is still a very challenging task because such powders are insoluble in almost all solvents.

There are two methods for preparing COF films: MMM and neat COF membranes. The former can be synthesized easily; however, as mentioned above, the interfacial compatibility between the COF filler and the polymer membrane is still an inevitable problem. In addition, the MMM did not evaluate the gas permeation properties of the pure COF. Therefore, the synthesis of COF as neat membranes is critical from two points of view: application of COF and exploration of their fundamental properties. Typical

synthesis methods for neat COF membranes are summarized in Table 1-2.

Table 1-2. Synthesis method of COF films

Method	Name	Substrate	Thickness	Application	Ref.
CVD with solvent vapor	PyTTA–TPA COF	Si/SiO_2, Cu, ITO	ca. 10–5 nm	OFET	[84]
Liquid–liquid interfacial polymerization	Tp–Bpy COF	Free-standing	ca. 50–200 nm	Dye separation	[85]
Solvothermal synthesis	COF-5	SLG/SiO_2, Cu or SiC	ca. 70–200 nm	None	[86]
Flow synthesis	HHTP-based COF	Au (QCM)	20–100 nm	None	[87]
Air–water interfacial synthesis	2DPI	Free-standing	~2 nm (ca. five layers)	None	[88]
Monomer-exchange	TAPT–DHTA	ITO glass	10 μm	Electrolyte membrane	[89]
Solid–vapor interfacial polymerization	TFP–PDA	Si/SiO_2	120 nm	Dye separation	[90]
Electrochemical method	TAPB–PDA COF	ITO	~100 μm	None	[91]
Vacuum deposition	COF-1	Ag (111)	Single layer	None	[92]

1.2.3 Membrane gas separation application of the COF

COF are promising candidates for highly permeable and selective gas separation membranes. Computational simulations have reported that COF membranes with specific porous characteristics exhibit good CO_2 separation performance, which exceeds the upper

bound of conventional polymeric membranes [93]. The experimentally evaluated gas-separation properties of the COF membranes are summarized in Table 1-3.

Table 1-3. Experimental gas separation properties of COF membranes

Name	Synthesis method	Target gas	Faster gas permeability / Barrer	Selectivity	Ref.
$TpTG_{Cl}$@TpPa–SO_3H	Liquid–liquid interface	H_2/CO_2 H_2/N_2 H_2/CH_4	361	28 36 48	[80]
COF–LZU1–ACOF-1	Solvothermal	H_2/CO_2 H_2/N_2 H_2/CH_4	658	24 84 100	[82]
NCOFM-0	Liquid–liquid interface	CO_2/N_2 CO_2/CH_4	36.8	80 54	[83]
ACOF-1	Solvothermal	CO_2/CH_4	56.6	97.1	[94]
TpHz COF	Counter-diffusion	CO_2/N_2	20.6	0.79	[95]
TpAzo	Liquid–liquid interface	CO_2/N_2	44.9	1	[96]
TpEBr@TpPa–SO_3Na iCON	Air–liquid interface	H_2/CO_2 H_2/N_2 H_2/CH_4	121	26.2 40.5 74.2	[97]
DhaTGAsp-X	Liquid–liquid interface	CO_2/CH_4	33.0	49	[98]
Vertically aligned COF–LZU1	Solvothermal	H_2/CO_2 H_2/CH_4 H_2/C_3H_6 H_2/C_3H_8	7270	31.6 29.5 90.9 119.5	[99]
LA-α-CD–TpPa-1	Liquid–liquid interface	H_2/CO_2 H_2/CH_4 H_2/C_3H_6 H_2/C_3H_8	4600	36.2 39.4 157.8 187.1	[100]

TpPa-1 SSSN TpPa-2 SSSN TpHz SSSN	Hot drop coating	CO_2/H_2	5.0 3.2 0.9	8.6 21 9.9	[101]
PATA	Assembly-dissociation-reconstruction	CO_2/N_2	975	30.6	[102]

However, experimental exploration of the gas separation performance of COF membranes has yet to be sufficiently examined due to the difficulty in synthesizing neat COF membranes as following problems.

(1) Solvothermal or continuous flow methods cannot prepare free-standing films because they require specific substrates, such as Si/SiO_2 or Au, to grow uniform films [84,87].

(2) Free-standing COF films can be obtained using interfacial synthesis methods [78,85,103]. Gas separation membranes require extremely thin films with no gas leakage; however, it is difficult to precisely control their thickness to less than 100 nm on a wafer scale without defects.

1.3 Motivation and Organization of This Thesis

The motivation for this thesis is to investigate new materials for gas-separation membranes. I have focused on COF-based separation membranes, which are expected to exhibit excellent gas permeation properties. However, their gas separation mechanisms still need to be sufficiently elucidated due to the difficulty in preparing neat COF membranes. Using molecular-level experiments and simulations, I will develop a new preparation method for COF membranes and reveal their transportation mechanisms for various gases.

The structure of this thesis is as follows. Chapter 1 provides a general introduction to the position and purpose of this thesis. Chapter 2 considers the thermodynamic efficiency of gas separation membranes using numerical calculations. The membrane separation method was found to have greater thermodynamic efficiency than the other methods under certain conditions. Chapter 3 discusses the development of a new synthesis method for COF films and the evaluation of their CO_2/N_2 separation performances. Chapter 4 describes the crystallization of COF films using the solvent vapor annealing method and assessing their CO_2/CH_4 separation properties. Chapter 5 discusses the evaluation of the separation performance of fluorinated COF films for separating volatile organic compounds (VOC) vapor. Finally, Chapter 6 presents a general conclusion.

References

[1] I.C. Lda, History of alcohol distillation, (2021). https://www.copper-alembic.com/en/page/history-of-alcohol-distillation (accessed October 29, 2024).

[2] 化学工学会分離プロセス部会, 分離プロセス工学の基礎, (2009).

[3] D.M. D'Alessandro, B. Smit, J.R. Long, Carbon dioxide capture: prospects for new materials, Angew. Chem. Int. Ed Engl. 49 (2010) 6058–6082.

[4] C.Y. Chuah, K. Goh, Y. Yang, H. Gong, W. Li, H.E. Karahan, M.D. Guiver, R. Wang, T.-H. Bae, Harnessing filler materials for enhancing biogas separation membranes, Chem. Rev. 118 (2018) 8655–8769.

[5] W.J. Martinez-Burgos, E. de Souza Candeo, A.B. Pedroni Medeiros, J. Cesar de Carvalho, V. Oliveira de Andrade Tanobe, C.R. Soccol, E.B. Sydney, Hydrogen: Current advances and patented technologies of its renewable production, J. Clean. Prod. 286 (2021) 124970.

[6] F.D. Mango, The light hydrocarbons in petroleum: a critical review, Org. Geochem. 26 (1997) 417–440.

[7] X. Zhao, Y. Chen, Q. Ding, T. Xiao, X. Yang, High-performance silicone membranes for VOC/N_2 separation: A new crosslinking strategy via octyl-grafted poly(hydromethylsiloxane), Ind. Eng. Chem. Res. 62 (2023) 13974–13987.

[8] R. Wordsworth, J.T. Seeley, K.P. Shine, Fermi resonance and the quantum mechanical basis of global warming, Planet. Sci. J. 5 (2024) 67.

[9] 気象庁, 大気中二酸化炭素濃度の経年変化, (2024). https://www.data.jma.go.jp/ghg/kanshi/ghgp/co2_trend.html (accessed November 21, 2024).

[10] Jircas, 2023 年の温室効果ガス排出量と気候政策, JIRCAS, (2024). https://www.jircas.go.jp/ja/program/proc/blog/20240412 (accessed November 21, 2024).

[11] IPCC, Synthesis report: Climate change 2023, (2023).

[12] Y. Xu, V. Ramanathan, D.G. Victor, Global warming will happen faster than we think, Nature 564 (2018) 30–32.

[13] A. Samanta, A. Zhao, G.K.H. Shimizu, P. Sarkar, R. Gupta, Post-combustion CO_2

capture using solid sorbents: A review, Ind. Eng. Chem. Res. 51 (2012) 1438–1463.

[14] A. Kumar, D.G. Madden, M. Lusi, K.-J. Chen, E.A. Daniels, T. Curtin, J.J. Perry 4th, M.J. Zaworotko, Direct air capture of CO_2 by physisorbent materials, Angew. Chem. Int. Ed Engl. 54 (2015) 14372–14377.

[15] Y. Zhang, J. Sunarso, S. Liu, R. Wang, Current status and development of membranes for CO_2/CH_4 separation: A review, Int. J. Greenhouse Gas Control 12 (2013) 84–107.

[16] O. Us Epa, What are volatile organic compounds (VOCs)?, (2019). https://www.epa.gov/indoor-air-quality-iaq/what-are-volatile-organic-compounds-vocs (accessed September 20, 2024).

[17] Seki A., Takigawa T., Kishi R., Sakabe K., Torii S., Tanaka M., Yoshimura T., Morimoto K., Katoh T., Kira S., Aizawa Y., Review of sick house syndrome, Nihon Eiseigaku Zasshi 62 (2007) 939–948.

[18] Y. Toyoda, T. Takada, H. Suzuki, Halogenated hydrocarbon solvent-related cholangiocarcinoma risk: biliary excretion of glutathione conjugates of 1,2-dichloropropane evidenced by untargeted metabolomics analysis, Sci. Rep. 6 (2016) 24586.

[19] S. Kubo, Y. Nakanuma, S. Takemura, C. Sakata, Y. Urata, A. Nozawa, T. Nishioka, M. Kinoshita, G. Hamano, H. Terajima, G. Tachiyama, Y. Matsumura, T. Yamada, H. Tanaka, S. Nakamori, A. Arimoto, N. Kawada, M. Fujikawa, H. Fujishima, Y. Sugawara, S. Tanaka, H. Toyokawa, Y. Kuwae, M. Ohsawa, S. Uehara, K.K. Sato, T. Hayashi, G. Endo, Case series of 17 patients with cholangiocarcinoma among young adult workers of a printing company in Japan, J. Hepatobiliary Pancreat. Sci. 21 (2014) 479–488.

[20] A. Mangotra, S.K. Singh, Volatile organic compounds: A threat to the environment and health hazards to living organisms - A review, J. Biotechnol. 382 (2024) 51–69.

[21] Energy institute, Statistical review of world energy, 2024.

[22] 経済産業省, 2050 年カーボンニュートラルに向けた我が国の課題と取組, (2022). https://www.enecho.meti.go.jp/about/whitepaper/2021/html/1-2-3.html#:~:text=日本が排出する温室,123-1-1）。 (accessed December 23,

2024).

[23] S. Wang, Z. Su, X. Lu, Energy-consumption analysis of carbon-based material for CO_2 capture process, Fluid Phase Equilib. 510 (2020) 112504.

[24] S.M.W. Wilson, F.H. Tezel, Direct dry air capture of CO_2 using VTSA with faujasite zeolites, Ind. Eng. Chem. Res. 59 (2020) 8783–8794.

[25] H. Furukawa, K.E. Cordova, M. O'Keeffe, O.M. Yaghi, The chemistry and applications of metal-organic frameworks, Science 341 (2013) 1230444.

[26] Z. Zolfaghari, A. Aslani, R. Zahedi, S. Kazzazi, Simulation of carbon dioxide direct air capture plant using potassium hydroxide aqueous solution: Energy optimization and CO_2 purity enhancement, Energy Conversion and Management: X 21 (2024) 100489.

[27] G.T. Rochelle, Amine scrubbing for CO_2 capture, Science 325 (2009) 1652–1654.

[28] N. Matsumiya, M. Teramoto, S. Kitada, H. Matsuyama, Evaluation of energy consumption for separation of CO_2 in flue gas by hollow fiber facilitated transport membrane module with permeation of amine solution, Sep. Purif. Technol. 46 (2005) 26–32.

[29] N. Wang, Z. Peng, H. Gao, T. Sema, J. Shi, Z. Liang, New insight and evaluation of secondary amine/n-butanol biphasic solutions for CO_2 capture: Equilibrium solubility, phase separation behavior, absorption rate, desorption rate, energy consumption and ion species, Chem. Eng. J. 431 (2022) 133912.

[30] L. He, M. Fan, B. Dutcher, S. Cui, X.-D. Shen, Y. Kong, A.G. Russell, P. McCurdy, Dynamic separation of ultradilute CO_2 with a nanoporous amine-based sorbent, Chem. Eng. J. 189–190 (2012) 13–23.

[31] Y. Zhang, X. Ji, Y. Xie, X. Lu, Thermodynamic analysis of CO_2 separation from biogas with conventional ionic liquids, Appl. Energy 217 (2018) 75–87.

[32] Y. Xie, Y. Zhang, X. Lu, X. Ji, Energy consumption analysis for CO_2 separation using imidazolium-based ionic liquids, Appl. Energy 136 (2014) 325–335.

[33] M.M.F. Hasan, R.C. Baliban, J.A. Elia, C.A. Floudas, Modeling, simulation, and optimization of post-combustion CO_2 capture for variable feed concentration and flow rate. 2. Pressure swing adsorption and vacuum swing adsorption processes, Ind. Eng. Chem. Res. 51 (2012) 15665–15682.

[34] J. Du, H. Cao, Y. Li, Z. Yang, A. Eslamimanesh, M. Fakhroleslam, S.S. Mansouri, W. Shen, Development of hybrid surrogate model structures for design and optimization of CO_2 capture processes: Part I. Vacuum pressure swing adsorption in a confined space, Chem. Eng. Sci. 283 (2024) 119379.

[35] N. Shigaki, Y. Mogi, H. Kijima, T. Kakiuchi, T. Yajima, Y. Kawajiri, Performance evaluation of gas fraction vacuum pressure swing adsorption for CO_2 capture and utilization process, Int. J. Greenhouse Gas Control 120 (2022) 103763.

[36] B. Liu, Y. Lian, S. Li, S. Deng, L. Zhao, B. Chen, D. Wang, Experimental investigation on separation and energy-efficiency performance of temperature swing adsorption system for CO_2 capture, Sep. Purif. Technol. 227 (2019) 115670.

[37] Y. Zheng, L. Gao, S. He, Analysis of the mechanism of energy consumption for CO_2 capture in a power system, Energy (Oxf.) 262 (2023) 125103.

[38] J. Wang, Z. Guo, S. Deng, R. Zhao, L. Chen, J. Xue, A rapid multi-objective optimization of pressure and temperature swing adsorption for CO_2 capture based on simplified equilibrium model, Sep. Purif. Technol. 279 (2021) 119663.

[39] C. Song, Q. Liu, N. Ji, S. Deng, J. Zhao, Y. Li, Y. Kitamura, Reducing the energy consumption of membrane-cryogenic hybrid CO_2 capture by process optimization, Energy (Oxf.) 124 (2017) 29–39.

[40] B. Liu, X. Yang, P.-C. Chiang, T. Wang, Energy consumption analysis of cryogenic-membrane hybrid process for CO_2 capture from CO_2-EOR extraction gas, Aerosol Air Qual. Res. 20 (2020) 820–832.

[41] 空気分離によるガスのつくられ方,

https://www.jimga.or.jp/gas/produce_airseparation/ (accessed October 7, 2024).

[42] P. Bernardo, E. Drioli, G. Golemme, Membrane gas separation: A review/state of the art, Ind. Eng. Chem. Res. 48 (2009) 4638–4663.

[43] R. Sidhikku Kandath Valappil, N. Ghasem, M. Al-Marzouqi, Current and future trends in polymer membrane-based gas separation technology: A comprehensive review, J. Ind. Eng. Chem. 98 (2021) 103–129.

[44] R.W. Baker, B.T. Low, Gas separation membrane materials: A perspective, Macromolecules 47 (2014) 6999–7013.

[45] S. Fujikawa, R. Selyanchyn, T. Kunitake, A new strategy for membrane-based direct air capture, Polym. J. 53 (2021) 111–119.

[46] M. Nomura, S. Kasahara, S.-I. Nakao, Silica membrane reactor for the thermochemical iodine−sulfur process to produce hydrogen, Ind. Eng. Chem. Res. 43 (2004) 5874–5879.

[47] Z. Dai, L. Ansaloni, L. Deng, Recent advances in multi-layer composite polymeric membranes for CO_2 separation: A review, Green Energy Environ. 1 (2016) 102–128.

[48] D. De Meis, Gas transport through porous membranes, ENEA (2017) 1–20.

[49] J.G. Wijmans, R.W. Baker, The solution-diffusion model: a review, J. Memb. Sci. 107 (1995) 1–21.

[50] G.H. Fredrickson, E. Helfand, Dual-mode transport of penetrants in glassy polymers, Macromolecules 18 (1985) 2201–2207.

[51] W.J. Koros, D.R. Paul, A.A. Rocha, Carbon dioxide sorption and transport in polycarbonate, J. Polym. Sci. Polym. Phys. Ed. 14 (1976) 687–702.

[52] R.M. Barrer, Diffusivities in glassy polymers for the dual mode sorption model, J. Memb. Sci. 18 (1984) 25–35.

[53] F. Moghadam, E. Kamio, H. Matsuyama, High CO_2 separation performance of amino acid ionic liquid-based double network ion gel membranes in low CO_2 concentration gas mixtures under humid conditions, J. Memb. Sci. 525 (2017) 290–297.

[54] W.M. McDanel, M.G. Cowan, N.O. Chisholm, D.L. Gin, R.D. Noble, Fixed-site-carrier facilitated transport of carbon dioxide through ionic-liquid-based epoxy-amine ion gel membranes, J. Memb. Sci. 492 (2015) 303–311.

[55] Y. Han, D. Wu, W.S.W. Ho, Nanotube-reinforced facilitated transport membrane for CO_2/N_2 separation with vacuum operation, J. Memb. Sci. 567 (2018) 261–271.

[56] L. Deng, T.-J. Kim, M.-B. Hägg, Facilitated transport of CO_2 in novel PVAm/PVA blend membrane, J. Memb. Sci. 340 (2009) 154–163.

[57] J. Huang, J. Zou, W.S.W. Ho, Carbon dioxide capture using a CO_2-selective

facilitated transport membrane, Ind. Eng. Chem. Res. 47 (2008) 1261–1267.

[58] J. Shang, G. Li, R. Singh, Q. Gu, K.M. Nairn, T.J. Bastow, N. Medhekar, C.M. Doherty, A.J. Hill, J.Z. Liu, P.A. Webley, Discriminative separation of gases by a "molecular trapdoor" mechanism in chabazite zeolites, J. Am. Chem. Soc. 134 (2012) 19246–19253.

[59] R. Kitaura, K. Seki, G. Akiyama, S. Kitagawa, Porous coordination-polymer crystals with gated channels specific for supercritical gases, Angew. Chem. Int. Ed Engl. 42 (2003) 428–431.

[60] Y. Ying, Z. Zhang, S.B. Peh, A. Karmakar, Y. Cheng, J. Zhang, L. Xi, C. Boothroyd, Y.M. Lam, C. Zhong, D. Zhao, Pressure-responsive two-dimensional metal-organic framework composite membranes for CO_2 separation, Angew. Chem. Int. Ed Engl. 60 (2021) 11318–11325.

[61] Development of technology for CO_2 separation, capture, etc, NEDO green innovation fund projects. https://green-innovation.nedo.go.jp/en/project/development-co2-separation-recovery/ (accessed October 7, 2024).

[62] B. Comesaña-Gándara, J. Chen, C.G. Bezzu, M. Carta, I. Rose, M.-C. Ferrari, E. Esposito, A. Fuoco, J.C. Jansen, N.B. McKeown, Redefining the Robeson upper bounds for CO_2/CH_4 and CO_2/N_2 separations using a series of ultrapermeable benzotriptycene-based polymers of intrinsic microporosity, Energy Environ. Sci. 12 (2019) 2733–2740.

[63] L.M. Robeson, The upper bound revisited, J. Memb. Sci. 320 (2008) 390–400.

[64] Y. Kohno, M. Kanakubo, M. Iwaya, Y. Yamato, T. Makino, Ionic liquid mixtures for direct air capture: High CO_2 permeation driven by superior CO_2 absorption with lower absolute enthalpy, ACS Omega 7 (2022) 42155–42162.

[65] A.B. Pereiro, L.C. Tomé, S. Martinho, L.P.N. Rebelo, I.M. Marrucho, Gas permeation properties of fluorinated ionic liquids, Ind. Eng. Chem. Res. 52 (2013) 4994–5001.

[66] S.M. Mahurin, P.C. Hillesheim, J.S. Yeary, D.-E. Jiang, S. Dai, High CO_2 solubility, permeability and selectivity in ionic liquids with the tetracyanoborate anion, RSC Adv. 2 (2012) 11813–11819.

[67] K. Kusakabe, T. Kuroda, A. Murata, S. Morooka, Formation of a Y-type zeolite membrane on a porous α-alumina tube for gas separation, Ind. Eng. Chem. Res. 36 (1997) 649–655.

[68] T. Tomita, K. Nakayama, H. Sakai, Gas separation characteristics of DDR type zeolite membrane, Microporous Mesoporous Mater. 68 (2004) 71–75.

[69] Q. Qian, P.A. Asinger, M.J. Lee, G. Han, K. Mizrahi Rodriguez, S. Lin, F.M. Benedetti, A.X. Wu, W.S. Chi, Z.P. Smith, MOF-based membranes for gas separations, Chem. Rev. 120 (2020) 8161–8266.

[70] F. Dorosti, L. Ge, H. Wang, J. Bell, R. Lin, J. Hou, Z. Zhu, Non-selective defect minimization towards highly efficient metal-organic framework membranes for gas separation, Angew. Chem. Weinheim Bergstr. Ger. (2024).

[71] G. Dong, H. Li, V. Chen, Challenges and opportunities for mixed-matrix membranes for gas separation, J. Mater. Chem. A Mater. Energy Sustain. 1 (2013) 4610–4630.

[72] Z. Kang, Y. Peng, Y. Qian, D. Yuan, M.A. Addicoat, T. Heine, Z. Hu, L. Tee, Z. Guo, D. Zhao, Mixed matrix membranes (MMMs) comprising exfoliated 2D covalent organic frameworks (COFs) for efficient CO_2 separation, Chem. Mater. 28 (2016) 1277–1285.

[73] X. Tan, S. Robijns, R. Thür, Q. Ke, N.D. Witte, A. Lamaire, Y. Li, I. Aslam, D. Van Havere, T. Donckels, T. Van Assche, V. Van Speybroeck, M. Dusselier, I. Vankelecom, Truly combining the advantages of polymeric and zeolite membranes for gas separations, Science 378 (2022) 1189–1194.

[74] A.P. Côté, A.I. Benin, N.W. Ockwig, M. O'Keeffe, A.J. Matzger, O.M. Yaghi, Porous, crystalline, covalent organic frameworks, Science 310 (2005) 1166–1170.

[75] K. Geng, T. He, R. Liu, S. Dalapati, K.T. Tan, Z. Li, S. Tao, Y. Gong, Q. Jiang, D. Jiang, Covalent organic frameworks: Design, synthesis, and functions, Chem. Rev. 120 (2020) 8814–8933.

[76] E. Jin, S. Fu, H. Hanayama, M.A. Addicoat, W. Wei, Q. Chen, R. Graf, K. Landfester, M. Bonn, K.A.I. Zhang, H.I. Wang, K. Müllen, A. Narita, A nanographene-based two-dimensional covalent organic framework as a stable and efficient photocatalyst, Angew. Chem. Int. Ed. 61 (2022) e202114059.

[77] C.S. Diercks, S. Lin, N. Kornienko, E.A. Kapustin, E.M. Nichols, C. Zhu, Y. Zhao, C.J. Chang, O.M. Yaghi, Reticular electronic tuning of porphyrin active sites in covalent organic frameworks for electrocatalytic carbon dioxide reduction, J. Am. Chem. Soc. 140 (2018) 1116–1122.

[78] Z. Wang, Q. Yu, Y. Huang, H. An, Y. Zhao, Y. Feng, X. Li, X. Shi, J. Liang, F. Pan, P. Cheng, Y. Chen, S. Ma, Z. Zhang, PolyCOFs: A new class of freestanding responsive covalent organic framework membranes with high mechanical performance, ACS Cent. Sci. 5 (2019) 1352–1359.

[79] G. Cheng, C. Sui, W. Hao, J. Li, Y. Zhao, L. Miao, G. Zhao, J. Li, Y. Sang, C. Zhao, L. Wen, X. He, C. Wang, Ultra-strong Janus covalent organic framework membrane with smart response to organic vapor, Small 20 (2024) 2401635.

[80] Y. Ying, S.B. Peh, H. Yang, Z. Yang, D. Zhao, Ultrathin covalent organic framework membranes via a multi-interfacial engineering strategy for gas separation, Adv. Mater. 34 (2022) e2104946.

[81] J. Liu, G. Han, D. Zhao, K. Lu, J. Gao, T.-S. Chung, Self-standing and flexible covalent organic framework (COF) membranes for molecular separation, Sci. Adv. 6 (2020) eabb1110.

[82] H. Fan, A. Mundstock, A. Feldhoff, A. Knebel, J. Gu, H. Meng, J. Caro, Covalent organic framework–covalent organic framework bilayer membranes for highly selective gas separation, J. Am. Chem. Soc. 140 (2018) 10094–10098.

[83] Z. Guo, H. Wu, Y. Chen, S. Zhu, H. Jiang, S. Song, Y. Ren, Y. Wang, X. Liang, G. He, Y. Li, Z. Jiang, Missing-linker defects in covalent organic framework membranes for efficient CO_2 separation, Angew. Chem. Int. Ed Engl. 61 (2022) e202210466.

[84] M. Liu, Y. Liu, J. Dong, Y. Bai, W. Gao, S. Shang, X. Wang, J. Kuang, C. Du, Y. Zou, J. Chen, Y. Liu, Two-dimensional covalent organic framework films prepared on various substrates through vapor induced conversion, Nat. Commun. 13 (2022) 1–9.

[85] K. Dey, M. Pal, K.C. Rout, S. Kunjattu H, A. Das, R. Mukherjee, U.K. Kharul, R. Banerjee, Selective molecular separation by interfacially crystallized covalent organic framework thin films, J. Am. Chem. Soc. 139 (2017) 13083–13091.

[86] J.W. Colson, A.R. Woll, A. Mukherjee, M.P. Levendorf, E.L. Spitler, V.B. Shields,

M.G. Spencer, J. Park, W.R. Dichtel, Oriented 2D covalent organic framework thin films on single-layer graphene, Science 332 (2011) 228–231.

[87] R.P. Bisbey, C.R. DeBlase, B.J. Smith, W.R. Dichtel, Two-dimensional covalent organic framework thin films grown in flow, J. Am. Chem. Soc. 138 (2016) 11433–11436.

[88] K. Liu, H. Qi, R. Dong, R. Shivhare, M. Addicoat, T. Zhang, H. Sahabudeen, T. Heine, S. Mannsfeld, U. Kaiser, Z. Zheng, X. Feng, On-water surface synthesis of crystalline, few-layer two-dimensional polymers assisted by surfactant monolayers, Nat. Chem. 11 (2019) 994–1000.

[89] C. Fan, H. Wu, J. Guan, X. You, C. Yang, X. Wang, L. Cao, B. Shi, Q. Peng, Y. Kong, Y. Wu, N.A. Khan, Z. Jiang, Scalable fabrication of crystalline COF membranes from amorphous polymeric membranes, Angew. Chem. Int. Ed Engl. 60 (2021) 18051–18058.

[90] N.A. Khan, R. Zhang, H. Wu, J. Shen, J. Yuan, C. Fan, L. Cao, M.A. Olson, Z. Jiang, Solid–vapor interface engineered covalent organic framework membranes for molecular separation, J. Am. Chem. Soc. 142 (2020) 13450–13458.

[91] T. Shirokura, T. Hirohata, K. Sato, E. Villani, K. Sekiya, Y.-A. Chien, T. Kurioka, R. Hifumi, Y. Hattori, M. Sone, I. Tomita, S. Inagi, Site-selective synthesis and concurrent immobilization of imine-based covalent organic frameworks on electrodes using an electrogenerated acid, Angew. Chem. Int. Ed Engl. 62 (2023) e202307343.

[92] N.A.A. Zwaneveld, R. Pawlak, M. Abel, D. Catalin, D. Gigmes, D. Bertin, L. Porte, Organized formation of 2D extended covalent organic frameworks at surfaces, J. Am. Chem. Soc. 130 (2008) 6678–6679.

[93] M. Tong, Q. Yang, Q. Ma, D. Liu, C. Zhong, Few-layered ultrathin covalent organic framework membranes for gas separation: a computational study, J. Mater. Chem. A Mater. Energy Sustain. 4 (2016) 124–131.

[94] H. Fan, A. Mundstock, J. Gu, H. Meng, J. Caro, An azine-linked covalent organic framework ACOF-1 membrane for highly selective CO_2/CH_4 separation, J. Mater. Chem. A Mater. Energy Sustain. 6 (2018) 16849–16853.

[95] J.E. Lopez-Cazares, K. Kim, J.Y.S. Lin, K. Jin, Gas permeation and separation characteristics of microporous TpHz COF membranes synthesized by substrate-

assisted interfacial polymerization, Ind. Eng. Chem. Res. 63 (2024) 3684–3694.

[96] H.S. Sasmal, A. Halder, S. Kunjattu H, K. Dey, A. Nadol, T.G. Ajithkumar, P. Ravindra Bedadur, R. Banerjee, Covalent self-assembly in two dimensions: Connecting covalent organic framework nanospheres into crystalline and porous thin films, J. Am. Chem. Soc. 141 (2019) 20371–20379.

[97] Y. Ying, M. Tong, S. Ning, S.K. Ravi, S.B. Peh, S.C. Tan, S.J. Pennycook, D. Zhao, Ultrathin two-dimensional membranes assembled by ionic covalent organic nanosheets with reduced apertures for gas separation, J. Am. Chem. Soc. 142 (2020) 4472–4480.

[98] Z. Guo, H. Jiang, H. Wu, L. Zhang, S. Song, Y. Chen, C. Zheng, Y. Ren, R. Zhao, Y. Li, Y. Yin, M.D. Guiver, Z. Jiang, Oil-water-oil triphase synthesis of ionic covalent organic framework nanosheets, Angew. Chem. Int. Ed Engl. 60 (2021) 27078–27085.

[99] H. Fan, M. Peng, I. Strauss, A. Mundstock, H. Meng, J. Caro, High-flux vertically aligned 2D covalent organic framework membrane with enhanced hydrogen separation, J. Am. Chem. Soc. 142 (2020) 6872–6877.

[100] H. Fan, H. Wang, M. Peng, H. Meng, A. Mundstock, A. Knebel, J. Caro, Pore-in-pore engineering in a covalent organic framework membrane for gas separation, ACS Nano 17 (2023) 7584–7594.

[101] P. Wang, Y. Peng, C. Zhu, R. Yao, H. Song, L. Kun, W. Yang, Single-phase covalent organic framework staggered stacking nanosheet membrane for CO_2 -selective separation, Angew. Chem. Int. Ed Engl. 60 (2021) 19047–19052.

[102] H. Zhang, T. Shao, Z. Cheng, J. Dong, Z. Wang, H. Jiang, X. Zhao, T. Xiaoteng Liu, G. Zhu, X. Zou, Assembly-dissociation-reconstruction synthesis of covalent organic framework membranes with high continuity for efficient CO_2 separation, Angew. Chem. Int. Ed Engl. (2024) e202411724.

[103] Z. Zhang, C. Yin, G. Yang, A. Xiao, X. Shi, W. Xing, Y. Wang, Stitching nanosheets of covalent organic frameworks to build aligned nanopores in nanofiltration membranes for precise ion separations, J. Memb. Sci. 618 (2021) 118754.

[104] S.A. Stern, The “barrer” permeability unit, J. Polym. Sci. A-2 Polym. Phys. 6 (1968) 1933–1934.

Chapter 2 Thermodynamic Efficiency of Membrane Separation of Dilute Gas: Estimation for CO_2 Direct Air Capture Application

2.1 Introduction

Capturing greenhouse gases such as CO_2 is essential for alleviating global warming [1]. The energy efficiency of CO_2 separation is a hot topic, and the estimation and optimization of schemes and materials for specific applications have been reported. Experimental and theoretical analyses of direct air capture (DAC), in which very dilute CO_2 (400 molar ppm) in the air is concentrated, are performed using specific materials and schemes [2–8]. Some processes can be energy efficient in special circumstances, such as physisorption and cryogenic processes [9,10], where low temperatures are available (in space colonies, for example), or chemisorption processes [11] where high temperatures are available (near iron manufacturing furnaces, for example). However, among the many methods for gas separation, selective permeation through a membrane is often referred to as an energy-efficient technique [12]. For researchers studying separation membranes, a guideline for energy efficiency and membrane parameters is

desirable, but the theoretical limit of energy efficiency for various membrane parameters for DAC has not yet been vigorously explored.

Herein, I provide a detailed analysis of the energy efficiency of membrane separation based on thermodynamic considerations. Although the theory involved is classical, i.e., merely mixing entropy calculation, surprisingly rich features were noticed during the detailed analysis. Two models of operation of the membrane separation device were examined: a vacuum swing and a continuous pumping operation scheme, which are repeated sequential permeation–pumping and maintaining internal pressure by exhaust, respectively. These schemes can be used for the separation of any two gases. In the following, I use parameters for atmospheric CO_2 and "air (without CO_2)," considering the application of DAC.

2.2 Models and Methods

2.2.1 Vacuum swing model

Figure 2-1a illustrates the setup of a repeated sequential permeation–pumping scheme, named after "vacuum swing." This scheme is considered because no irreversible mixing occurs outside the membrane and the highest energy efficiency is expected among the models. Initially, both chambers were thoroughly pumped from a separate route, with

valves 0 and 1 closed.

The work for the initial evacuation was not counted because this work was required only once at the beginning. The following three steps were performed: [Step 1] Valve 0 was opened until the pressure of chamber 0 reached the ambient pressure of P_0. The ambient gas contains CO_2 and "air (without CO_2)," which will be mentioned as "air" for simplicity in the following. Their partial pressures were $(1-\alpha)P_0$ and αP_0, respectively. [Step 2] The pressure difference causes permeation of CO_2 and air with different kinetic constants, where r is the membrane separation ratio. [Step 3] After a specific time, valves 0 and 1 are closed again, and the gas in chamber 1 is compressed to ambient pressure and transferred to the output.

2.2.2 Continuous pumping model

Figure 2-1b illustrates the continuous pumping model. In this model, chamber 0 is assumed to be very large, ideally the entire atmosphere of the earth. Gas molecules permeating through the membrane are pumped to ambient pressure continuously, and the partial pressures of CO_2 and air are constant in Chamber 1. In this model, the operation is simple and practically crucial, because there is no moving part other than the pump compressor.

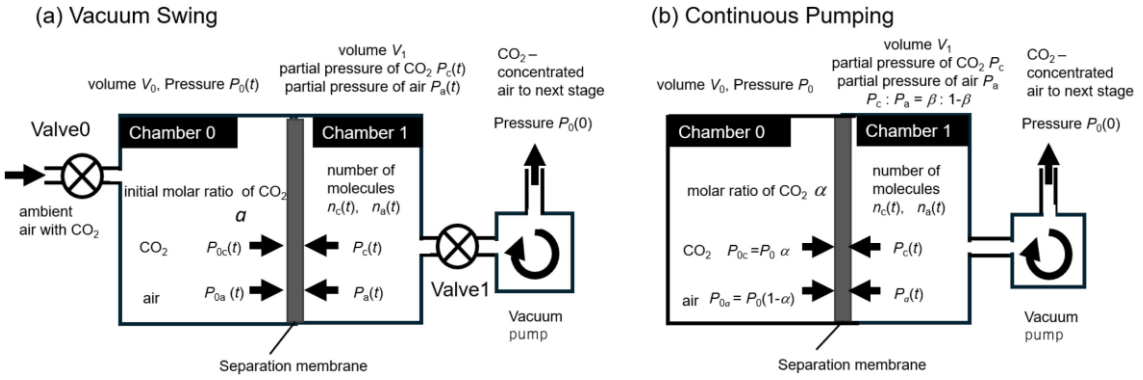

Fig. 2-1. Two models were used for the membrane separation using a vacuum pump. (a) Vacuum swing (Model 1). (b) Continuous pumping (Model 2).

2.2.3 Methods

In the following analysis, the change in the free energy due to the concentration change is calculated from the change in entropy (ΔS) and the system temperature T as $-T\Delta S$. Historically, this equation was adopted for efficiency analysis and has been used in the era of van't Hoff [14]. $-T\Delta S$ corresponds to the minimum thermodynamic work required for the reversible gas separation process. I will discuss the energy efficiency of separation from these minimum work values divided by the actual work done by the pump. The Maxima (ver. 5.47) for arithmetic handling of the equations, including Taylor expansion, to study asymptotic behavior. In order to find the optimum parameters for maximizing efficiency and related values, the optimization library in SciPy and Python (ver. 3.12). All gases were regarded as ideal gases.

2.3 Results and Discussion

2.3.1 Vacuum swing model

The rate constants for permeation were assumed to be different for CO_2 and air, which were denoted as *kr* and *k*, respectively. *r* corresponds to the selectivity of the membrane separation, which is much greater than 1. The number of molecules (in mols) can then be expressed by the following differential equations:

$$\frac{dn_c}{dt} = kr(P_{0c} - P_c) \tag{2.1}$$

$$\frac{dn_a}{dt} = k(P_{0a} - P_a) \tag{2.2}$$

$$\frac{dn_{0c}}{dt} = -kr(P_{0c} - P_c) \tag{2.3}$$

$$\frac{dn_{0a}}{dt} = -k(P_{0a} - P_a) \tag{2.4}$$

where n_{0c} and n_{0a} and n_c and n_a denote the molar numbers of CO_2 and air molecules in Chambers 0 and 1, respectively. The "a" and "c" are denoted by the species of air and CO_2, respectively. The partial pressures P_{0c}, P_{0a}, P_c, and P_a are defined similarly. All molar numbers and partial pressures are functions of time, where time $t = 0$ is the start of [Step 1].

It is necessary to derive the relationship between the partial pressure and the number of molecules. Let $P_{0i}V_0=n_{0i}RT$, where P_{0i}, V_0, and n_i are the pressure, volume, and molar number of species i (= a or c) in Chamber 0, respectively, R is the gas constant,

and T is the absolute temperature. A similar relation, $P_iV_0=n_iRT$, applies to Chamber 1. The temperatures of chambers 0 and 1 were assumed to be the same. Eqs. (2.1) and (2.4) yields the following equations:

$$\frac{d(V_0P_{0c}+V_1P_c)}{dt}=0 \tag{2.5}$$

$$\frac{d(P_{0c}-P_c)}{dt}=-kRTr\left(\frac{1}{V_0}+\frac{1}{V_1}\right)(P_{0c}-P_c) \tag{2.6}$$

$$\frac{d(V_0P_{0a}+V_1P_a)}{dt}=0 \tag{2.7}$$

$$\frac{d(P_{0a}-P_a)}{dt}=-kRT\left(\frac{1}{V_0}+\frac{1}{V_1}\right)(P_{0a}-P_a) \tag{2.8}$$

I put $v_{01}=V_0/V_1$ and $K=\frac{kRT}{V_0}$. Eq. (2.5) to (2.8) can be solved by using $P_a(0)=P_c(0)=0$ and $P_{0a}(0)+P_{0c}(0)=P_0$, and $P_{0c}(0) : P_{0a}(0) = \alpha : 1\text{-}\alpha$.

$$P_{0c}(t)=P_0\alpha\left(\frac{1}{1+v_{01}}\exp(-Kr(1+v_{01})t)+\frac{v_{01}}{1+v_{01}}\right) \tag{2.9}$$

$$P_c(t)=P_0\alpha\frac{v_{01}}{1+v_{01}}\left(1-\exp\left((-Kr(1+v_{01})t\right)\right) \tag{2.10}$$

$$P_{0a}(t)=P_0(1-\alpha)\left(\frac{1}{1+v_{01}}\exp(-K(1+v_{01})t)+\frac{v_{01}}{1+v_{01}}\right) \tag{2.11}$$

$$P_a(t)=P_0(1-\alpha)\frac{v_{01}}{1+v_{01}}\left(1-\exp\left((-K(1+v_{01})t\right)\right) \tag{2.12}$$

The bahavor of Eqs. (2.10) and (2.12) as functions of time are shown in Fig. 2-2. The partial pressure of CO_2 initially increases faster than that of air but saturates quickly. CO_2 is condensed at the time indicated by the arrows. However, I do not have "Maxwell's daemon" to control a single molecule's motion; a membrane with a permeability difference can separate the gases [12].

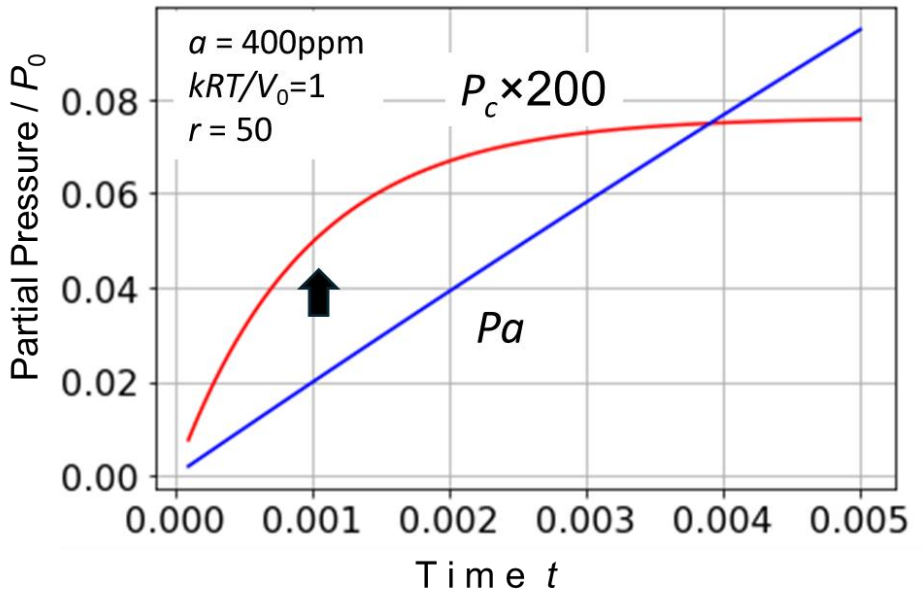

Fig. 2-2. Typical time evolution of partial pressures at different permeation speeds in Model 1.

The entropy of chambers 0 and 1 at time t is as follows:

$$S_0 = n_{0c}(t)\log\frac{p_{0c}(t)}{p_{0c}(t)+p_{0a}(t)} + n_{0a}(t)\log\frac{p_{0a}(t)}{p_{0c}(t)+p_{0a}(t)} \tag{2.13}$$

$$S_1 = n_c(t)\log\frac{p_c(t)}{p_c(t)+p_a(t)} + n_a(t)\log\frac{p_a(t)}{p_c(t)+p_a(t)} \tag{2.14}$$

The initial (t =0) entropy is given by Eq. (2.15).

$$S_{00} = n_{0c}(0)\log\frac{p_{0c}(0)}{p_{0c}(0)+p_{0a}(0)} + n_{0a}(0)\log\frac{p_{0a}(0)}{p_{0c}(0)+p_{0a}(0)} \tag{2.15}$$

The decrease in entropy in one cycle provides a thermodynamic measure for membrane separation.

$$\Delta S = -(S_0 + S_1 - S_{00}) \tag{2.16}$$

The thermodynamic efficiency of η is given by Eq. (2.17).

$$\eta = \frac{T\Delta S}{W} \tag{2.17}$$

where W denotes the work performed by the pumping system. W was calculated from the compression work from $P_1(t) = p_c(t) + p_a(t)$ to the ambient pressure P_0 at the outlet.

$$W = P_1 V_1 \log \frac{P_0}{P_1} \tag{2.18}$$

The results are presented as figures with time parameter of $s = Kt$. There is an optimum value of s with a set of α, r, and v_{01} that maximize η. Figure 2-3a shows a typical relationship between time $s=krt$ and efficiency η. In Fig. 2-3a, s gives the maximum efficiency at s =0.01, whereas the optimum s decreases as r increases. Figures 2-3b and c show plots of increased r. The maximum efficiency increases significantly as r increases.

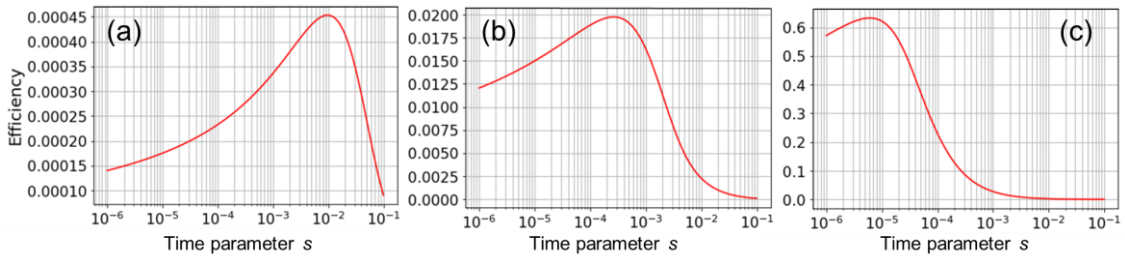

Fig. 2-3. Efficiency in Model 1 as a Function of Time Parameter $s = Kt$. α = 400ppm, v_{01}=10. (a) r=5 (b) r=100 (c) r=10000.

This is illustrated by plotting the maximum efficiency as a function of selectivity r, as shown in Fig. 2-4a. This result has important implications for practical applications, such as DAC. The energy efficiencies are summarized in Table 2-1. The energy efficiency of the membrane separation is significantly affected by r, which has not been previously reported under this generic condition. The dependence of the efficiency on the volume ratio of the chambers $v_{01} = V_0/V_1$ is negligible and converges to one curve when v_{01} becomes large (Fig. 2-4b). This was consistent with the mathematical analysis of the equations. The required vacuum can be estimated from P_c values at the optimum $s = Kt$ in Eq. (2.10) and Fig. 2-3. This value is of the order of 1–10 Pa, which is achievable using a good mechanical pump.

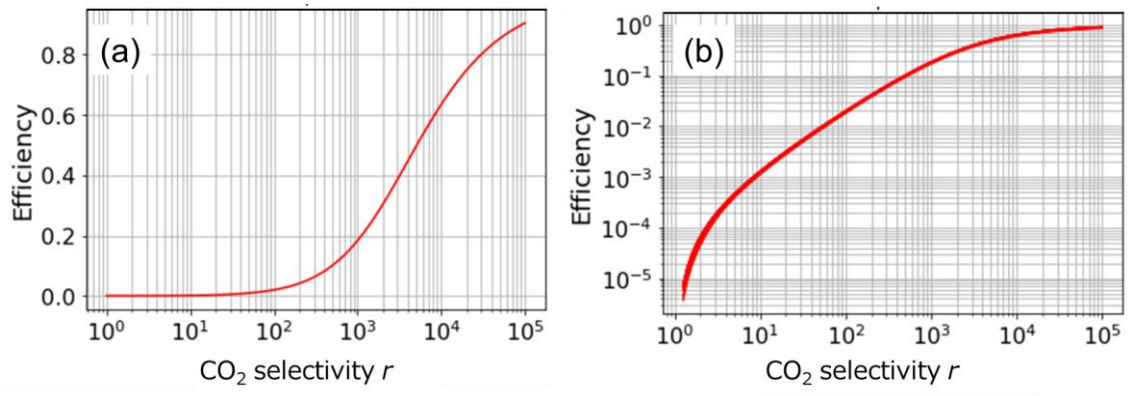

Fig. 2-4. Efficiency as a function of r. (a) Curve for α = 400ppm and v_{01}=20. (b) v_{01}=5–500 overlapped in the log–log plot.

Table 2-1. Efficiency as a function of selectivity r in Model 1.

Selectivity r	Efficiency η /%	Output con. β /%
5	0.05	14.1
10	0.13	24.4
50	0.92	59.1
100	2.00	72.3
500	10.7	90.4
1000	18.4	94.1
5000	49.9	98.2
10000	63.8	99.0

2.3.2 Continuous pumping model

In this model, the variables are determined by the steady-state condition:

$$\frac{dP_c}{dt} : \frac{dP_a}{dt} = P_c : P_a \tag{2.19}$$

Let β be the ratio of CO_2 in the permeating gas. The CO_2 and air molecule balance permeating Chamber 1 in a short time Δt are given by the following:

$$\Delta n_c = kr(P_{0c} - P_c)\Delta t \tag{2.20}$$

$$\Delta n_a = k(P_{0a} - P_a)\Delta t \tag{2.21}$$

$$\Delta n_c = \frac{\beta}{1-\beta}\Delta n_a \tag{2.22}$$

When $n_c = \frac{P_c V_1}{RT}$ and $n_a = \frac{P_a V_1}{RT}$, Eq. (2.19) leads to following Eq. (2.23).

$$\Delta n_c : \Delta n_a = \frac{\mathrm{d}P_c}{\mathrm{d}t} : \frac{\mathrm{d}P_a}{\mathrm{d}t} \tag{2.23}$$

When I assume V_0>>V_1 (for example, Chamber 0 is the whole earth), I can neglect the change in the pressure and composition in Chamber 0 during Δt as the second order and use the constant relation $P_{0c} = P_0\,\alpha$ and $P_{0a} = P_0\,(1-\alpha)$. From Eq. (2.20) to (2.23), the following equations are derived:

$$P_c = P_0 \frac{\beta}{1-\beta}\frac{1}{1-r}\left(1 - \alpha - r\alpha\frac{1-\beta}{\beta}\right) \tag{2.24}$$

$$P_a = P_0 \frac{1}{1-r}\left(1 - \alpha - r\alpha\frac{1-\beta}{\beta}\right) \tag{2.25}$$

The minimum thermodynamic work $-T\Delta S$ was calculated using Eq. (2.16). I include the change in the concentration on both sides by permeation during Δt. Work W was calculated using Eq. (2.18).

Figure 2-5 shows the energy efficiency η as a function of r for various values of β. Here, v_{01} was set to a very large value (=10^6) to ensure that permeation did not change the kinetics. The arithmetic analysis shows that it is an increasing function of r.

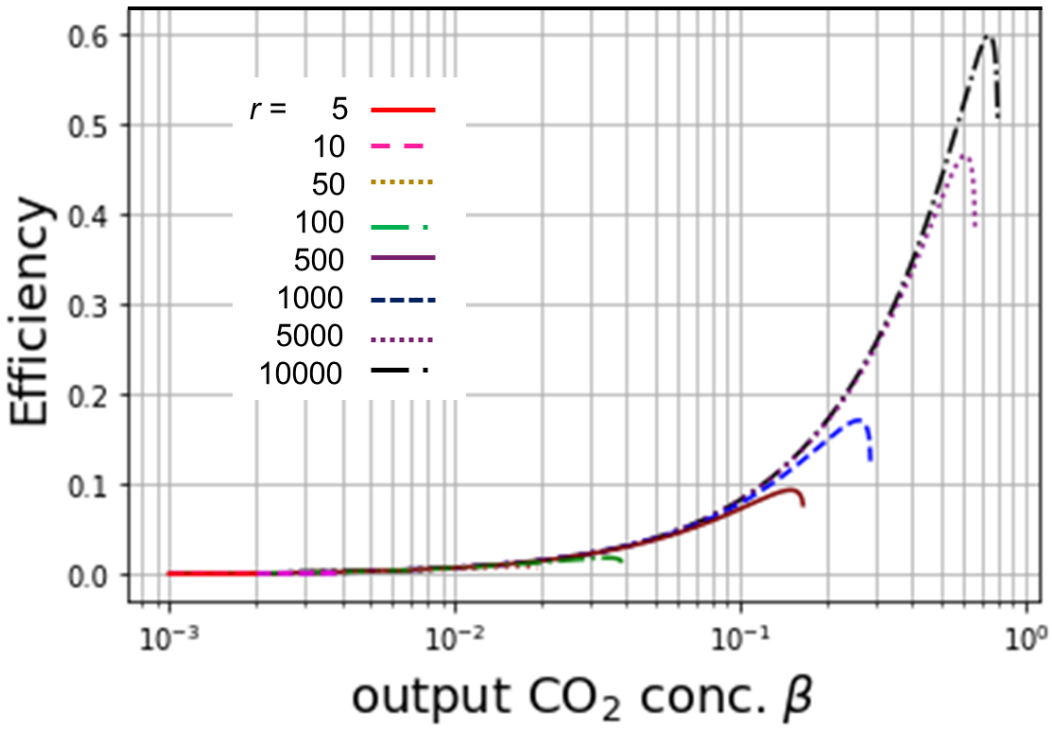

Fig. 2-5. Efficiency as a function of output CO_2 concentration β in Model 2.

I searched for the optimum β for each set of parameters. The results are shown in Fig. 2-6a. Note that the curve converges as v_{01} increases, indicating that the approximation is valid. The total pressure of Chamber 1 was the only parameter controlled from the outside, and the optimum values are plotted in Fig. 2-6b. When $r <$ ca. 40, the output CO_2 concentration β values converge to the initial concentration α and become practically meaningless when considering the efficiency (Fig. 2-6c).

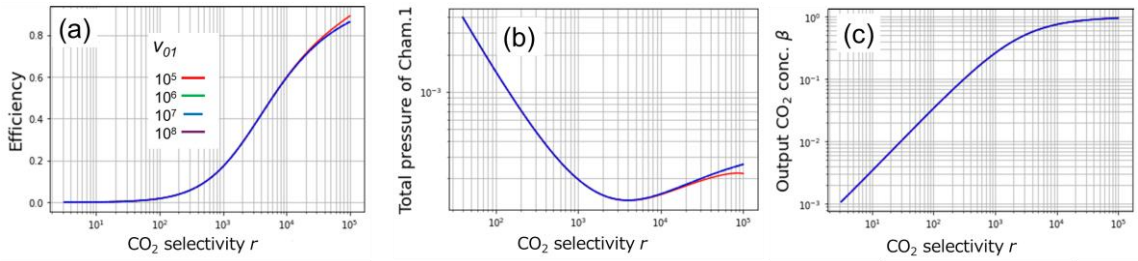

Fig. 2-6. (a) Maximum efficiency as a function of the CO_2 selectivity r in Model 2. (b) Total pressure and (c) output CO_2 concentration β of chamber 1 for maximum efficiency.

2.3.3 Discussion

It is often mentioned that membrane separation can be energy-efficient, but I could not find a precise formula for energy efficiency in the literature for vacuum swing (Model 1) or continuous pumping (Model 2). From the above calculations using basic thermodynamics, it was concluded that the energy efficiency is strongly related to the selectivity r of the membrane. Although a separation membrane is often evaluated by r and permeation speed, as in Robeson's upper bound [13], the ideal energy efficiency is related to r, not the permeation rate constant k. If an initial CO_2 concentration of 400 ppm is used for the DAC, $\eta = 1\%$ will be achieved at $r \simeq 100$, and $\eta = 10\%$ will be achieved at $r \simeq 1000$ in model 1 (Fig. 2-4). Model 2 (Fig. 2-5) gives slightly higher efficiency but is still around 1% when r is 100.

It is worth mentioning that the analysis of a higher α value. Figure 2-6 shows the efficiency vs. CO_2 selectivity r for Models 1 and 2 with α = 4%. It is seen that the

efficiency with a lower r, e.g., r = 10, gives a much higher efficiency (8%) than the case of α = 400ppm.

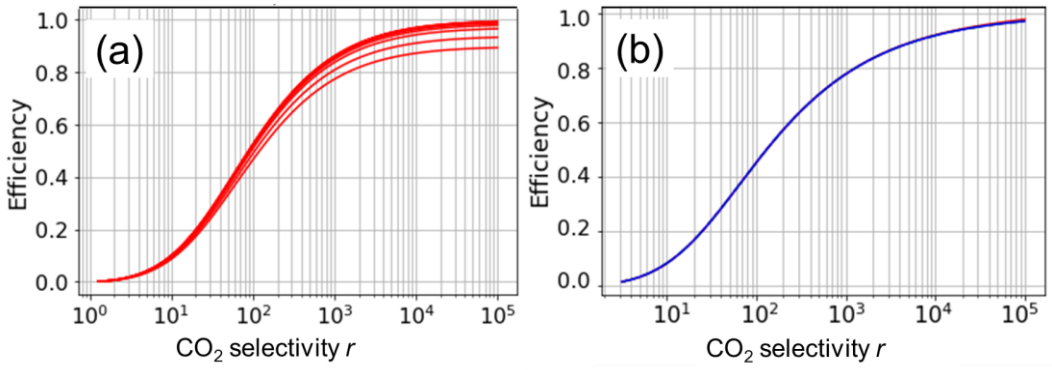

Fig. 2-6. Efficiency as a function of r when α = 4%. (a) Model 1 and (b) Model 2. Multiple lines correspond to different volume ratios of the two chambers (v_{01}=10^5–10^8).

The energy efficiency of other methods, such as zeolite adsorption, is theoretically estimated to be 43% [15], which is reasonable because adsorption schemes require extra energy to desorb CO_2. Therefore, it can be concluded that the energy efficiency of membrane separation can be higher than that of the other methods if a sufficiently good membrane is used. High values of r for separation membranes exceeding 100 have rarely been reported [16]. Some candidates are carbon-based films [17], ionic-liquid–polymer composites [18], mixtures of ionic liquids [19], mixed-matrix membranes with zeolites [20], and graphene oxides [21], followed by fluoropolymers with slightly lower selectivity(r =50–60) [22]. Facilitated transport membranes, which are gels composed of water, ionic liquids, and mobile CO_2 transporter molecules contained in a polymer

network, show very high selectivity ($r > 10^2$–10^3). However, some of them require high temperatures (~100 °C) and humidity control [23–25].

The results presented here clearly indicate the importance of a very high separation ratio for achieving high energy efficiency, and future research should be pursued in this direction. A crack in the membrane degrades the separation ratio, and for the maintenance and lifetime of the device, soft membranes immersed in a low-vapor-pressure liquid can be a candidate. Energy analysis of the recently appearing electrochemical CO_2 pumping [26] is required for comparison with the ideal efficiency, with one report of 393.7kJ/mol-CO_2 without optimization [6].

It is worth mentioning that the thermodynamic work required to separate CO_2 and air from the gas containing α = 400 ppm CO_2 was calculated from the mixing entropy ($\Delta S = -R\,(\alpha \log\alpha + (1-\alpha)/\alpha \log(1-\alpha))$). It is 22.0 kJ/mol-$CO_2$ and 0.500 GJ/ton-CO_2 = 139 kWh/ton-CO_2 at 300 K. This value is compared to reported energy consumption values, which sometimes do not include the entropy term from a very diluted CO_2 input and should be a pure loss. They are grouped below 1.0 GJ/ton-CO_2 [10,27], 1.4–1.8 GJ/ton-CO_2 [6,9,28], 4–9 GJ/ton-CO_2 [29,30], or over 10 GJ/ton-CO_2 [4,15,31,32] of various schemes. The detailed data are summarized in Table 2-2. It should be noted that the theoretical limit (22.0 kJ/mol) is about 5.7% of the enthalpy when the CO_2 is reduced to

graphite (393.5 kJ/mol[33]). These analyses show that the energy required for separation becomes comparable to the reduction energy when the CO_2 separation ratio of the membrane r is greater than 100. The separation ratio should not be ignored when planning membrane-based CCS technology.

Table 2-2. Comparison of energy consumption

Method	Energy consumption /GJ ton-CO_2^{-1}	Target	Ref.
Theoretical value (not a specific separation method)	35	DAC	[32]
IL absorption–desorption ([Emim][Et_2PO_4])	0.66–1.09	Biogas purification	[27]
CO_2 absorption with phase separation	1.6	Post-combustion process	[28]
PSA-based carbon absorbent	14	CO_2/CH_4 separation	[15]
TSA-based multi-step tree system	50	DAC	[4]
TSA with zeolite 13X–APG (experiment)	6.9	Flue gas separation	[29]
MEA-based absorption	5.3	Flue gas separation	[30]
Ammonium-based ionic exchange (experiment)	1.5	DAC	[6]
Membrane–cryogenic hybrid CO_2 capture	1.7	Flue gas separation	[9]
Hybrid membrane–cryogenic process	0.85	CO_2-enhanced oil recovery	[10]
Membrane-based, muti-step CO_2 separation	44	DAC	[31]
Membrane-based vacuum swing or continuous pumping	0.50	DAC	**This work**

2.4 Conclusion

The maximum efficiency of CO_2 capture using membrane separation under DAC conditions was evaluated using numerical analysis with a steady-state approximation. The maximum efficiency reached 63% using the membrane with a CO_2 selectivity of 10000, and I obtained CO_2 at a concentration of 99% in the permeated gas. In comparison, the efficiency was only 2% for a membrane with a selectivity 100. I found that The maximum efficiency was strongly dependent on the CO_2 selectivity of the membrane but not on the permeation rate and volumetric ratio between the feed and permeate sides. This study offers a theoretical framework for the economic and practical use of the membrane separation method for DAC, indicating the importance of developing new CO_2 separation membranes with drastically high CO_2 selectivity.

References

[1] R. Wordsworth, J.T. Seeley, K.P. Shine, Fermi resonance and the quantum mechanical basis of global warming, Planet. Sci. J. 5 (2024) 67.

[2] L. He, M. Fan, B. Dutcher, S. Cui, X.-D. Shen, Y. Kong, A.G. Russell, P. McCurdy, Dynamic separation of ultradilute CO_2 with a nanoporous amine-based sorbent, Chem. Eng. J. 189–190 (2012) 13–23.

[3] G. Leonzio, P.S. Fennell, N. Shah, A comparative study of different sorbents in the context of direct air capture (DAC): Evaluation of key performance indicators and comparisons, Appl. Sci. (Basel) 12 (2022) 2618.

[4] G. Santori, C. Charalambous, M.-C. Ferrari, S. Brandani, Adsorption artificial tree for atmospheric carbon dioxide capture, purification and compression, Energy (Oxf.) 162 (2018) 1158–1168.

[5] X. Zhu, T. Ge, F. Yang, R. Wang, Design of steam-assisted temperature vacuum-swing adsorption processes for efficient CO_2 capture from ambient air, Renew. Sustain. Energy Rev. 137 (2021) 110651.

[6] Y. Yang, W. Liu, B. Wu, T. Wang, H. Dong, M. Fang, X. Gao, Kinetic research on ion exchange regeneration of quaternary ammonium-based CO_2 sorbent for direct air capture, Sep. Purif. Technol. 324 (2023) 124504.

[7] V. Gama, B. Dantas, O. Sanyal, F.V. Lima, Process operability analysis of membrane-based direct air capture for low-purity CO_2 production, ACS Eng. Au 4 (2024) 394–404.

[8] B.M. Balasubramaniam, P.-T. Thierry, S. Lethier, V. Pugnet, P. Llewellyn, A. Rajendran, Process-performance of solid sorbents for direct air capture (DAC) of CO_2 in optimized temperature-vacuum swing adsorption (TVSA) cycles, Chem. Eng. J. 485 (2024) 149568.

[9] C. Song, Q. Liu, N. Ji, S. Deng, J. Zhao, Y. Li, Y. Kitamura, Reducing the energy consumption of membrane-cryogenic hybrid CO_2 capture by process optimization, Energy (Oxf.) 124 (2017) 29–39.

[10] B. Liu, X. Yang, P.-C. Chiang, T. Wang, Energy consumption analysis of cryogenic-membrane hybrid process for CO_2 capture from CO_2-EOR extraction gas, Aerosol Air Qual. Res. 20 (2020) 820–832.

[11] Z. Zolfaghari, A. Aslani, R. Zahedi, S. Kazzazi, Simulation of carbon dioxide direct air capture plant using potassium hydroxide aqueous solution: Energy optimization and CO_2 purity enhancement, Energy Conversion and Management: X 21 (2024) 100489.

[12] C. Castel, E. Favre, Membrane separations and energy efficiency, J. Memb. Sci. 548 (2018) 345–357.

[13] S.A. Amelkin, A.M. Tsirlin, J.M. Burzler, S. Schubert, K.H. Hoffmann, Minimal work for separation processes of binary mixtures, Open Syst. Inf. Dyn. 10 (2003) 335–349.

[14] L.M. Robeson, The upper bound revisited, J. Memb. Sci. 320 (2008) 390–400.

[15] S. Wang, Z. Su, X. Lu, Energy-consumption analysis of carbon-based material for CO_2 capture process, Fluid Phase Equilib. 510 (2020) 112504.

[16] P. Ignatusha, H. Lin, N. Kapuscinsky, L. Scoles, W. Ma, B. Patarachao, N. Du, Membrane separation technology in direct air capture, Membranes. 14 (2024) 30.

[17] G. Genduso, W. Ogieglo, Y. Wang, I. Pinnau, Carbon molecular sieve gas separation materials and membranes: A comprehensive review, J. Memb. Sci. 699 (2024) 122533.

[18] X. Li, S. Ding, J. Zhang, Z. Wei, Optimizing microstructure of polymer composite membranes by tailoring different ionic liquids to accelerate CO_2 transport, Int. J. Greenhouse Gas Control 101 (2020) 103136.

[19] Y. Kohno, M. Kanakubo, M. Iwaya, Y. Yamato, T. Makino, Ionic liquid mixtures for direct air capture: High CO_2 permeation driven by superior CO_2 absorption with lower absolute enthalpy, ACS Omega 7 (2022) 42155–42162.

[20] H. Wu, X. Li, Y. Li, S. Wang, R. Guo, Z. Jiang, C. Wu, Q. Xin, X. Lu, Facilitated transport mixed matrix membranes incorporated with amine functionalized MCM-41 for enhanced gas separation properties, J. Memb. Sci. 465 (2014) 78–90.

[21] M. Chen, F. Soyekwo, Q. Zhang, C. Hu, A. Zhu, Q. Liu, Graphene oxide nanosheets to improve permeability and selectivity of PIM-1 membrane for carbon dioxide separation, J. Ind. Eng. Chem. 63 (2018) 296–302.

[22] L.S. White, X. Wei, S. Pande, T. Wu, T.C. Merkel, Extended flue gas trials with a membrane-based pilot plant at a one-ton-per-day carbon capture rate, J. Memb. Sci. 496 (2015) 48–57.

[23] F. Moghadam, E. Kamio, H. Matsuyama, High CO_2 separation performance of amino acid ionic liquid-based double network ion gel membranes in low CO_2 concentration gas mixtures under humid conditions, J. Memb. Sci. 525 (2017) 290–297.

[24] W.M. McDanel, M.G. Cowan, N.O. Chisholm, D.L. Gin, R.D. Noble, Fixed-site-carrier facilitated carbon dioxide transport through ionic-liquid-based epoxy-amine ion gel membranes, J. Memb. Sci. 492 (2015) 303–311.

[25] Y. Han, D. Wu, W.S.W. Ho, Nanotube-reinforced facilitated transport membrane for CO_2/N_2 separation with vacuum operation, J. Memb. Sci. 567 (2018) 261–271.

[26] K. Khoiruddin, I.G. Wenten, U.W.R. Siagian, Advancements in bipolar membrane electrodialysis techniques for carbon capture, Langmuir 40 (2024) 9362–9384.

[27] Y. Zhang, X. Ji, Y. Xie, X. Lu, Thermodynamic analysis of CO_2 separation from biogas with conventional ionic liquids, Appl. Energy 217 (2018) 75–87.

[28] H. Machida, R. Ando, T. Esaki, T. Yamaguchi, H. Horizoe, A. Kishimoto, K. Akiyama, M. Nishimura, Low temperature swing process for CO_2 absorption-desorption using phase separation CO_2 capture solvent, Int. J. Greenhouse Gas Control 75 (2018) 1–7.

[29] B. Liu, Y. Lian, S. Li, S. Deng, L. Zhao, B. Chen, D. Wang, Experimental investigation on separation and energy-efficiency performance of temperature swing adsorption system for CO_2 capture, Sep. Purif. Technol. 227 (2019) 115670.

[30] N. Xie, B. Chen, C. Tan, Z. Liu, Energy consumption and exergy analysis of MEA-based and hydrate-based CO_2 separation, Ind. Eng. Chem. Res. 56 (2017) 15094–15101.

[31] S. Fujikawa, R. Selyanchyn, T. Kunitake, A new strategy for membrane-based direct air capture, Polym. J. 53 (2021) 111–119.

[32] Y. Zhang, X. Ji, X. Lu, Energy consumption analysis for CO_2 separation from gas mixtures, Appl. Energy 130 (2014) 237–243.

[33] J. Rumble, CRC handbook for chemistry and physics, CRC Press, Boca Rat, 2021.

Chapter 3 Free-Standing Nanometer-Thick Covalent Organic Framework Films for Separating CO_2 and N_2

3.1 Introduction

The COF is expected to be a high-performance CO_2 separation membrane due to its designable pore characteristics. However, the CO_2/N_2 separation mechanism of COF has not yet been sufficiently explored due to the difficulty of its film preparation. In this chapter, I developed a new method for synthesizing COF films using vapor deposition polymerization, which is a vapor phase synthesis method for organic thin films[1]. The vapor phase synthesis of COFs has been reported for few-molecular-layer COFs on single-crystalline metal substrates for scanning tunneling microscopy (STM) observations [2–4]. However, these films cannot be used in practical membrane-based devices because they are on metal substrates and are not continuous on a large scale.

The difficulty in deposition polymerization is stoichiometry control and substrate removal. These problems were solved by alternately depositing the precursors on a dissolvable substrate with precise control of the thickness of each layer followed by annealing. This chapter focuses on the development of free-standing COF films and evaluating their CO_2/N_2 permeation properties. Free-standing films have great potential

for membrane separation because they can be incorporated into high-flux hollow fiber membranes.

3.2 Experiment

3.2.1 Materials

1,3,5-tris(4-aminophenyl)benzene (TAPB, >93.0%) and naphthalene-1,4,5,8-tetracarboxylic dianhydride (NTCDA, >99%) were purchased from Tokyo Kasei Inc. and used without further purification. The commercial porous anodic aluminum oxide (AAO) support was Whatman® Anodisc Membrane Filters, with a diameter of 13 mm and nominal pore diameter of 0.02 μm. The KCl substrate with (001) polished surface was purchased from OHYO KOKEN KOGYO Co., Ltd. and used without further purification. The Si/SiO_2 wafer was purchased from Graphene Supermarket. The Si/SiO_2 wafer was cut into 1 cm×1 cm substrates and cleaned by the RCA (Radio Corporation of America) cleaning method[5].

3.2.2 Preparation of COF films

COF films with an imide-bonding network structure were prepared using TAPB and NTCDA precursors (Fig. 3-1a). It is generally challenging to synthesize polymer films

with precisely controlled thicknesses and stoichiometries using deposition polymerization in the vapor phase. In order to solve these problems, a new apparatus (Fig. 3-1b) was developed to alternately deposit TAPB and NTCDA on substrates with real-time thickness monitoring using a quartz crystal microbalance (QCM) and automatic source control. Fig. 3-1c schematically illustrates the overall COF film preparation process. A pre-designed amount of NTCDA was deposited on the substrate; the source was switched to TAPB, and the deposition was continued.

In greater detail, the alternating deposition was performed in a vacuum chamber evacuated by a turbo molecular pump (TMP) to a pressure below 5.0×10^{-4} Pa. NTCDA and TAPB (ca. 100 mg) were introduced into separate quartz crucibles and fixed on a carousel at the bottom of the chamber. The precursors were sublimed by a lamp heater and deposited on Si/SiO_2 or KCl substrates. The substrates were placed 5 cm above the deposition source and rotated at 20 rpm to enhance film uniformity [6]. The amounts of deposited precursors were monitored by changing the resonance frequency (Δf) of the QCM (INFICON, 6 MHz). The QCM was maintained at ca. 17 °C by water circulation to avoid desorption of the precursor from the QCM surface and to prevent thermal deviation of the QCM frequency. The thickness and Δf relationship were calibrated by measuring the thickness of the deposited films of each precursor using laser microscopy

(KEYENCE VX-8700). First, NTCDA was deposited on the substrate. The carousel was then rotated, and TAPB was deposited on the substrate. The rotation of the precursor carousel and intensity of the lamp heater were automatically controlled by a computer program that monitored the QCM. The precursor deposition rate was 0.1 nm s^{-1}. By repeating these operations 25–100 times, the alternately deposited film was prepared.

After alternating depositions, the film was removed from the chamber and annealed under vacuum conditions (<10 Pa) in a glass tube to facilitate the imide-forming reaction between the precursors. This annealing caused partial desorption of the precursors, and the optimal ratio of the precursors in the as-deposited films was dependent on the annealing conditions, as explained in the Results and Discussion section.

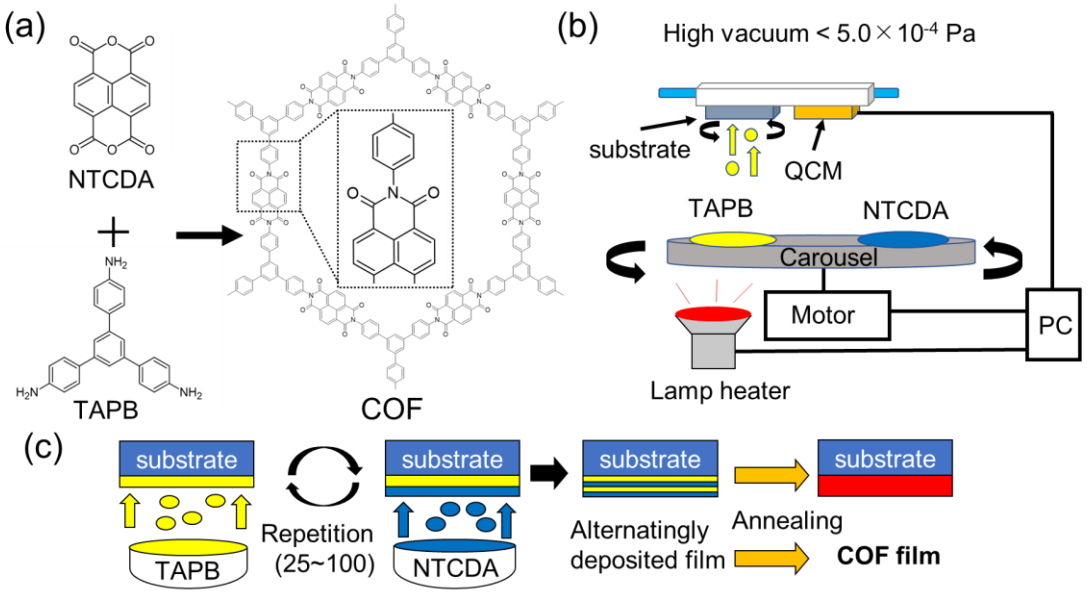

Fig. 3-1. (a) Structure of COF and its precursors (NTCDA and TAPB). (b) Schematic illustration of the deposition apparatus. (c) Schematic illustration of alternating deposition used to prepare the COF film.

3.2.3 Characterization of the COF films

Fourier transform infrared (FTIR) spectroscopy was performed using a JASCO FT/IR-4700 spectrometer with a 4 cm^{-1} resolution. The COF films and precursor powders were measured using the transmission method on a KCl substrate and the attenuated total reflection method, respectively. Atomic force microscope (AFM) images were obtained using a Hitachi High-Tech Corp. (SPA-400) in tapping mode. Scanning transmission electron microscopy (STEM) was performed using an aberration-corrected FEI Titan3 G2 60–300 at an acceleration voltage of 60 kV. Small-angle X-ray scattering (SAXS) measurements were conducted using a Rigaku Nano-viewer IPA with an exposure time of 4.5 h. A KEYENCE VX-8700 laser microscope was employed to measure the film

thickness using a step between the film and the substrate. It has also been used for the observation of free-standing films.

3.2.4 Gas permeation measurements

Gas permeation measurements were conducted using a homemade apparatus based on the differential-pressure methods (ISO 15105-1:2007). The general operation is described in Chapter 1. The COF film was prepared on a KCl (001) single-crystal substrate, and the sample was gently placed in water. KCl was then dissolved, and the COF film floated on the surface. Next, the free-standing film was lifted off by AAO support. The COF film on the support was dried in ambient atmosphere and then glued onto a separator with an NW-KF25 flange using a vacuum-compatible epoxy resin (Stycast 2850G). The COF separator was positioned between the supply gas manifold and the partial pressure measurement chamber. The residual gas on both sides was removed to achieve a high vacuum lower than 5×10^{-5} Pa by TMP pumping for over 12 h. The pressures of the feed and permeate gases were measured using a capacitance gauge (CANON ANELVA, M342DG-13) and a crystal-and-cold-cathode combination gauge (Tokyo Electronics Co., cc-10), respectively. The gas species used were pure CO_2, pure N_2, and a CO_2/N_2 mixture (1:1). The gas components on the permeate side were determined using QMS

(INFICON, Transpector2) with differential pumping. All measurements were repeated at least three times. The graph plots and error bars in graph show the average and standard error of the experiments, respectively.

3.2.5 Numerical analysis of gas permeation through the COF films

The gas permeation performance of the COF film was evaluated by numerical analysis based on dual-site sorption with a partial immobilization model. The model equations are described in section 1.2.3, Chapters 1. Generally, dual-mode sorption parameters ($C'_{\mathrm{H}}, b,$ and k_{D}) can be obtained by nonlinear curve fitting of the experimental gas sorption isotherms using Eq. (1.4). However, the number of gases absorbed in the COF film prepared by alternating deposition cannot be experimentally measured because its thickness is extremely low. The parameters were determined by numerically solving Eq. (1.7) using the finite differential method and adjusting the solution to the experimental permeation curve. An analysis program was built using Python 3.7.1. Eq. (1.7) was numerically solved using the Crank–Nicolson and Gauss–Seidel methods. Appropriate parameters were calculated by minimizing the residual sum of squares of the numerical solution and experimental data. Algorithms for searching for the minimum value used the differential-evolution method, which can search for the global minimum of a system.

3.2.6 DFT calculation

The interaction energy between the COF and gas molecules was calculated using the density functional theory (DFT). Calculations were performed using the Gaussian 16W package[7]. To consider the weak interactions between the atoms, the D3 dispersion correction reported by Grimme was included in the DFT calculations (DFT-D) [8]. Basis sets of the 6-31 G (d) [9] and B3LYP [10,11] functionals were used for structural optimization. The total energies of the optimized structures were calculated using the 6-311G (d) basis sets and B3LYP functional. The basis set superposition error was corrected using the counterpoise method [12].

The interaction energies between the COF and the gas molecules (ΔE) were calculated using the following equation (Eq. (3.1)).

$$\Delta E = E_{\mathrm{COF+gas}} - \left(E_{\mathrm{COF}} + E_{\mathrm{gas}}\right) \tag{3.1}$$

where $E_{\mathrm{COF+gas}}$ is the total energy of the COF with gas molecules at a binding site and E_{COF} and E_{gas} are the energies of the COF and gas molecules, respectively.

3.3 Results and Discussion

3.3.1 Preparation and characterization of COF films

Fig. 3-2 shows the recorded decrease in the QCM frequency, which corresponds to the deposited amounts of TAPB and NTCDA. The stepwise decrease at 16 Hz and 9 Hz indicated that the cycle was successfully controlled. The thickness of each layer was set to 1-2 nm and no significant difference in the film structure and properties was observed by changing this parameter. Precursors were repeatedly deposited 25–100 times to prepare alternately deposited films. The film was annealed in vacuum to facilitate the imide-forming reaction between TAPB and NTCDA. Many experiments were performed with different monomer ratios, annealing temperatures, and annealing periods for prescreening. I found that these factors are interconnected, i.e., the optimum stoichiometry can be achieved under different annealing conditions by adjusting the monomer ratio.

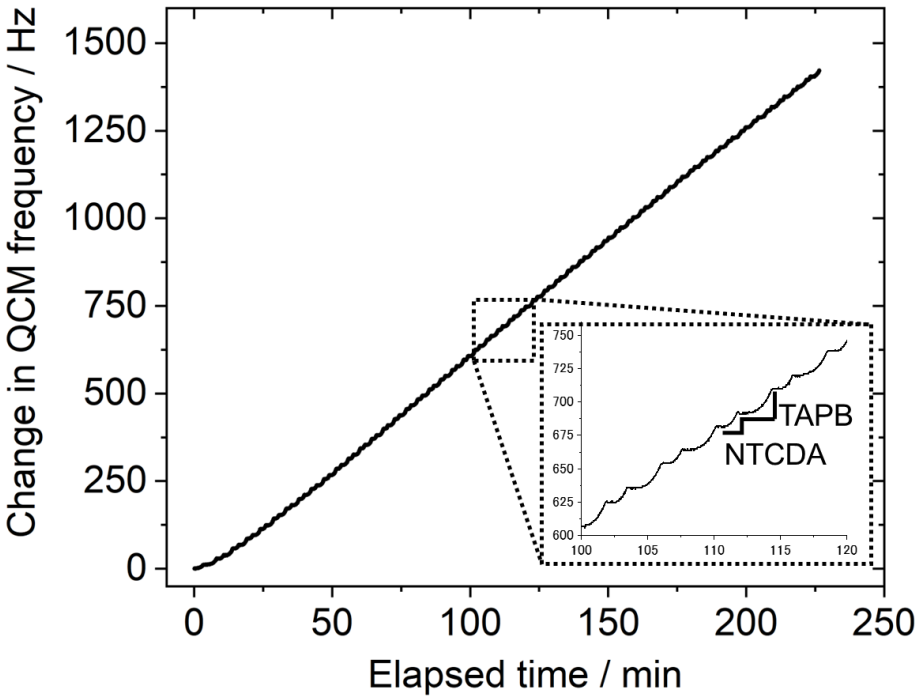

Fig. 3-2. A decrease in the QCM frequency, which corresponds to the deposited amounts of TAPB and NTCDA, occurred in a stepwise manner.

In the following section, I will explain the results of two types of COF films with an upper limit and lower limit for obtaining films of high quality (FTIR-based), as shown in Table 3-1. The conditions were optimized by controlling three parameters: the deposition ratio (weight ratio) of TAPB and NTCDA, temperature, and time during annealing in vacuum. Because partial evaporation occurred during vacuum annealing, stoichiometry control requires optimization of the precursor ratio depending on the annealing conditions. This was performed using FTIR, as described in the following table.

Table 3-1. Conditions to synthesize two types of COF films

Sample name	TAPB : NTCDA deposition ratio	Annealing temperature	Annealing time
"HTA"(high temperature annealed)	1 : 1.2	400 ℃	10 min
"LTA" (low temperature annealed)	1 : 2.5	275 ℃	12 h

Figure 3-3a shows the FTIR spectra of the film with a TAPB: NTCDA = 1:1.2 annealed at various temperatures, including those of an as-deposited film and each precursor. The "b" symbols denote the peaks from unreacted species (3353 cm^{-1} and 1607 cm^{-1} from $-NH_2$ of TAPB, 1781 cm^{-1} from C=O of NTCDA), whereas "a" denotes those from the imide-bonded species (1714 cm^{-1} and 1673 cm^{-1} from the symmetric and asymmetric vibrations of C=O, respectively; 1344 cm^{-1} from –C–N–C– stretching [13]). As the imide-forming reaction was complete, the "b" peaks disappeared and the "a" peaks became relatively strong. Notably, the total absorption intensity decreased because of the desorption of precursor molecules that occurred during an annealing. Fig. 3-3b shows the FTIR spectra under the same annealing conditions (400 °C, 10 min, high-temperature annealed (HTA)-COF afterward) of the precursor films but with various TAPB: NTCDA ratios. The "b" peaks of the unreacted precursors disappeared when the ratio of TAPB: NTCDA was 1:1.2. This result indicates that the optimum precursor ratio depends on the annealing conditions. Using the same procedure (Fig. 3-3c), the

optimum annealing conditions for the precursor ratio of TAPB: NTCDA =1:2.5 was determined to be 275 °C for 12 h (low-temperature annealed (LTA)-COF).

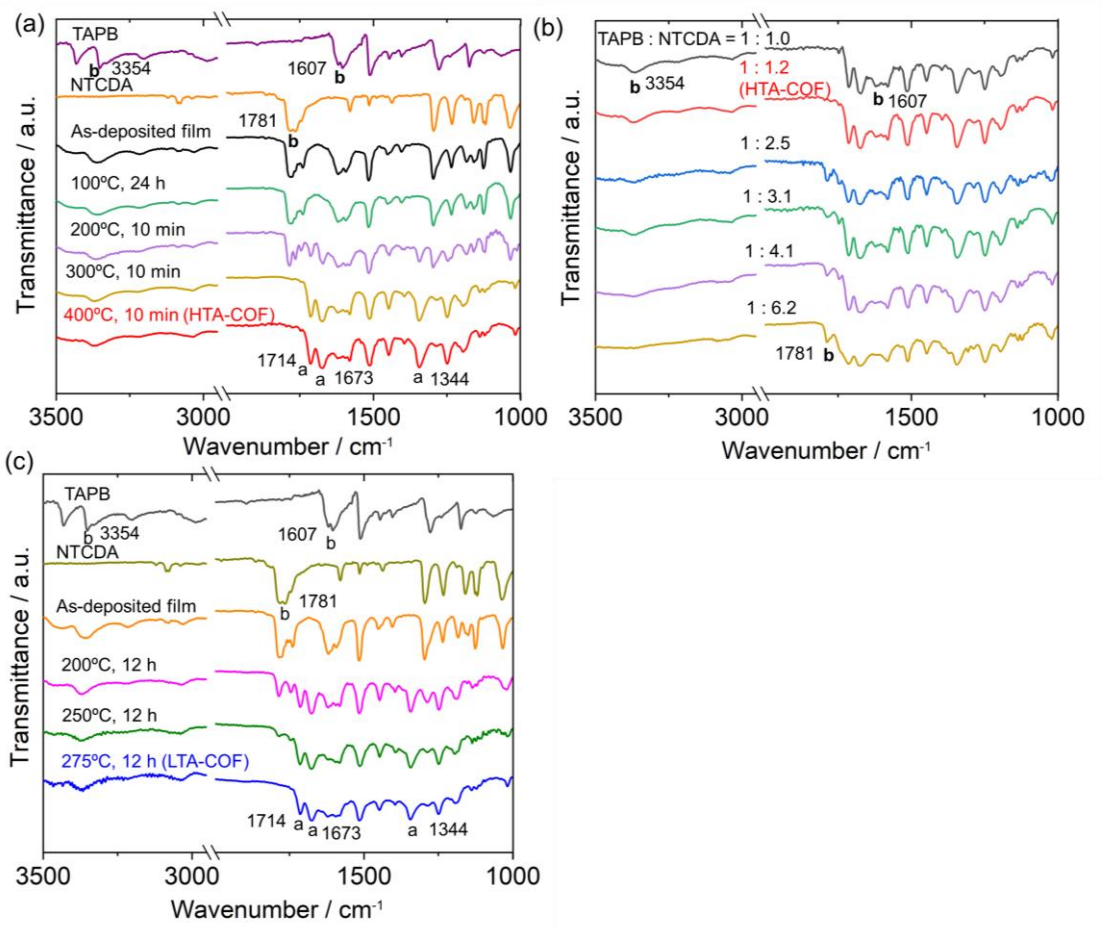

Fig. 3-3. FTIR analyses. (a) Films prepared with TAPB: NTCDA =1:1.2 measured before and after vacuum annealing at various temperatures. (b) Effect of precursor ratio of COF films annealed at 400 °C for 10 min. (c) Precursors, as-deposited film (deposition ratio of TAPB: NTCDA =1:2.5), and as-deposited films annealed at various temperatures for 12 h. Peaks marked with "b" correspond to precursors and those with "a" correspond to the imide group formed by polymerization.

Free-standing COF films were prepared by depositing precursors on water-soluble KCl substrates, followed by annealing and dissolving the substrates in water. These were obtained as floating objects on the water surface, as shown in Fig. 3-4a. The film can be lifted and transferred to any substrate from the water surface. Figure 3-4b shows an optical image of the COF film placed on a metal ring to partly cover the hole, in which the center part of the film was not supported by anything. Figure 3-4c shows a laser microscope image of the COF film on the Si substrate. An interference fringe of the laser light was observed due to the deviation in the air-gap thickness, which shows the smoothness and uniformity of the film. Figures 3-4d to f shows optical images of the COF films transferred to various substrates including sapphire, glass, and AAO supports obtained using the same method.

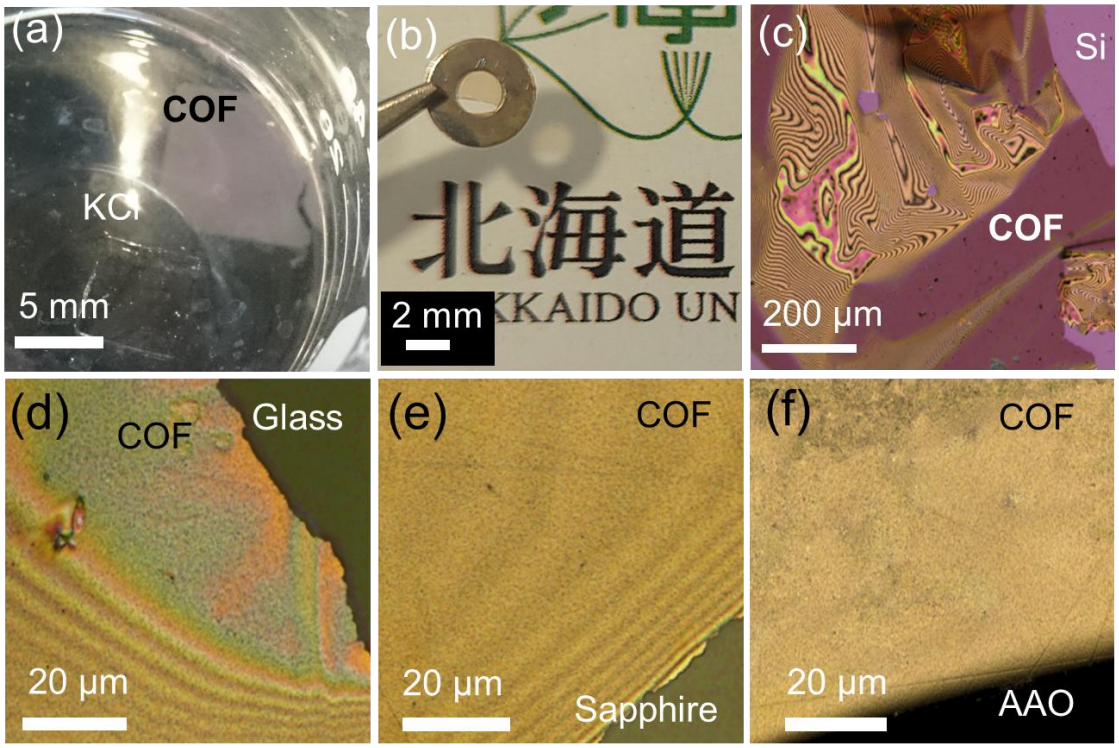

Fig. 3-4. Free-standing COF films. Optical images of (a) COF film floated on water by dissolving the KCl substrate and (b) free-standing COF film supported by a metal ring. Laser microscope image of a COF film lifted off by a (c) Si substrate, (d) a glass substrate, (e) a sapphire substrate, and (f) a AAO support.

The nanostructures of the free-standing COF films were evaluated using STEM with atomic resolution. Figure 3-5a shows a STEM image of the HTA-COF film transferred onto a TEM grid, which shows the typical overall structure of the HTA film. At higher magnification, a randomly oriented network structure was observed (Fig. 3-5b). Pore structures with a size of 2.4–3.6 nm are clearly identified in Fig. 3-5c by magnifying a part of Fig. 3-5b (the DFT-calculated ideal COF structure is inserted). This pore size

is close to that predicted previously (2.9 nm) for COF synthesized from the same precursors [13].

On the other hand, I did not reveal a pore structure in the LTA-COF films (Fig. 3-5d to 3-5f). The difference between the HTA- and LTA-COF is in accordance with previous reports, which showed that the morphology of the COF was dependent on the monomer concentration during synthesis [14]. It was also reported that a low-temperature reaction causes poor formation of network pore structures [15]. The present results indicate that the monomer ratio and annealing conditions are important for finely tuning the network structure of COF during alternating deposition.

The SAXS pattern of the free-standing HTA-COF films (Fig. 3-6a) showed a broad peak. The peak top placed at q = ca.1.5 nm^{-1} ($d = 2\pi/q = 4.19$ nm) corresponding to the spacing of $(\sqrt{3}\,d)/2$ = 3.6 nm for the hexagonal lattice, which was a slightly greater size than the (100) spacing of the bulk COF [13]. This enlargement was due to the warping and entanglement of the layers, which is consistent with the gas permeation results (Fig. 3-6b).

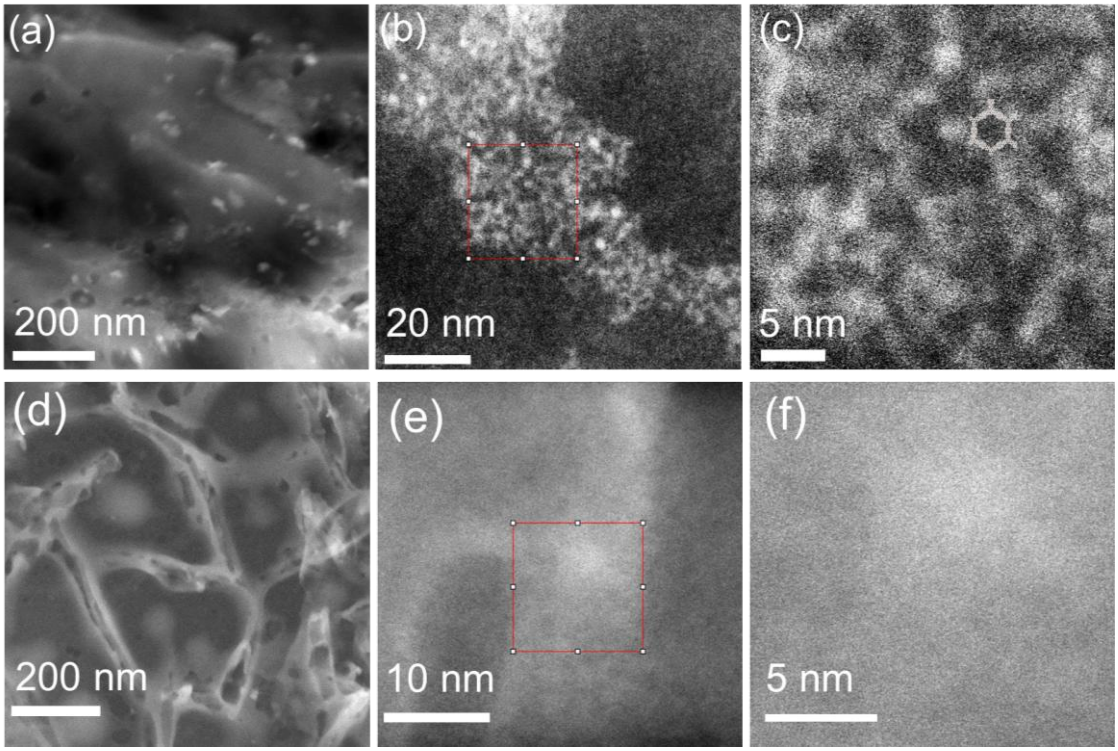

Fig. 3-5. STEM HAADF images. (a) low magnification and, (b) high magnification images of free-standing HTA-COF film, and (c) the enlarged view of (b) in the red square area. The DFT-calculated COF image was inserted. (d) low magnification, (e) high magnification, and (f) enlarged view of (e) in the red square area for LTA-COF films.

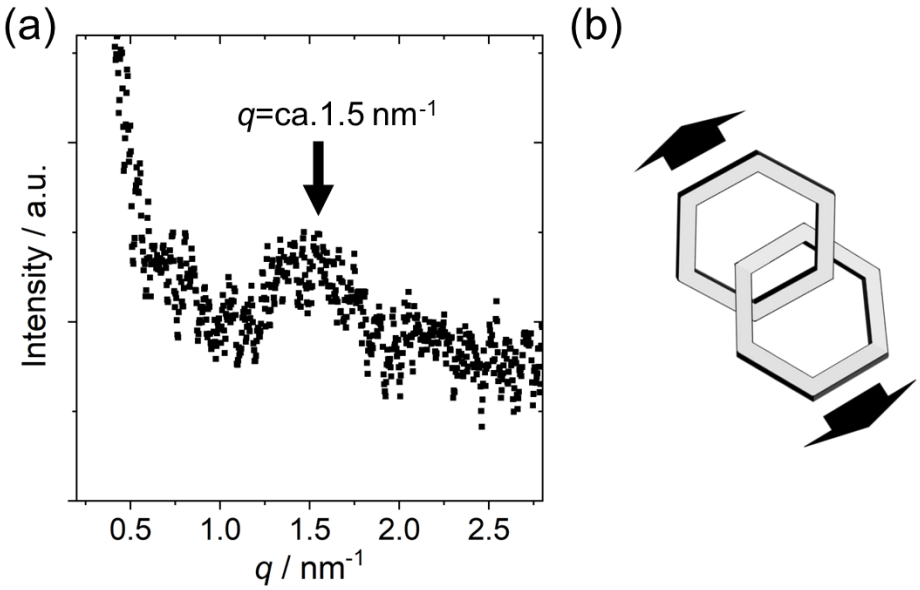

Fig. 3-6. (a) SAXS profile of the free-standing HTA-COF film. (b) Schematic illustration of pore entanglement in the HTA-COF film.

The absolute thickness of the COF films grown directly on Si wafers was calibrated using a laser microscope (Fig. 3-7a). This thickness was consistent with the AFM measurement using the partial scraping method (Fig. 3-7b). The thickness increases linearly with the number of repetitions. Annealing caused a decrease in thickness by a factor of 0.52 (for HTA; 0.42 for LTA (the plot is not shown)), while the linearity with the repetition number was maintained. This thinning was due to the sublimation of the unreacted precursors. It has been revealed that COF films with thicknesses precisely controlled at the nanometer scale can be prepared by alternating depositions.

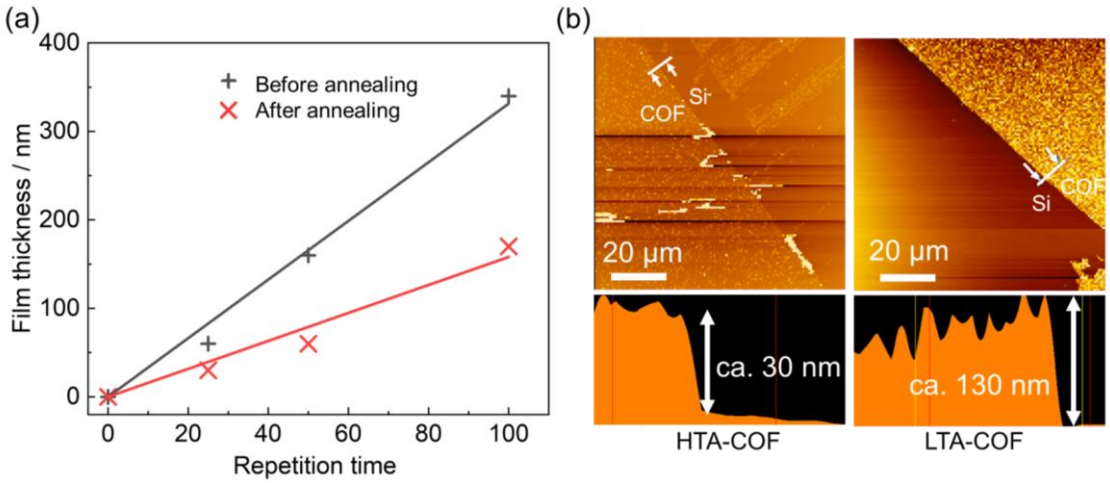

Fig. 3-7. (a) Thickness of the HTA-COF film at various repetition times (0–100). The black "+" and red " x " marks denote the film thickness before and after annealing, respectively. The black and red lines represent the linear regression lines of each dataset. (b) AFM measurements at scraped edges of HTA-COF and LTA-COF films grown on Si/ SiO_2 wafers at different repetition times. The height profile represented the white lines in Figs.

The chemical stability of the HTA-COF films was evaluated by immersing them in concentrated HCl aq. (12 M), NaOH aq. (1.3 M), toluene, tetrahydrofuran (THF), ethanol (EtOH), dichloromethane (CH_2Cl_2), and acetone for 24 h. The FTIR peak characteristics of the imide bonding were maintained even after immersing the films in these chemicals (Fig. 3-8a). This result indicated that the COF films had high stability against acids and organic solvents because the network structure composed of the imide bonding reinforced the chemical stability. The COF showed a relatively low resistivity to NaOH(aq) because the imide bond was hydrolyzed by a base [16]. The thermal stability of the HTA-COF films was examined. The imide peaks are maintained after annealing at 400 °C for 12 h (Fig. 3-8b). This indicates that the HTA-COF possesses good thermal stability, not only for the powder [17,18] but also for the film type.

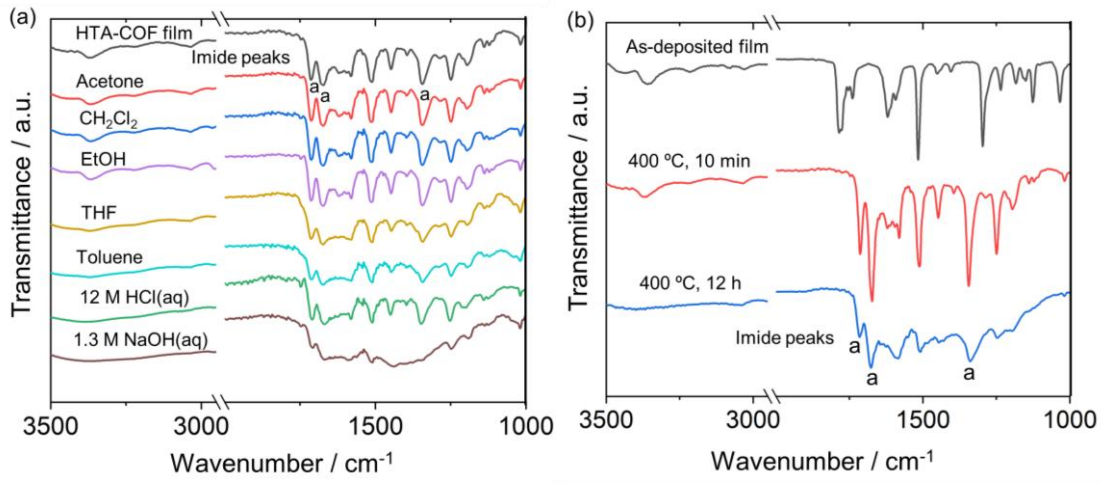

Fig. 3-8. FTIR spectra of HTA-COF films (a) before and after immersion in various solvents for 24 h. (b) for the long-term thermal stability test.

3.3.2 CO_2 and N_2 permeation properties

The gas separation properties of the free-standing COF films were investigated. The film thicknesses of the HTA- and LTA-COFs were estimated to be ca. 50 and 100 nm, respectively, from the sample prepared under the same experimental conditions shown in Fig. 3-8b. As the CO_2 and N_2 permeances of the AAO support were sufficiently greater than those of the COF film, the effect of the AAO support was negligible.

Figure 3-9a shows the CO_2 or N_2 permeances and CO_2/N_2 ideal selectivity for the HTA-COF film of pure CO_2 or N_2 permeated through the film at transmembrane pressures of 10^3 to 10^5 Pa. The difference between CO_2 and N_2 was highest when the transmembrane pressure was 10^5 Pa. The permeances of CO_2 and N_2 were 1.79×10^{-8} and 0.39×10^{-8} mol m^{-2} Pa^{-1} s^{-1}, respectively. Thus, the ideal CO_2/N_2 selectivity at 10^5 Pa was calculated to be 4.58 (Table 3-2). The pore size of HTA-COF ranged between 2.4 and 3.6 nm based on the STEM observations, which is far greater than the kinetic diameters of CO_2 and N_2 (0.33 and 0.36 nm, respectively) [19]. Based on this result, it is presumed that the CO_2/N_2 selectivity is not due to a molecular sieving effect but to differences in the solution–diffusion mechanism between CO_2 and N_2 in the films.

When the transmembrane pressure was 10^5 Pa, the CO_2 and N_2 permeance of the LTA-COF film were 5.7×10^{-10} and 1.2×10^{-10} mol m^{-2} Pa^{-1} s^{-1}, respectively (Table 3-2).

These values are lower than the CO_2 and N_2 permeances of the HTA-COF film by factors of 31.4 and 32.5 times, respectively. This tendency, in which the LTA-COF film permeance was lower than that of the HTA-COF film, was observed at all measured transmembrane pressures (10^3-10^5 Pa) (Fig. 3-9b). I consider the mechanism for this difference to be due to the HTA-COF films having partially oriented pores that formed short gas permeation paths, as determined by STEM, whereas the LTA-COF films did not have these paths.

The CO_2/N_2 separation factor of the HTA-COF films was measured using a CO_2/N_2 mixture (molar ratio=1:1). There were no significant differences between the CO_2/N_2 separation factor and CO_2/N_2 ideal selectivity for the HTA-COF film at transmembrane pressures of 10^3-10^5 Pa (Fig. 3-9c).

These results suggest that the diffusion effect was dominant in the HTA-COF films due to the partially oriented pores. This model agrees with the fact that the value of the CO_2–N_2 separation factor for the HTA-COF film (4.66) is approximately in agreement with that of the CO_2/N_2 ideal selectivity (4.58). In addition, the HTA-COF film had almost no contribution to the molecular sieve effect[20], in which N_2 was prevented from permeating when the adsorption sites on the pore wall were occupied with CO_2.

However, the CO_2/N_2 separation factor of the LTA-COF film (3.83) was lower than that of the CO_2/N_2 ideal selectivity (4.79). This indicates that adsorption and solution effects played important roles during permeation through the LTA-COF films. The mechanism is that the diffusion is hindered in the LTA-COF films due to the lack of ordered structures.

Table 3-2. CO_2 and N_2 permeance, CO_2/N_2 ideal selectivity and CO_2/N_2 separation factors of HTA-, LTA- COF films and AAO support at the transmembrane pressure=10^5 Pa

	CO_2 permeance [a]	N_2 permeance [a]	CO_2/N_2 ideal selectivity	CO_2/N_2 separation factor
HTA-COF film	1.8±0.2	0.39±0.04	4.6±0.8	4.7±0.3
LTA-COF film	0.057±0.004	0.012±0.002	4.8 ± 0.9	3.8±0.4
AAO support	142 ± 2	133 ± 0.4	1.06±0.02	1.54±0.02

[a] Unit: 10^{-8} mol m^{-2} Pa^{-1} s^{-1}

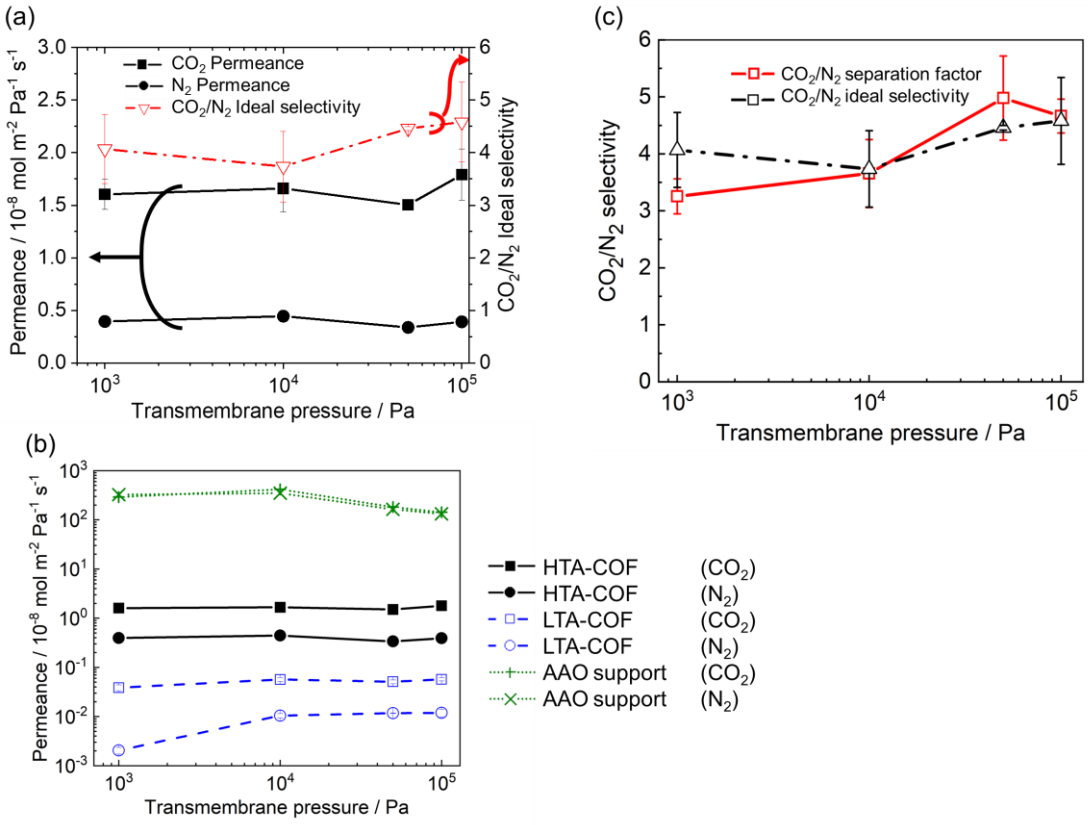

Fig. 3-9. Gas permeation characteristics of the COF film. (a) CO_2 and N_2 permeances and CO_2/N_2 ideal selectivity of the HTA-COF film at transmembrane pressures of 10^3–10^5 Pa. (b) CO_2 and N_2 gas permeances of the HTA-COF films, LTA-COF films, and AAO support at transmembrane pressures of 10^3–10^5 Pa. (c) Pressure dependence of the CO_2/N_2 separation factor and CO_2/N_2 ideal selectivity for the HTA-COF film.

3.3.3 Examination of absorption behavior of the COF film

The gas absorption behavior of the COF films was examined to understand their permeation mechanism further. The CO_2 absorption was evaluated by FTIR using the apparatus shown in Fig. 3-10a. The HTA-COF film grown on NaCl was placed in the chamber, and FTIR was measured with 1 atm air and CO_2 filling the chamber at room temperature. The peak positions of the imide C=O symmetric and asymmetric vibration peaks are shifted by 3 cm^{-1} and 1 cm^{-1}, respectively, when CO_2 is introduced into the chamber (Fig. 3-10b with dips). It is reported that the proxy and ethoxy-based polymers exhibited a peak shift by 2.0 cm^{-1} and 3.7 cm^{-1} to the higher wavenumber side when the CO_2 absorption occurred [21]. Thus, it was estimated that the imide of – C=O in the COF film acted as a CO_2 absorption site.

DFT-D calculations were conducted to observe the gas-absorption behavior further. The calculations predicted that the adsorption site of the gas molecules in the COF was the O atom of the imide group (Fig. 3-11). Interestingly, CO_2 was absorbed onto the site at a distance of 2.84 Å, which was much closer than that of N_2 (3.25 Å). The calculations also predicted that the COF has higher affinities to CO_2 than N_2 at the ΔE of -17.2 kJ mol^{-1} vs. -9.0 kJ mol^{-1}, which are consistent with the experimental isosteric heat of adsorption from a previous report [13].

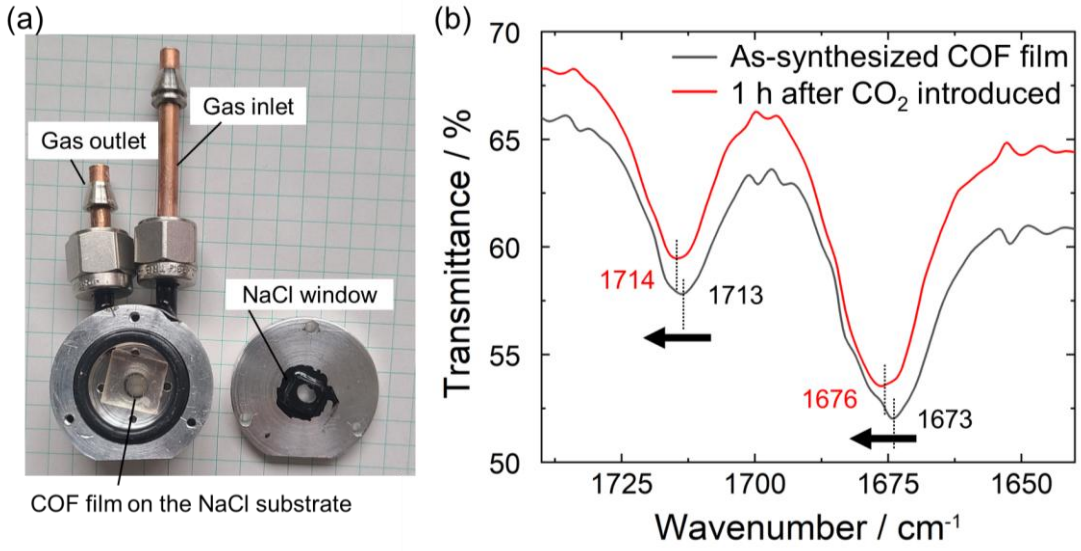

Fig. 3-10. (a) IR measurement apparatus for CO_2 adsorption in COF films. (b) FTIR spectra before and after CO_2 was introduced into the chamber. The dips correspond to the symmetric and asymmetric stretching of imide C=O.

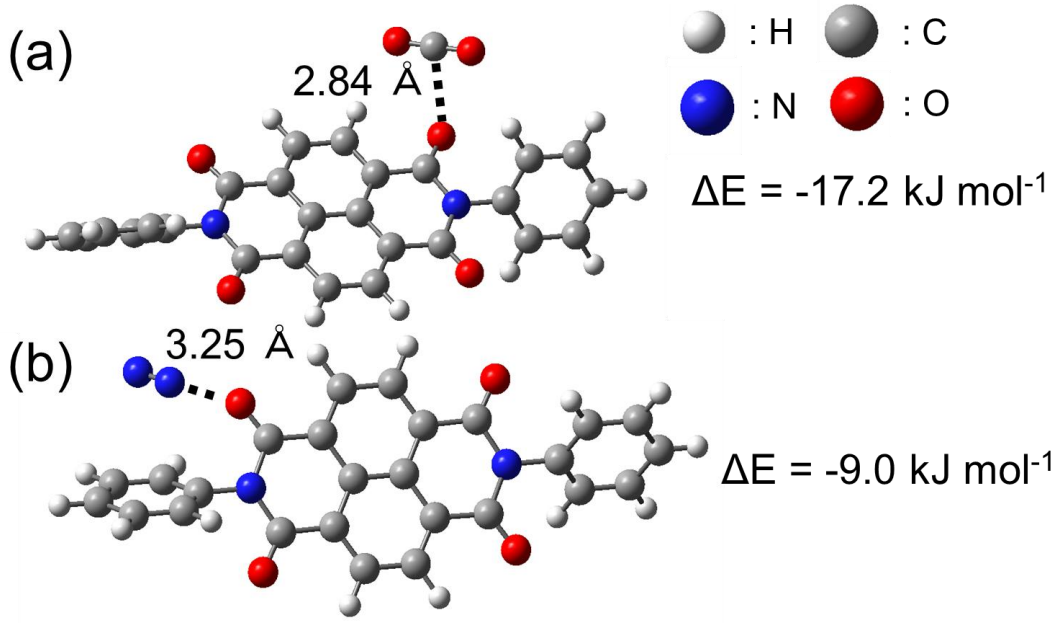

Fig. 3-11. Optimized binding structures and binding energies for (a) CO_2 and (b) N_2 with a model partial COF structure.

3.3.4 Mechanism of gas permeation through the COF films

The mechanism of gas permeation through COF films has not been discussed by applying quantitative model parameters, probably because it is difficult to use well-defined and uniform samples. Partial immobilization and dual-mode sorption models were used. The model parameters were determined by a numerical solution and experimental gas permeation data using least-squares genetic algorithm fitting. This approach has the advantage of obtaining solubility and diffusivity parameters only from permeation data. Figure 3-12 and Table. 3-3 show the fitting results. The HTA-COF film had greater k_D, C_H', and b values for CO_2 (8.45×10^{-5}, 1.0×10^{5}, and 3.51×10^{-5}, respectively) than for N_2 (1.0×10^{-5}, 8.56×10^{4}, 1.0×10^{-5}). This shows that the HTA-COF film has a greater solubility of CO_2 than N_2 in both the matrix and void regions, which is consistent with the DFT result of the greater interaction energy of CO_2 than that of N_2 in the imide groups of COF.

The b values of CO_2 and N_2 in the HTA-COF films were in the range of 10^{-5} to 10^{-4} Pa^{-1}, which indicated that at a high feed gas pressure, the pores in the COF film were saturated by gas molecules, and gas permeation through the films was governed by a Henry sorption mechanism. The b values of the LTA-COF film were not significantly different from those of the HTA-COF film, whereas the k_D and C_H' of the LTA-COF film

were significantly higher and lower than those of the HTA-COF film. These results suggest that the gas molecules in the LTA-COF film were more easily adsorbed in the matrix region than in the void region because the LTA-COF film was structureless.

In both the matrix and void regions, the diffusivity coefficient of the HTA-COF film was significantly greater than that of the LTA-COF film. Thus, it was estimated that the pore structures in the HTA-COF film function as diffusion pathways for gas molecules. The absence of gating effects in our results, in which CO_2 blocks the permeation of N_2, can be explained as follows. The pore size of our COF is greater than the molecular size, even with entanglement and interpenetration, and N_2 permeation was not blocked by absorbed CO_2. Designing and synthesizing COF membranes with narrower pore sizes will realize gating effects and interesting functions of the separation films. The discussion above can be summarized as follows:

(1) Both the matrix (solvation of gas to the polymer followed by diffusion) and voids (diffusion on the channel surface) contribute to the selectivity.

(2) The selectivity arises from the stronger interaction between CO_2 and the polymer, which increases the CO_2 solubilities of both the matrix and void (Fig. 3-13a).

(3) The difference in the selectivity and permeation between HTA-COF and LTA-COF arises from the ordering of the void channel, which is consistent with the STEM images (Fig. 3-13b).

(4) The "molecular sieving effect" was not observed because the void size was much greater than that of CO_2 or N_2.

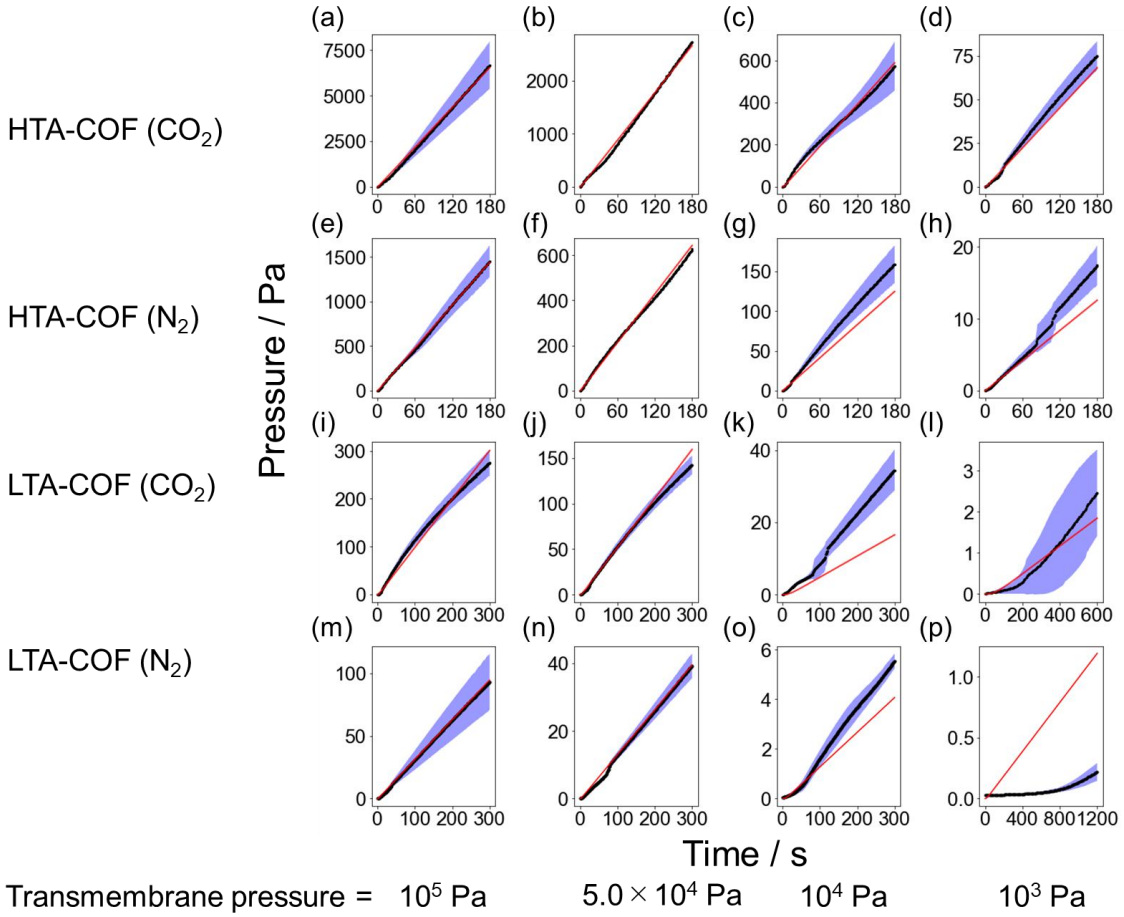

Fig. 3-12. Model fitting to the experimental gas permeation data. The black and red curves represent the experimental and fitted results, respectively. The blue bands show the deviation of the experimental data (repeated three or more times). (a)–(d) HTA-COF (CO_2), (e)–(h) HTA-COF (N_2), (i)–(l) LTA-COF (CO_2), (m)–(p) LTA-COF (N_2).

Table 3-3. Dual mode sorption and partial immobilization parameters for HTA- and LTA-COF films

Film	Gas	k_D [i]	C_H' [ii]	b [iii]	D_D [iv]	D_H [v]
HTA	CO_2	8.47×10^{-5}	1.00×10^{5}	3.51×10^{-5}	2.14×10^{-12}	2.61×10^{-16}
	N_2	1.00×10^{-5}	8.56×10^{4}	1.00×10^{-5}	8.37×10^{-12}	1.31×10^{-15}
LTA	CO_2	1.67×10^{-2}	5.92×10^{3}	1.00×10^{-4}	8.63×10^{-16}	6.99×10^{-22}
	N_2	1.64×10^{-3}	1.04×10^{3}	4.89×10^{-5}	2.73×10^{-15}	2.45×10^{-19}

i Henry's law constant. Unit: mol m^{-3} Pa^{-1}

ii Langmuir capacity. Unit: mol m^{-3}

iii Langmuir affinity constant Unit: Pa^{-1}

iv Diffusion coefficient in the matrix region Unit: m^2 s^{-1}

v Diffusion coefficient in the void region Unit: m^2 s^{-1}

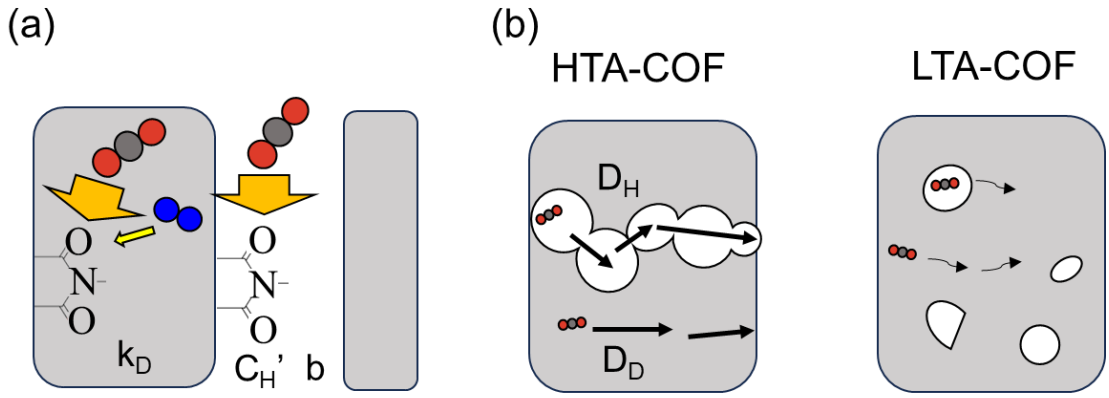

Fig. 3-13. Schematic illustration of estimated gas permeation mechanism through HTA- and LTA-COF films. (a) solubility rerated parameters of k_D, C_H', and b. (b) diffusivity rerated parameters of D_H and D_D

3.3.5 Comparison with the literature for CO_2/N_2 membrane separation

The CO_2/N_2 separation performances of the HTA- and LTA-COF films were compared with those of COF-based membranes (Table 3-4). The NCOFM-0 exhibited the greatest CO_2/N_2 separation performance under humid conditions.

Under dry conditions, the CO_2/N_2 separation performance of the HTA-COF film was 1.4 to 5.8 times greater than that of COF membranes reported in the literature. However, the CO_2 permeability of the HTA-COF membrane was 5–16 times lower than that of the COF membrane reported in the literature. This value can be improved by increasing the crystallinity of the COF film, because the orientation of the COF pores plays a crucial role in fast gas permeation. The CO_2/N_2 separation performance of the HTA- and LTA-COF films did not exceed the upper bounds of polymeric membranes in the literature (Fig. 3-14). Although further improvement of the performance of COF membranes will be required by finely tuning the COF skeletons, I confirmed that COF films prepared by the alternating deposition method are promising candidate materials for next-generation CO_2/N_2 separation membranes.

Table 3-4. Comparison with the literature COF for CO_2/N_2 separation

Name	Thickness /μm	CO_2 permeability / Barrer	CO_2/N_2 selectivity	Ref.
COF–LZU1–ACOF-1	1	27.4	3.3	[22]
NCOFM-0	0.2	36.8	25	[23]
TpHz COF	0.290	20.6	0.79	[24]
TpAzo	0.800	44.9	1	[25]
TpEBr@TpPa–SO_3Na iCON	0.041	4.65	1.5	[26]
$TpTG_{Cl}$@TpPa–SO_3H	0.155	12.9	1.3	[27]
PATA	0.92	975	31	[28]
HTA-COF	ca. 0.050	2.69	4.6	**This work**
LTA-COF	ca. 0.10	0.17	4.8	**This work**

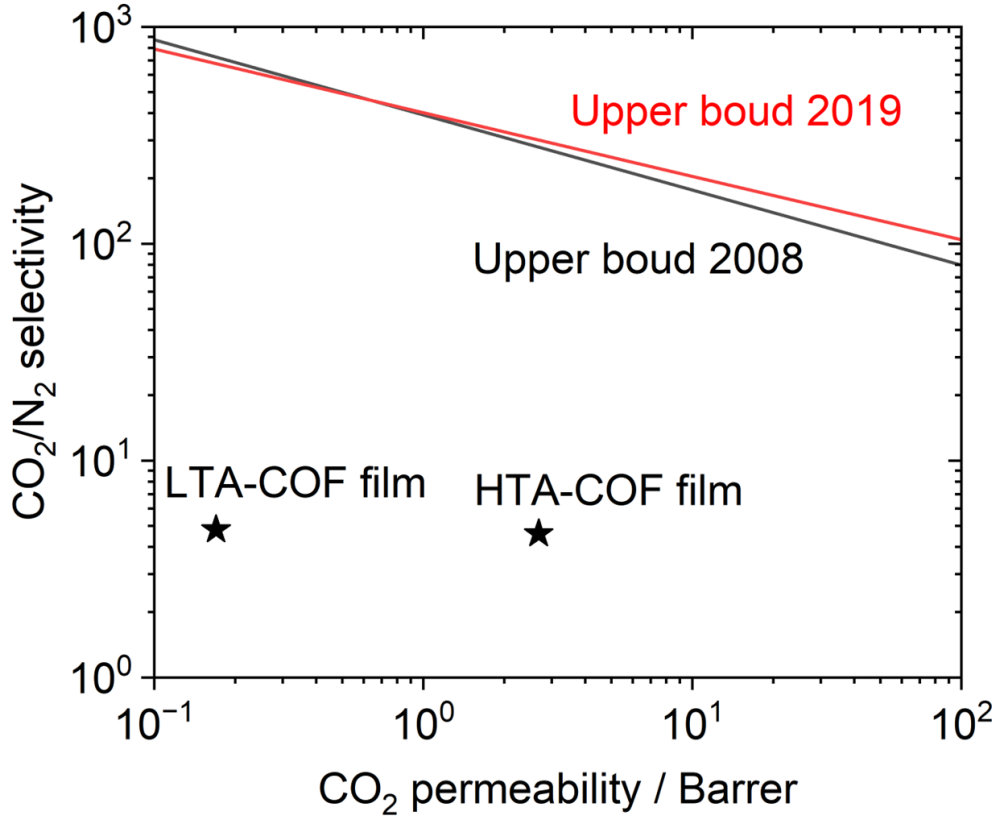

Fig. 3-14. Comparison with literature polymeric membranes for CO_2/N_2 separation. The red and black lines represent Robeson's upper bound (trade-off relationship of conventional polymeric membranes) in 2019 and 2008, respectively.

3.4 Conclusion

I have demonstrated the development of free-standing nanometer-thick COF films with practical gas-separating capabilities. The films were prepared using digital alternating deposition of the precursor molecules, which guarantees a precisely controlled stoichiometry required for applying different annealing conditions for the COF-forming reactions. Under certain annealing conditions, atomic-scale oriented network structures were observed using STEM, resulting in a higher CO_2/N_2 separation ratio. Based on quantum chemical calculations, the CO_2 and N_2 adsorption sites are the O atoms of the imide group. The difference in adsorption energies governs the role of surface diffusion on the pore wall during permeation. These results provide a new practical technique for the preparation of free-standing COF films with well-defined structures and shed light on their gas separation applications.

In addition, the model equations were numerically solved using dual-mode sorption with a partial immobilization model along with a finite differential model. This analysis is a facile method for analyzing the permeation properties of not only COF but also various ultrathin films. By adjusting the solution parameters to the experimental data, appropriate model parameters of the COF films were determined, and it was found that the solubility selectivity mainly contributed to the selectivity.

References

[1] 高橋 善和, 飯島 幸之助, 稲川 正行, 伊藤 昭夫, 真空中での芳香族ポリイミドの合成, 真空 28 (1985) 440−442.

[2] R. Gutzler, H. Walch, G. Eder, S. Kloft, W.M. Heckl, M. Lackinger, Surface mediated synthesis of 2D covalent organic frameworks: 1,3,5-tris(4-bromophenyl)benzene on graphite(001), Cu(111), and Ag(110), Chem. Commun. 29 (2009) 4456.

[3] N.A.A. Zwaneveld, R. Pawlak, M. Abel, D. Catalin, D. Gigmes, D. Bertin, L. Porte, Organized formation of 2D extended covalent organic frameworks at surfaces, J. Am. Chem. Soc. 130 (2008) 6678–6679.

[4] T. Joshi, C. Chen, H. Li, C.S. Diercks, G. Wang, P.J. Waller, H. Li, J.-L. Bredas, O.M. Yaghi, M.F. Crommie, Local electronic structure of molecular heterojunctions in a single-layer 2D covalent organic framework, Adv. Mater. 31 (2019) e1805941.

[5] W. Kern, The evolution of silicon wafer cleaning technology, J. Electrochem. Soc. 137 (1990) 1887–1892.

[6] T. Yanase, T. Hasegawa, T. Nagahama, T. Shimada, Fabrication of piezoelectric polyurea films by alternating deposition, Jpn. J. Appl. Phys. 51 (2012) 041603.

[7] M. J. Frisch, G. W. Trucks, H. B. Schlegel, G. E. Scuseria, M. A. Robb, J. R. Cheeseman, G. Scalmani, V. Barone, G. A. Petersson, H. Nakatsuji, X. Li, M. Caricato, A. V. Marenich, J. Bloino, B. G. Janesko, R. Gomperts, B. Mennucci, H. P. Hratchian, J. V. Ortiz, A. F. Izmaylov, J. L. Sonnenberg, D. Williams-Young, F. Ding, F. Lipparini, F. Egidi, J. Goings, B. Peng, A. Petrone, T. Henderson, D. Ranasinghe, V. G. Zakrzewski, J. Gao, N. Rega, G. Zheng, W. Liang, M. Hada, M. Ehara, K. Toyota, R. Fukuda, J. Hasegawa, M. Ishida, T. Nakajima, Y. Honda, O. Kitao, H. Nakai, T. Vreven, K. Throssell, J. A. Montgomery, J. E. Peralta, F. Ogliaro, M. J. Bearpark, J. J. Heyd, E. N. Brothers, K. N. Kudin, V. N. Staroverov, T. A. Keith, R. Kobayashi, J. Normand, K. Raghavachari, A. P. Rendell, J. C. Burant, S. S. Iyengar, J. Tomasi, M. Cossi, J. M. Millam, M. Klene, C. Adamo, R. Cammi, J. W. Ochterski, R. L. Martin, K. Morokuma, O. Farkas, J. B. Foresman, and D. J. Fox, Gaussian, Inc. , Wallingford CT, 2016., Gaussian 16, Revision C.01, (2016).

[8] S. Grimme, J. Antony, S. Ehrlich, H. Krieg, A consistent and accurate ab initio parametrization of density functional dispersion correction (DFT-D) for the 94 elements H-Pu, J. Chem. Phys. 132 (2010) 154104.

[9] C. Lee, W. Yang, R.G. Parr, Development of the Colle-Salvetti correlation-energy formula into a functional of the electron density, Phys. Rev. B Condens. Matter 37 (1988) 785–789.

[10] A.D. Becke, Density-functional thermochemistry. III. The role of exact exchange, J. Chem. Phys. 98 (1993) 5648–5652.

[11] S.F. Boys, F. Bernardi, The calculation of small molecular interactions by the differences of separate total energies. Some procedures with reduced errors, Mol. Phys. 19 (1970) 553–566.

[12] S. Simon, M. Duran, J.J. Dannenberg, How does basis set superposition error change the potential surfaces for hydrogen-bonded dimers?, J. Chem. Phys. 105 (1996) 11024–11031.

[13] L. Jiang, P. Wang, M. Li, P. Zhang, J. Li, J. Liu, Y. Ma, H. Ren, G. Zhu, Construction of a stable crystalline polyimide porous organic framework for C_2H_2/C_2H_4 and CO_2/N_2 separation, Chem. Eur. J. 25 (2019) 9045–9051.

[14] Y.-P. Mo, X.-H. Liu, D. Wang, Concentration-directed polymorphic surface covalent organic frameworks: Rhombus, parallelogram, and kagome, ACS Nano 11 (2017) 11694–11700.

[15] X.-H. Liu, C.-Z. Guan, S.-Y. Ding, W. Wang, H.-J. Yan, D. Wang, L.-J. Wan, On-surface synthesis of single-layered two-dimensional covalent organic frameworks via solid–vapor interface reactions, J. Am. Chem. Soc. 135 (2013) 10470–10474.

[16] L.E. Stephans, A. Myles, R.R. Thomas, Kinetics of alkaline hydrolysis of a polyimide surface, Langmuir 16 (2000) 4706–4710.

[17] T. Zhu, B. Pei, T. Di, Y. Xia, T. Li, L. Li, Thirty-minute preparation of microporous polyimides with large surface areas for ammonia adsorption, Green Chem. 22 (2020) 7003–7009.

[18] S. Royuela, E. Martínez-Periñán, M.P. Arrieta, J.I. Martínez, M.M. Ramos, F. Zamora, E. Lorenzo, J.L. Segura, Oxygen reduction using a metal-free

naphthalene diimide-based covalent organic framework electrocatalyst, Chem. Commun. 56 (2020) 1267–1270.

[19] R.W. Baker, Membrane technology and applications, 4th ed., John Wiley & Sons, Nashville, TN, 2024.

[20] A.S. Kovvali, H. Chen, K.K. Sirkar, Dendrimer Membranes: A CO_2-selective molecular gate, J. Am. Chem. Soc. 122 (2000) 7594–7595.

[21] S.P. Nalawade, F. Picchioni, J.H. Marsman, L.P.B.M. Janssen, The FT-IR studies of the interactions of CO_2 and polymers having different chain groups, J. Supercrit. Fluids 36 (2006) 236–244.

[22] H. Fan, A. Mundstock, A. Feldhoff, A. Knebel, J. Gu, H. Meng, J. Caro, Covalent organic framework–covalent organic framework bilayer membranes for highly selective gas separation, J. Am. Chem. Soc. 140 (2018) 10094–10098.

[23] Z. Guo, H. Wu, Y. Chen, S. Zhu, H. Jiang, S. Song, Y. Ren, Y. Wang, X. Liang, G. He, Y. Li, Z. Jiang, Missing-linker defects in covalent organic framework membranes for efficient CO_2 separation, Angew. Chem. Int. Ed. Engl. 61 (2022) e202210466.

[24] J.E. Lopez-Cazares, K. Kim, J.Y.S. Lin, K. Jin, Gas permeation and separation characteristics of microporous TpHz COF membranes synthesized by substrate-assisted interfacial polymerization, Ind. Eng. Chem. Res. 63 (2024) 3684–3694.

[25] H.S. Sasmal, A. Halder, S. Kunjattu H, K. Dey, A. Nadol, T.G. Ajithkumar, P. Ravindra Bedadur, R. Banerjee, Covalent self-assembly in two dimensions: Connecting covalent organic framework nanospheres into crystalline and porous thin films, J. Am. Chem. Soc. 141 (2019) 20371–20379.

[26] Y. Ying, M. Tong, S. Ning, S.K. Ravi, S.B. Peh, S.C. Tan, S.J. Pennycook, D. Zhao, Ultrathin two-dimensional membranes assembled by ionic covalent organic nanosheets with reduced apertures for gas separation, J. Am. Chem. Soc. 142 (2020) 4472–4480.

[27] Y. Ying, S.B. Peh, H. Yang, Z. Yang, D. Zhao, Ultrathin covalent organic framework membranes via a multi-interfacial engineering strategy for gas separation, Adv. Mater. 34 (2022) e2104946.

[28] H. Zhang, T. Shao, Z. Cheng, J. Dong, Z. Wang, H. Jiang, X. Zhao, T. Xiaoteng

Liu, G. Zhu, X. Zou, Assembly-dissociation-reconstruction synthesis of covalent organic framework membranes with high continuity for efficient CO_2 separation, Angew. Chem. Int. Ed Engl. 45 (2024) e202411724.

Chapter 4 Solvent-Vapor-Assisted Crystallization of Covalent Organic Framework Films for CO_2/CH_4 Separation

4.1 Introduction

The purification of CO_2–CH_4 in natural gas or biogas has attracted much attention because CH_4 is a principal energy source. Membrane-based CO_2/CH_4 separation can purify natural gas with high energy efficiency and low cost [1]. COF films are promising candidates for CO_2/CH_4 separation membranes [2,3]. In the previous chapter, I demonstrated a new preparation method for COF films using alternating vapor deposition of precursors, followed by vacuum annealing. This method allowed us to obtain a free-standing COF film with precisely controlled stoichiometry and uniform thickness with a cm^2 area. However, it was found that there was room for improvement in the crystallinity of the synthesized COF film, which extracted the performance of ideal COF networks.

Herein, I focused on solvent vapor annealing to improve the crystallinity and CO_2/CH_4 separation performance of COF films synthesized via alternating vapor deposition. Solvent vapor annealing is an effective method for improving the

crystallinity of small molecules or polymer films, resulting in improved physical properties [4,5]. This method is also an effective approach for improving the crystallinity and framework alignment of the COF film [6–8].

4.2 Experiment

4.2.1 Materials

TAPB, 1,3,5-tris(4-formylphenyl)benzene (H-TFPB, >96.0%), and 1,4-dioxane (>99%) were purchased from Tokyo Kasei Inc. and used without further purification. Mesitylene (>97.0%) and acetic acid (AcOH, >99.7%) were purchased from FUJIFILM Wako Pure Chemical Co. and KANTO Chemical Co., Inc., respectively.

4.2.2 Preparation of COF film.

Alternating vapor deposition of the precursors to obtain the as-deposited film was performed using a homemade apparatus, as described in Chapter 3. Amine of TAPB and aldehyde of H-TFPB were used as precursors to prepare the as-deposited film (Fig. 4-1a). The thickness of a single layer of TAPB and H-TFPB were set to 18.1 and 3.1 nm, respectively. The precursors were deposited on Si/SO_2 and AAO by repeating 100 or 50 times. The detailed deposition conditions were optimized according to the HTA

and LTA-COF films described in Chapter 3.

The as-deposited film was annealed under solvent–vapor conditions (Fig. 4-1b). Mesitylene (0.5 mL), 1,4-dioxane (0.1 mL), and AcOH (0.1 mL) were mixed in a glass vial. The as-deposited film was placed in another glass tube to avoid contact between the solvent and the film. The vial was sealed and heated at 60 °C for 48 h. After annealing, the vial was cooled to room temperature. The annealed film was immersed in acetone to remove the residual solvents. The washed film was dried under ambient conditions to obtain the COF film.

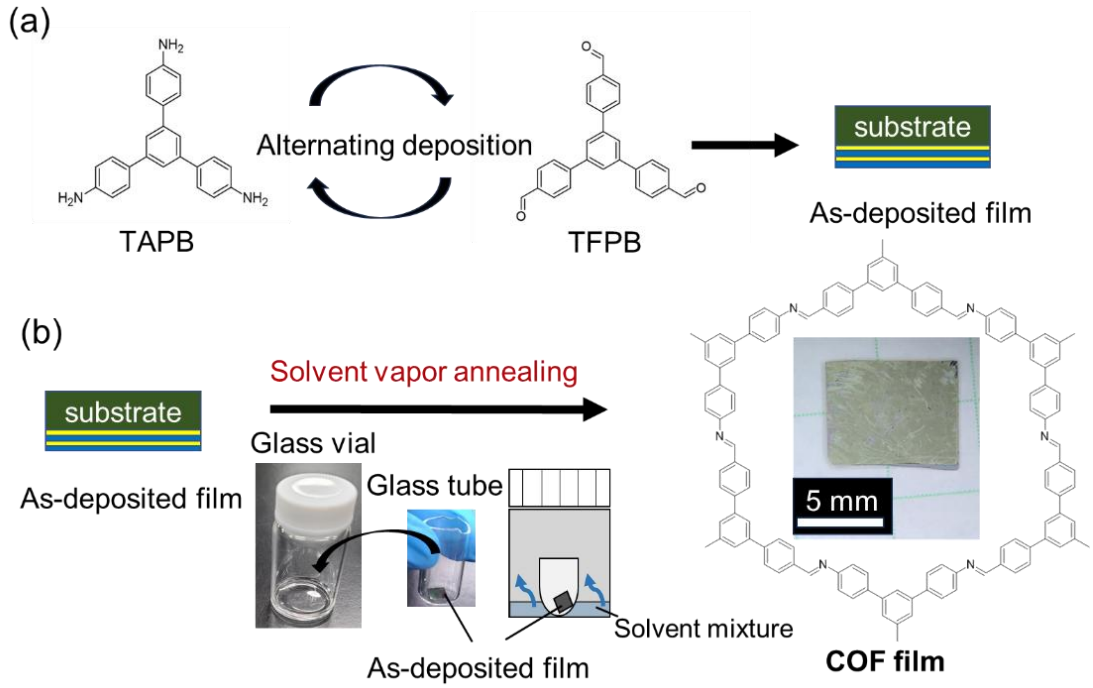

Fig. 4-1. Schematic illustration of the preparation procedure for the COF film. (a) Alternating deposition of TAPB and TFPB. (b) Solvent vapor annealing of as-deposited film. The inset shows the COF film prepared on a Si/SiO_2 substrate.

4.2.3 Synthesis of H-COF Powder

H-COF and its powder were synthesized via a conventional solvothermal method with slight modifications [9]. The TAPB (12.5 mg, 35.6 μmol) and H-TFPB (15.2 mg, 34.2 μmol) were dissolved in mesitylene (0.9 mL) and 1,4-dioxane (0.1 mL). AcOH (0.1 mL) was then added to the solution. The solution was then placed in an autoclave and heated in an oven at 120 °C for 12 h. After cooling to room temperature, the precipitate was washed with acetone to remove residual solvents and dried under ambient conditions to obtain H-COF powder.

4.2.4 Calculation of optimized COF structure

The optimized COF structure was calculated by DFT using the Vienna ab initio calculation package (VASP) [10]. The initial structure of the COF was assumed to be an ideal hexagonal arrangement of the precursor molecules. The calculation was conducted using the generalized gradient approximation (GGA) of the Perdew–Burke–Ernzerhof (PBE) functional [11]. The dispersion interaction was corrected using Grimme's D3 method [12]. The system was optimized until the energy difference was below 1.0×10^{-5} eV. A 4×4×4 k-mesh grid was used for electronic state calculation.

4.2.5 Characterization of COF

FTIR and STEM measurements were conducted using the methods described in section 3.2.2, Chapter 3. Out-of-plane X-ray diffraction (XRD) measurements were performed using a Rigaku MiniFlex 600. Gas permeation measurements were conducted using the method described in Chapters 1 and 3. Gas permeation measurements were performed using the same procedure described in Chapters 1 and 3. Pure CO_2 or CH_4 were used for the measurement.

4.2.6 Estimation of defects in as-deposited film

It is proposed that gas permeability through porous materials can be expressed by Eq. 1.2. From Eq. 1.2, the CO_2/CH_4 selectivity was calculated using Eq. (4.1).

$$ {}^{CO_2}/_{CH_4}\ \text{selectivity} = \frac{P_{CO2}}{P_{CH4}} = \frac{\sqrt{\frac{8RT}{\pi M_{CO2}}} + \frac{r^2}{8\mu_{CO2}} p_{av}}{\sqrt{\frac{8RT}{\pi M_{CH4}}} + \frac{r^2}{8\mu_{CH4}} p_{av}} \tag{4.1} $$

where P_{CO2} and P_{CH4} are the permeabilities for CO_2 and CH_4, respectively. The CO_2/CH_4 selectivity depends only on *r*. The parameters used in the calculations are listed in Table 4-1.

Table 4-1. Physical parameters of CO_2 and CH_4 for gas permeation through the as-deposited film.

	CO_2	CH_4
R / J mol^{-1} K^{-1}	8.31	
T / ^{o}C	25	
q	2.5	
P_{av} / Pa	10^4	
μ / Pa s^{-1}	1.47×10^{-5}	1.08×10^{-5}
M / g mol^{-1}	44	16

4.3 Results and Discussion

4.3.1 Characterization of COF Structure

The imine formation between the amine and aldehyde moieties was evaluated using FTIR and Raman spectroscopy. For the FTIR spectra of COF films (Fig. 4-2a), the characteristic peak of imine moiety denoted as "a" symbol was observed (1593 cm^{-1} from –C=N), while the intensity of peaks from the precursor of TAPB and TFPB, which are denoted as a "b" symbol, relatively decreased (3354 cm^{-1} from –NH_2 of TAPB and 1680 cm^{-1} from –CHO of TFPB). From the Raman spectra, the strong peaks denoted as "a" symbol were observed at 1592 and 1562 cm^{-1}, corresponding to aromatic C=C and imine moiety, respectively (Fig. 4-2b)[13]. In addition, the peaks denoted as "b" symbol from precursors (amine of TAPB at 1610 and aldehyde of H-TFPB at 1626 cm^{-1}) were not

observed in the peaks from H-COF powder and films. These results indicate that the functional groups in TAPB of the amine and TFPB of the aldehyde were successfully polymerized to form an imine bond in the COF film [9].

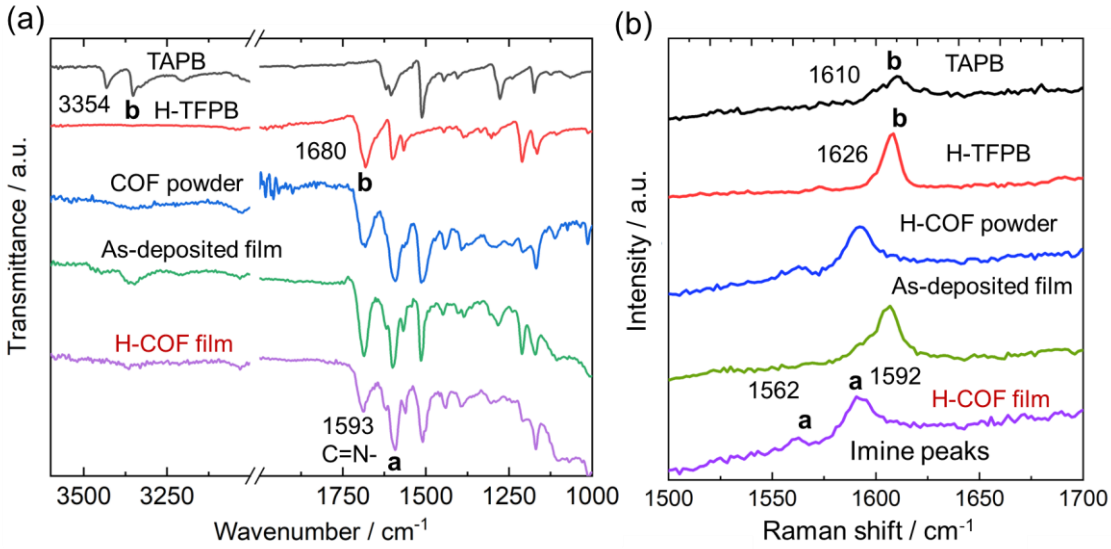

Fig. 4-2. (a) FTIR and (b) Raman spectra of the COF film and its precursors.

Out-of-plane XRD confirmed the crystallinity of the COF film prepared on the Si/SiO_2 substrate. The as-deposited film did not exhibit the apparent crystallinity of the COF, whereas after annealing in vapor containing mesitylene, 1,4-dioxane, and AcOH (volumetric ratio of 9:1:1), diffraction peaks corresponding to the COF skeleton were observed, which were the 100 and 110 reflections at 2θ angles of 4.0° and 7.0°, respectively (Fig. 4-3a; the optimized COF structure is shown in Fig. 4-3c). In addition, the interlayer distance of the COF film was confirmed by an enlarged XRD profile (Fig. 4-3b), exhibiting a broad diffraction peak from (001) at a 2θ of ca. 25.6°. I could not

find XRD features showing crystallinity related to the COF when the as-deposited film was annealed in a vacuum at 120 °C for 12 h. The as-deposited film was annealed in a mesitylene/1,4-dioxane mixture (volumetric ratio of 9:1) or AcOH vapor at 60 °C for 48 h and did not exhibit apparent crystallinity of the COF. Thus, it is essential to choose an appropriate solvent vapor mixture to facilitate the crystallization of COF films because the vapor pressure of each solvent can affect the formation of dynamic imine bonds.

The effect of annealing conditions on the crystallinity of the H-COF films was investigated. When the annealing temperature was below 60 °C or above 150 °C, the diffraction intensity from 100 facets decreased (Fig. 4-3d). The diffraction intensity from 100 facets was greatest at an annealing temperature of 60 °C because the relatively low annealing temperature allowed a dynamic imine bond reaction to promote gentle crystallization. In addition, when the annealing time was extended from 12 to 48 h, the peak intensities of the impurities decreased (Fig. 4-3e). When the precursor ratio of H-TFPB or TAPB was in excess (weight ratio of TAPB: H-TFPB = 1:17 or 1:2, respectively), the annealed film exhibited either poor or no crystallinity (Fig. 4-3f). These results indicate that an appropriate annealing temperature, time, precursor ratio, and solvent composition are necessary to synthesize crystalline COF films by alternating deposition polymerization followed by solvent vapor annealing.

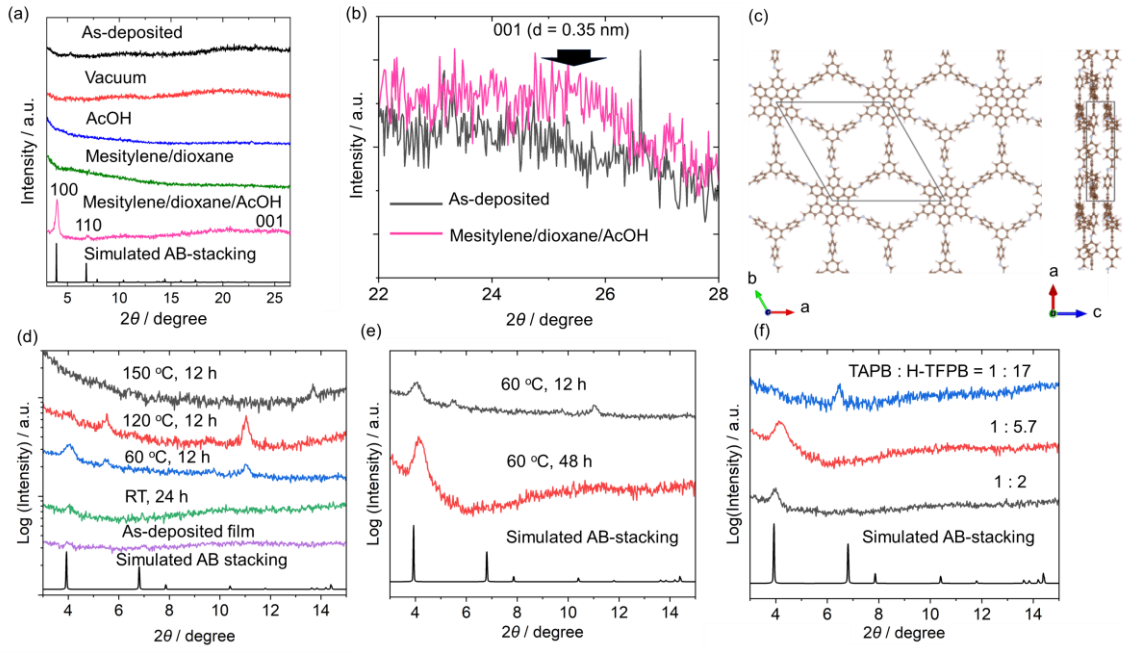

Fig. 4-3. Out-of-plane XRD of COF film with (a) different annealing conditions and (b) enlarged view. (c) The calculated COF structure was visualized from the c and b axes using VESTA software [14]. (d) Annealing temperature, (e) annealing time, and (f) precursor ratio dependence of out-of-plane XRD for the H-COF films.

STEM observations were performed to examine the nanostructures of the COF films. The STEM image of COF film scraped from the Si substrate showed a spherical structure with piled layers like “onions” (Fig. 4-4a). The high-magnification image confirmed that the COF layers had many defects, such as shifting or branching (Fig. 4-4b in yellow lines). The interlayer distance of ca. 0.35 nm agrees well with the XRD diffraction from (001) at a 2θ of ca. 25.6° (*d*-spacing = 0.346 nm). This result indicates that the “onions” are not formed by rolling layers, such as in the spiral growth mode, but by layer-by-layer crystallization. In other words, the alignment of the layers can be

induced by the interactions between the layers. This suggests a promising strategy for preparing fully ordered crystalline COF films by preparing the first flat-lying layer of COF on the substrate. My vacuum deposition method followed by solvent annealing is suitable for this strategy.

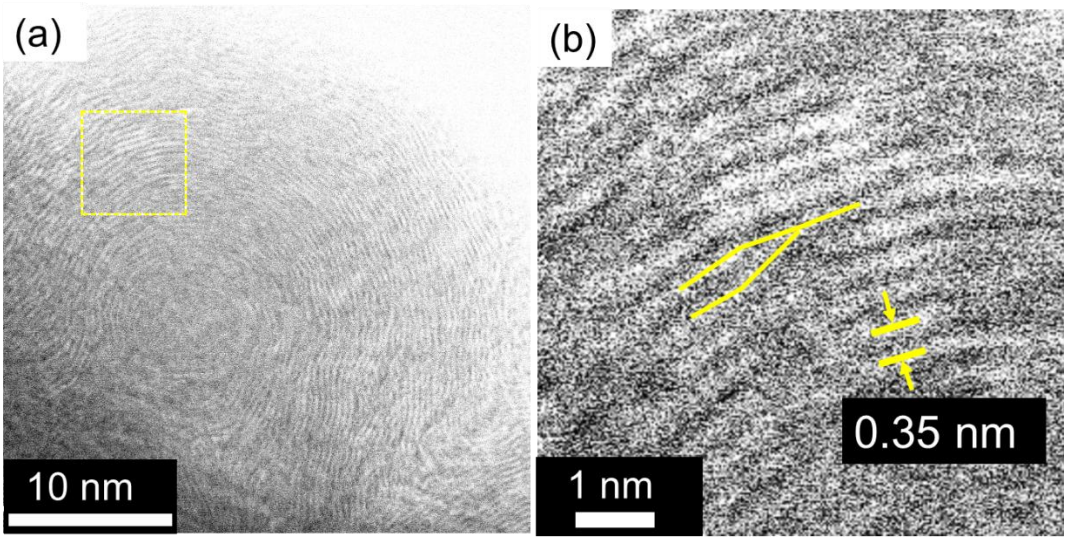

Fig. 4-4. STEM image of the COF film. (a) at low magnification and (b) enlarged view of the yellow square area in (a).

4.3.2 Evaluation of gas permeation performances of the COF film

The CO_2/CH_4 ideal selectivity of the COF film (2.8) was 3.6 times greater than that of the as-deposited film (0.78) at a transmembrane pressure of 10^4 Pa (Fig. 4-5a). The gas selectivity according to Knudsen diffusion (gas permeation mechanism of a porous membrane with diameters of several to 50 nm) is inversely proportional to the square root of molecular weight, i.e., $\sqrt{(16/44)} = 0.6$ for CO_2/CH_4 separation [15]. The ideal selectivity of the as-deposited film (0.78) was slightly greater than that of Knudsen diffusion separation (0.60), suggesting that many defects exist in the as-deposited film.

The size and density of the defects in the as-deposited films were numerically analyzed using Eq. (1.2) and Eq. (4.1), using numerical calculations. Because the Knudsen flow is dominant at a small *r*, the selectivity approaches the Knudsen separation (0.60) at a sufficiently small *r*. However, *r* approached the ratio of the viscosity of the gas (0.73) when *r* was sufficiently large. The experimental CO_2/CH_4 selectivity was 0.78 at a transmembrane pressure of 10^4 Pa, close to the viscosity ratio 0.73. This result suggests that large defective pores with $r > 1$ μm (99% exceeding the viscosity ratio) exist in the as-deposited film. The value of ε is estimated as 1.77×10^{-5} if the CO_2 permeability is equal to the experimental value of 1200 Barrer = 4.02×10^{-13} mol m^{-1} s^{-1} Pa^{-1} (substitute into Eq. 1.2). Therefore, the density of defects per film area (1.0×10^{-5} m^2) was estimated

as 5.62×10^{6} m^{-2}.

This result indicates that solvent vapor annealing promoted the polymerization of the COF and reduced the defects in the film, improving the CO_2/CH_4 separation performance to 2.8. However, the greatest CO_2/CH_4 separation factor for neat COF films is ~90, using a COF with a 0.94 nm pore radius [3]. The COF in the present work had an ideal pore size of 2.2 nm, contributing to the lower separation performance. One way to improve this is to use a halogen modification of the inner wall [2] to reduce the pore diameter.

The CO_2 permeability of the COF film (16 Barrer) was ca. 74 times lower than that of the as-deposited film (1200 Barrer) at a transmembrane pressure of 10^4 Pa, indicating a decrease in defects by growing the COF crystals (Fig. 4-5b). The CO_2 and CH_4 permeabilities of AAO were ca. 2000 times greater than those of COF; thus, the resistance of gas permeation through AAO can be ignored. The CO_2 permeability of the vapor-annealed COF film was 5.9 times greater than that of the vacuum-annealed COF film (2.7 Barrer), suggesting that the orientation of pores contributes to the improvement of gas permeability. Transmembrane pressure did not significantly affect the CO_2/CH_4 selectivity of the COF film (range of 2.2–2.7). This result indicates that the COF film has durability for pressure differences, at least under vacuum and atmospheric pressure.

This COF film can be applied in separation methods, such as vacuum swing or continuous pumping, which require high tolerability to pressure.

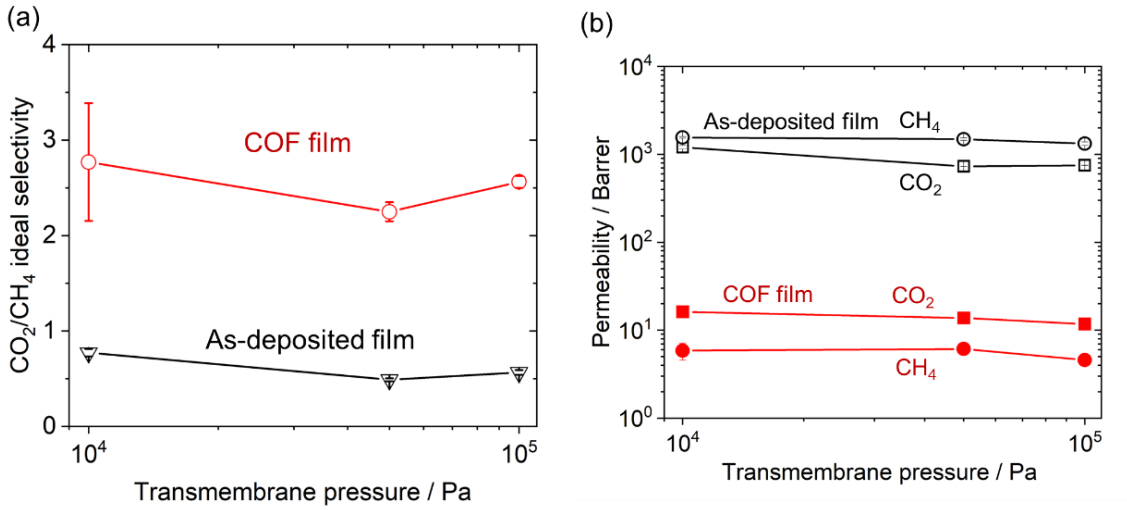

Fig. 4-5. (a) Transmembrane pressure dependence of the CO_2/CH_4 ideal selectivity of COF and as-deposited film. (b) CO_2 and CH_4 permeabilities of as-deposited film and COF film. The permeation measurements at each transmembrane pressure were repeated multiple times, and the error bars indicate the standard deviation of the experiments.

The optimized gas absorption sites and gas absorption energy (ΔE_{int}) are shown in Fig. 4-6. ΔE_{int} of CO_2 (-14.5 kJ mol^{-1}) was 1.7 times greater than that of CH_4 (-8.41 kJ mol^{-1}). The absorption sites for COF and CO_2 were the N atom of COF and the C atom of CO_2, and the H atom of COF and the O atom of CO_2 with distances of 3.01 and 2.70 Å, respectively. The adsorption sites for COF and CH_4 were the N of COF and the H of CH_4 with a distance of 2.61 Å. These results indicate that the affinity of COF for CO_2 is greater than that of CH_4 because of not only the electrostatic interaction between the N of COF and the C of CO_2 [16] but also the hydrogen bond between the H of COF

and the O of CO_2 contributes to the absorption [17].

The activation energy difference between the occupied states of CO_2 and CH_4 was $\Delta E = 6.09$ kJ mol^{-1}. The ratio of the Boltzmann distribution between the occupied states to the COF at room temperature is $\exp(\Delta E/RT)=11.7$, where R is the gas constant and T is the absolute temperature. When the gas permeation speed was governed by the adsorption of the pore walls in the COF, the permeation ratio was close to this ratio. The CO_2/CH_4 selectivity of the prepared COF film (2.8) was lower than that of this ratio, which can be explained by two possibilities. First, the pore size is too large for CO_2 and CH_4, and direct channeling is prominent. Another possibility is defects in the COF films; for example, less crystalline tissues between "onions" in the STEM images can act as gas leak pathways. Since I have established a promising strategy for making COF films with a high order, I will be able to examine the pore size effects more precisely in the future.

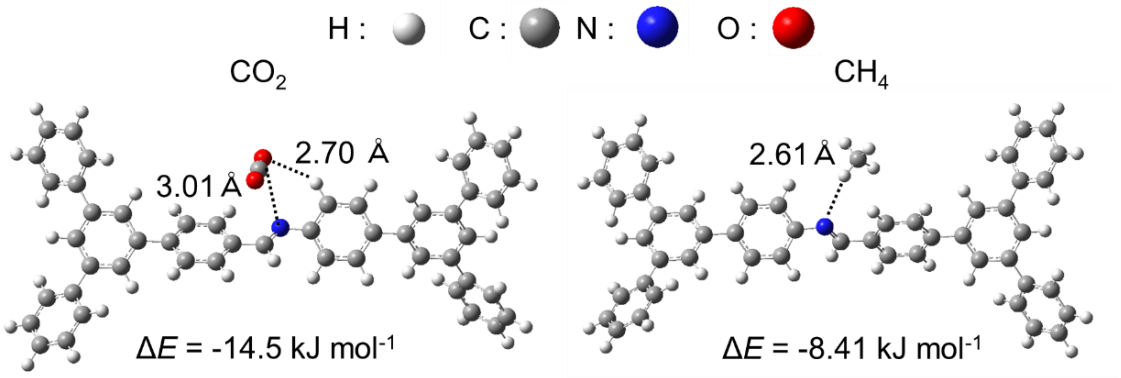

Fig. 4-6. Optimized absorption site of the COF moiety with CO_2 and CH_4

4.3.3 Comparison with literature membranes for CO_2/CH_4 separation

I compared the literature membrane and the prepared COF films for CO_2/CH_4 separation. Table 4-2 shows the CO_2/CH_4 separation performance of the COF membranes. DhaTGAsp-X and NCOFM-0 exhibited high CO_2/CH_4 separation performance, but it should be noted that these membranes should be used under humid conditions. Figure 4-7 shows Robeson's plot of COF films for CO_2/CH_4 separation under dry conditions. The H-COF-film (red symbol) exhibited similar CO_2 permeability and CO_2/CH_4 selectivity compared to previously reported COF films (black symbols). ACOF-1 has been reported to have a particularly high CO_2/CH_4 separation performance. As the pore size of ACOF-1 is less than 1 nm, the CO_2/CH_4 separation performance can be improved by reducing the pore size of the COF film. Unfortunately, the CO_2/CH_4 separation performance of the prepared COF film did not exceed the limitations of polymeric

membranes. It is expected that the modulation of the backbone in COF films is important for improving the CO_2/CH_4 separation performance.

Table 4-2. Comparison with literature COF membranes for CO_2/CH_4 separation

Name	Thickness /μm	CO_2 permeability / Barrer	CO_2/CH_4 selectivity	Ref.
ACOF-1	8	56.6	97.1	[3]
DhaTGAsp-X	0.23	33.0	79	[18]
COF-LZU1–ACOF-1	1	27.4	3.9	[19]
NCOFM-0	0.20	36.8	17	[20]
TpHz COF	0.29	20.6	0.60	[21]
TpEBr@TpPa –SO_3Na iCON	0.041	4.65	2.8	[22]
$TpTG_{Cl}$@TpPa–SO_3H	0.16	12.9	1.7	[23]
Vertically aligned COF-LZU1	2	230	0.93	[24]
LA-α-CD–TpPa-1	1.5	127	1.1	[25]
Solvent vapor annealed COF	2.1	16.0	2.8	**This work**

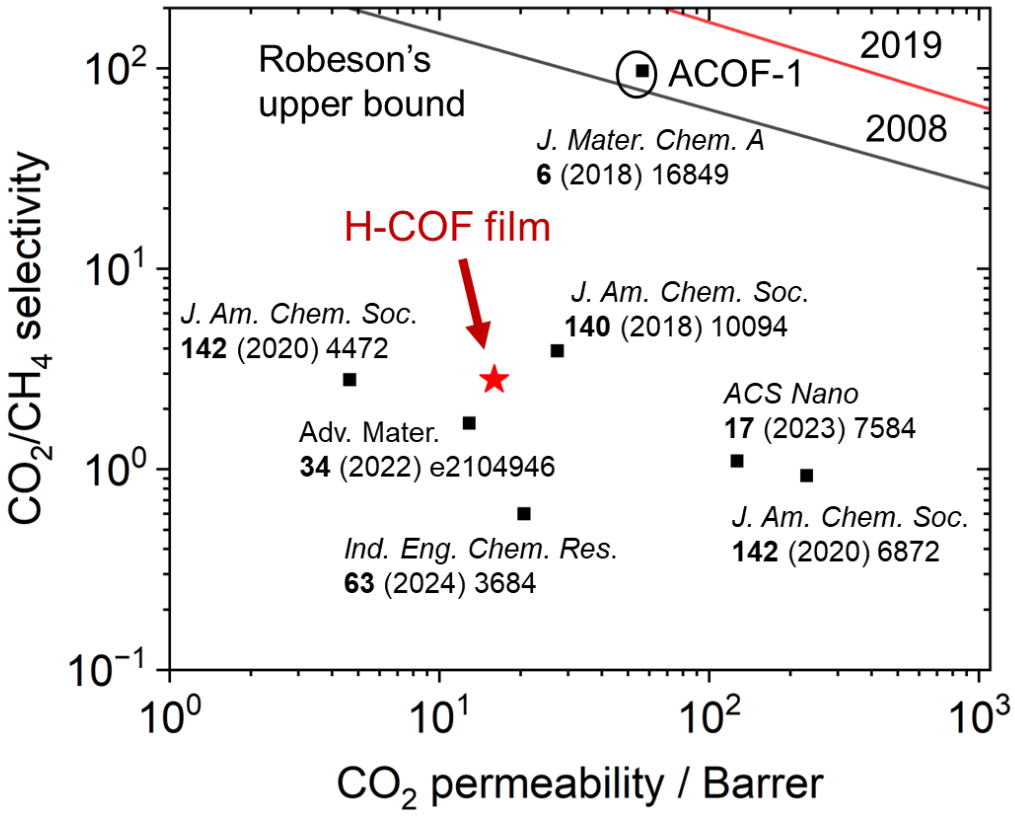

Fig. 4-7 Robeson's plot for CO_2/CH_4 separation under the dry condition. The red and black symbols represent the COF film prepared in this work and previous works, respectively. The red and black line represent the Robeson's upper bound in 2019 and 2008, respectively.

4.4 Conclusion

Crystalline COF films were synthesized using alternating vapor deposition followed by solvent vapor annealing, and their CO_2/CH_4 separation performances were evaluated. Structural analysis confirmed the formation of imine bonds and the successful synthesis of COF films with a well-defined organization. Notably, the vapor composition played a crucial role in improving the crystallinity and formation of layer stacking in the COF film. This result suggests that an ideal planar-oriented COF film can be synthesized by preparing a defect-free first layer on a substrate. The CO_2/CH_4 selectivity of the vapor-annealed COF film (2.8) was greater than that of the as-deposited film (0.78), indicating that dense and highly crystalline COF films improve the CO_2/CH_4 selectivity. This study provides insights into how to prepare strictly oriented COF films and improve their gas separation performance.

References

[1] Y. Zhang, J. Sunarso, S. Liu, R. Wang, Current status and development of membranes for CO_2/CH_4 separation: A review, Int. J. Greenhouse Gas Control 12 (2013) 84–107.

[2] T. Yan, Y. Lan, M. Tong, C. Zhong, Screening and design of covalent organic framework membranes for CO_2/CH_4 separation, ACS Sustainable Chem. Eng. 7 (2019) 1220–1227.

[3] H. Fan, A. Mundstock, J. Gu, H. Meng, J. Caro, An azine-linked covalent organic framework ACOF-1 membrane for highly selective CO_2/CH_4 separation, J. Mater. Chem. A 6 (2018) 16849–16853.

[4] C. Liu, T. Minari, X. Lu, A. Kumatani, K. Takimiya, K. Tsukagoshi, Solution-processable organic single crystals with bandlike transport in field-effect transistors, Adv. Mater. 23 (2011) 523–526.

[5] Y. Liu, Q. Shi, H. Dong, J. Tan, W. Hu, X. Zhan, Solvent-vapor induced self-assembly of a conjugated polymer: A correlation between solvent nature and transistor performance, Org. Electron. 13 (2012) 2372–2378.

[6] M. Liu, Y. Liu, J. Dong, Y. Bai, W. Gao, S. Shang, X. Wang, J. Kuang, C. Du, Y. Zou, J. Chen, Y. Liu, Two-dimensional covalent organic framework films prepared on various substrates through vapor induced conversion, Nat. Commun. 13 (2022) 1–9.

[7] N.A. Khan, R. Zhang, X. Wang, L. Cao, C.S. Azad, C. Fan, J. Yuan, M. Long, H. Wu, M.A. Olson, Z. Jiang, Assembling covalent organic framework membranes via phase switching for ultrafast molecular transport, Nat. Commun. 13 (2022) 3169.

[8] C. Yin, M. Liu, Z. Zhang, M. Wei, X. Shi, Y. Zhang, J. Wang, Y. Wang, Perpendicular alignment of covalent organic framework (COF) pore channels by solvent vapor annealing, J. Am. Chem. Soc. 145 (2023) 11431–11439.

[9] G. Jiang, W. Zou, Z. Ou, L. Zhang, W. Zhang, X. Wang, H. Song, Z. Cui, Z. Liang, L. Du, Tuning the interlayer interactions of 2D covalent organic frameworks enables an ultrastable platform for anhydrous proton transport, Angew. Chem. Int. Ed Engl. 61 (2022) e202208086.

[10] G. Kresse, J. Hafner, Ab initio molecular dynamics for liquid metals, Phys. Rev. B 47 (1993) 558–561.

[11] J.P. Perdew, K. Burke, M. Ernzerhof, Generalized gradient approximation made simple, Phys. Rev. Lett. 77 (1996) 3865–3868.

[12] S. Grimme, J. Antony, S. Ehrlich, H. Krieg, A consistent and accurate ab initio parametrization of density functional dispersion correction (DFT-D) for the 94 elements H-Pu, J. Chem. Phys. 132 (2010) 154104.

[13] W. Dai, F. Shao, J. Szczerbiński, R. McCaffrey, R. Zenobi, Y. Jin, A.D. Schlüter, W. Zhang, Synthesis of a two-dimensional covalent organic monolayer through dynamic imine chemistry at the air/water interface, Angew. Chem. Int. Ed Engl. 55 (2016) 213–217.

[14] K. Momma, F. Izumi, VESTA: a three-dimensional visualization system for electronic and structural analysis, J. Appl. Crystallogr. 41 (2008) 653–658.

[15] D. De Meis, Gas transport through porous membranes, ENEA (2017) 1–20.

[16] K. Sumida, D.L. Rogow, J.A. Mason, T.M. McDonald, E.D. Bloch, Z.R. Herm, T.-H. Bae, J.R. Long, Carbon dioxide capture in metal-organic frameworks, Chem. Rev. 112 (2012) 724–781.

[17] H.M. Lee, I.S. Youn, M. Saleh, J.W. Lee, K.S. Kim, Interactions of CO_2 with various functional molecules, Phys. Chem. Chem. Phys. 17 (2015) 10925–10933.

[18] Z. Guo, H. Jiang, H. Wu, L. Zhang, S. Song, Y. Chen, C. Zheng, Y. Ren, R. Zhao, Y. Li, Y. Yin, M.D. Guiver, Z. Jiang, Oil-water-oil triphase synthesis of ionic covalent organic framework nanosheets, Angew. Chem. Int. Ed Engl. 60 (2021) 27078–27085.

[19] H. Fan, A. Mundstock, A. Feldhoff, A. Knebel, J. Gu, H. Meng, J. Caro, Covalent organic framework–covalent organic framework bilayer membranes for highly selective gas separation, J. Am. Chem. Soc. 140 (2018) 10094–10098.

[20] Z. Guo, H. Wu, Y. Chen, S. Zhu, H. Jiang, S. Song, Y. Ren, Y. Wang, X. Liang, G. He, Y. Li, Z. Jiang, Missing-linker defects in covalent organic framework membranes for efficient CO_2 separation, Angew. Chem. Int. Ed Engl. 61 (2022) e202210466.

[21] J.E. Lopez-Cazares, K. Kim, J.Y.S. Lin, K. Jin, Gas permeation and separation characteristics of microporous TpHz COF membranes synthesized by substrate-assisted interfacial polymerization, Ind. Eng. Chem. Res. 63 (2024) 3684–3694.

[22] Y. Ying, M. Tong, S. Ning, S.K. Ravi, S.B. Peh, S.C. Tan, S.J. Pennycook, D. Zhao,

Ultrathin two-dimensional membranes assembled by ionic covalent organic nanosheets with reduced apertures for gas separation, J. Am. Chem. Soc. 142 (2020) 4472–4480.

[23] Y. Ying, S.B. Peh, H. Yang, Z. Yang, D. Zhao, Ultrathin covalent organic framework membranes via a multi-interfacial engineering strategy for gas separation, Adv. Mater. 34 (2022) e2104946.

[24] H. Fan, M. Peng, I. Strauss, A. Mundstock, H. Meng, J. Caro, High-flux vertically aligned 2D covalent organic framework membrane with enhanced hydrogen separation, J. Am. Chem. Soc. 142 (2020) 6872–6877.

[25] H. Fan, H. Wang, M. Peng, H. Meng, A. Mundstock, A. Knebel, J. Caro, Pore-in-pore engineering in a covalent organic framework membrane for gas separation, ACS Nano 17 (2023) 7584–7594.

Chapter 5 Fluorinated Covalent Organic Framework Films for Efficient VOC/N_2 Separation

5.1 Introduction

The recovery of VOC is important because they are hazardous to human health and the environment. Membrane separation has been investigated for VOC recovery. This method is advantageous for small-scale VOC recovery, such as equipment for household use, because the apparatus can be easily downsized. Conventional polymer materials, such as polydimethylsiloxane (PDMS) [1,2] and polyimide [3], have been used as VOC separation membranes. Recently, new materials for VOC membrane separation have been reported to enhance the permeation and separation properties of VOC [4–7]. COF are promising candidates for molecular separation membranes such as liquid-phase filtration[8] and pervaporation[9–13]. However, the vapor permeation properties of COF membranes have not been sufficiently explored. Although the VOC–N_2 separation properties of MMM have been reported[14,15], to the best of my knowledge, that of neat COF films has not been explored.

In this chapter, the VOC/N_2 separation performance of COF films with various functional groups was evaluated. I will reveal the effect of functionalization of COF

films on VOC permeation properties and provide guidance for designing high-performance COF films for VOC recovery. COF films were prepared via alternating vapor deposition of the precursors, followed by solvent vapor annealing. The amine of TAPB and two types of substituted aldehydes, H-TFPB or 3,3"-difluoro-5'-(3-fluoro-4-formylphenyl)-[1,1':3',1"-terphenyl]-4,4"-dicarbaldehyde (F-TFPB), were deposited on various substrates by repetition of 10–100 times to obtain the as-deposited films. The as-deposited film was annealed under solvent vapor conditions to obtain two types of COF films: H-COF and F-COF (Fig. 5-1). The structural analysis of the films was performed using Raman spectroscopy, XRD, and electron microscopy. The separation performances between VOC of dichloromethane (DCM), methyl ethyl ketone (MEK), and ethyl acetate (EtOAc) and N_2 were evaluated using gas permeation tests and theoretical calculations.

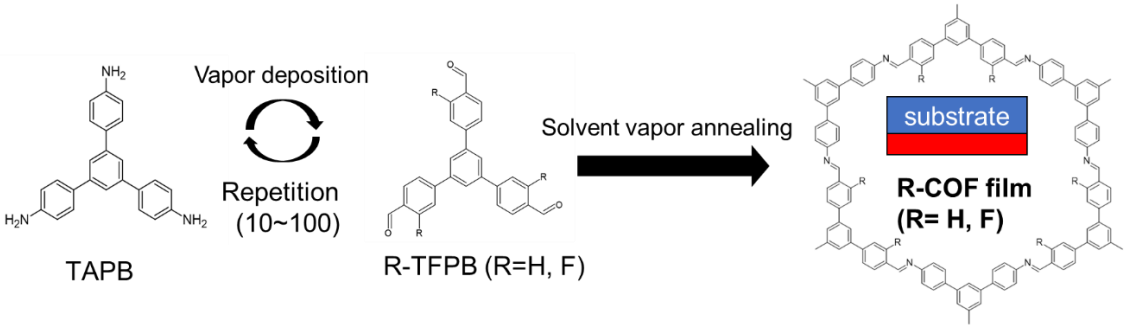

Fig. 5-1. Schematic illustration of preparation procedure for H- and F-COF films.

5.2 Experiment

5.2.1 Materials

TAPB, H-TFPB, 1,3,5-tribromobenzene (>98%), 3-fluoro-4-formylphenylboronic acid (containing varying amounts of anhydride), tetrakis (triphenylphosphine)palladium(0) ($Pd(PPh_3)_4$, >97%), potassium carbonate (K_2CO_3, >99%), and 1,4-dioxane (>99%) were purchased from Tokyo Kasei, Inc. All the reagents were used without further purification.

5.2.2 Synthesis of F-TFPB

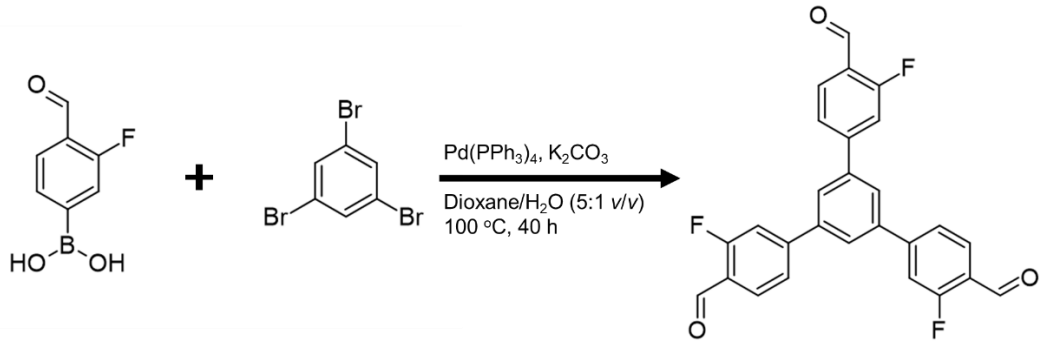

F-TFPB was synthesized using a previously reported method with slight modifications [16]. 1,4-dioxane (1.5 mL) and water (0.3 mL) were mixed in a Teflon beaker in a stainless-steel autoclave and degassed by N_2 bubbling for 30 min. Then, 1,3,5-tribromobenzene (61.2 mg, 0.194 mmol), 3-fluoro-4-formylphenylboronic acid (165 mg, 0.983 mmol), and K_2CO_3 (175 mg, 1.29 mmol) were added to the solvent mixture. The beaker was then transferred to an Ar glove box, and $Pd(PPh_3)_4$ (34.6 mg, 0.0299 mmol)

was added to the solution. The beaker was then sealed and heated at 100 °C for 40 h. Subsequently, the reaction mixture was cooled to room temperature, and the precipitate was filtered and washed with water and ethyl acetate to yield the desired product (38.2 mg, 44%). ^{1}H-NMR (400 MHz, DMSO-d6, δ) 10.26 (s, 3H) 8.27 (s, 3H), 8.16 (d, *J* 12.1 Hz, 3H), 8.01 (d, J 7.6 Hz, 3H), 7.96 (t, *J* 8.0, 8.3 Hz, 3H), ^{19}F-NMR (400 MHz, DMSO-d6, δ) -120.2 (s, 3F)

5.2.3 Synthesis of F-COF powder

The F-COF powder was synthesized using a procedure similar to that used for the H-COF powder. TAPB (12.5 mg, 35.6 μmol) and F-TFPB (15.2 mg, 34.2 μmol) were dissolved in mesitylene (0.9 mL) and 1,4-dioxane (0.1 mL). Acetic acid (AcOH, 0.1 mL) was then added to the solution. The solution was then placed in an autoclave and heated in an oven at 120 °C for 12 h. After cooling to room temperature, the precipitate was washed with acetone to remove residual solvents and dried under ambient conditions to obtain the F-COF powder.

5.2.4 Preparation of COF film

H-COF and F-COF films were prepared by alternating vapor deposition followed by

solvent vapor annealing. The H-COF film was prepared under the conditions described in Chapter 4. The preparation conditions of the F-COF films were optimized using the procedure described in Chapters 3 and 4. The single-layer thicknesses of the TAPB and F-TFPB were 18 and 1.7 nm, respectively.

5.2.5 Structural analysis of the COF films

AFM, STEM, and laser microscopy were performed using the same procedures described in section 3.2.2, Chapter 3. Field emission scanning electron microscopy (FE-SEM) was performed using a JEOL JSM7200F at an acceleration voltage of 15 kV. Fourier transform infrared spectroscopy (FTIR) was performed using a JASCO FT/IR-4700 with 4 cm^{-1} resolution using an attenuated total reflection method for both COF films and precursor powders. Raman spectroscopy was performed by a Renishaw Invia with a 532 nm laser excitation. Out-of-plane and powder X-ray diffraction (XRD) measurements were performed using a Rigaku MiniFlex600 with a 2θ scan rate of 0.1°/min. In-plane XRD measurements were performed using a Rigaku Smart Lab. The crystal domain size was estimated using the Scherrer equation, assuming that the crystal was cubic and that the diffraction vectors were oriented perpendicular to the plane.

5.2.6 Optimized structure and stacking energy calculation

The optimized structure and stacking energy of the COF film were calculated by DFT using the Vienna ab initio calculation package (VASP)[17]. The initial structures of H-COF and F-COF were assumed to be ideal hexagonal arrangements of the precursor molecules. The AA and AB stacking systems were calculated using the interlayer distance of ca. 3.3 Å, whereas the single-layer system was calculated by inserting a vacuum layer of 10 Å along the c-axis between the layers. The calculation was conducted using the generalized gradient approximation (GGA) of the Perdew–Burke–Ernzerhof (PBE) functional[18]. The dispersion interaction was corrected using Grimme's D3 method[19]. The system was optimized until the energy difference was below 1.0×10^{-5} eV. A 4×4×4 k-mesh grid was used for electrical calculations. The optimized structures and calculated XRD patterns were visualized using VESTA[20]. The interaction energy of interlayer stacking ($E_{\mathrm{intaction}}$) was estimated by the following Eq. 5-1,

$$E_{\mathrm{intaction}} = E_{\mathrm{stacking}} - E_{\mathrm{single\ layer}} \tag{5.1}$$

where E_{stacking} and $E_{\mathrm{single\ layer}}$ are the total energies of the stacked and single-layer systems, respectively.

5.2.7 Orientaion analysis of COF films

A quantitative analysis of the crystal orientation of the COF films on the substrate was performed by fitting the simulation patterns to the measured out-of-plane XRD. The model structures of H-COF and F-COF with different stacking configurations (AA- and AB-stacking) were obtained using the same procedure described in section 5.2.6. The XRD Intensity of I_{hkl} for each model was calculated by the following Eq. (5.2).

$$I_{hkl} = M_{hkl} \times LP_{\theta} \times T_{hkl} \times |F_{hkl}|^2 \tag{5.2}$$

where M_{hkl} is the multiplicity factor, LP_{θ} is the Lorentz polarization factor, T_{hkl} is the preferred orientation factor, and F_{hkl} is the structural factor. The atomic scattering factor was used for the library values[21]. The Debye–Waller factor B was set to 2.0 Å^2.

LP_{θ} is given by Eq. (5.3) with diffraction angle θ:

$$LP_{\theta} = \frac{1 + \cos^2 2\theta}{\cos\theta \sin 2\theta} \tag{5.3}$$

T_{hkl} was expressed using the March–Dollase function (Eq. (5.4)).

$$T_{hkl} = \left({r_M}^2 \cos^2 \psi_o + \frac{\sin^2 \psi_o}{r_M} \right)^{-1.5} \tag{5.4}$$

where ψ_o is the crystal orientation angle and r_M is the March–Dollase parameter. The orientation angles are represented by Euler angles (ψ, Θ, Φ). The initial crystal orientation axis of (ψ, Θ, Φ) = (0,0,0) was set such that the 001-direction coincided with the normal direction of the substrate. The range of r_M was $0 < r_M \leq 1$. The $r_M = 1$ means unoriented,

whereases $r_M \ll 1$ means strong orientation at its Euler angle.

I_{hkl} was calculated from a model of a structure with arbitrary (ψ, Θ, Φ) and r_M AA- and AB-stacking structures in the ratio R_{AA} versus R_{AB} =1-R_{AA}, respectively. The experimental peak intensities were extracted from background-subtracted XRD patterns. The optimal orientation parameters (ψ, Θ, Φ), r_M, and R_A were obtained by minimizing the mean square error (MSE) between the normalized experimental XRD peak intensity and simulated intensity. The analysis program was developed using Python version 3.7.1. Algorithms for searching for the minimum value use the differential-evolution method, which can search for the global minimum of a system.

5.2.8 STEM image simulations

STEM image simulations were performed using the ReciPro software [22]. The apparatus constants were the same as those used for the measurements (Table 5-1). The sample thickness was 20 nm. The chromatic aberration and defocus were set at 0.

Table 5-1. Apparatus constants for STEM simulations

Parameters	Value / unit
Spherical aberration (Cs)	-464.3 nm
Illumination semi angle (β)	25.8 mrad
Width of electron energy fluctuations	0.85 eV
Convergence angle (α)	17.9 mrad
Half-peak angle of the annular detector	9.2 mrad (inner), 20 mrad (outer)
Acceleration voltage	60 kV

5.2.9 Gas permeation measurement

Gas permeation measurements were conducted using the apparatus described in Chapter 1. For pure gas measurements, the VOCs of EtOAc, MEK, and DCM were frozen using liq. N_2 and degassed by pumping. After degassing, the VOC was heated to room temperature (25 °C), and VOC vapor was introduced into the manifold at a total pressure of 10^4 Pa, which was below the saturated vapor pressure of EtOAc, MEK, and DCM. N_2 was introduced into the gas manifold using a mass flow controller at the total pressure of

10^4 Pa. The VOC–N_2 mixture was prepared by introducing VOC and N_2 at different partial pressure ratios at a total pressure of 1×10^4 Pa. All experiments were repeated at least three times.

5.3 Results and Discussion

5.3.1 Structural characterization of COF films

The relationships between the number of repetitions of the precursor deposition and the thicknesses of the H-COF and F-COF films are shown in Fig. 5-2a and 5-2b, respectively. There is a linear relationship between the number of repetitions and film thickness. Cross-sectional SEM images of the H-COF (Fig. 5-2c) and F-COF films (Fig. 5-2d) at 100 repetitions of precursor deposition with thickness of 4.66 and 1.64 μm, respectively, were observed without apparent defects and pinholes. The AFM image of the H-COF film showed that plate-like structures of ca. 1–5 μm in length with a height of ca. 100–450 nm were grown randomly on the substrate (Fig. 5-2e). On the other hand, rod-like structures with a height of ca. 50–300 nm tended to grow perpendicular to the substrate in the F-COF films (Fig. 5-2f). This result indicates that the crystal orientations of the H-COF and F-COF films are different. The root-mean-square surfaces of the H-COF and F-COF films were 69 nm and 51 nm, respectively.

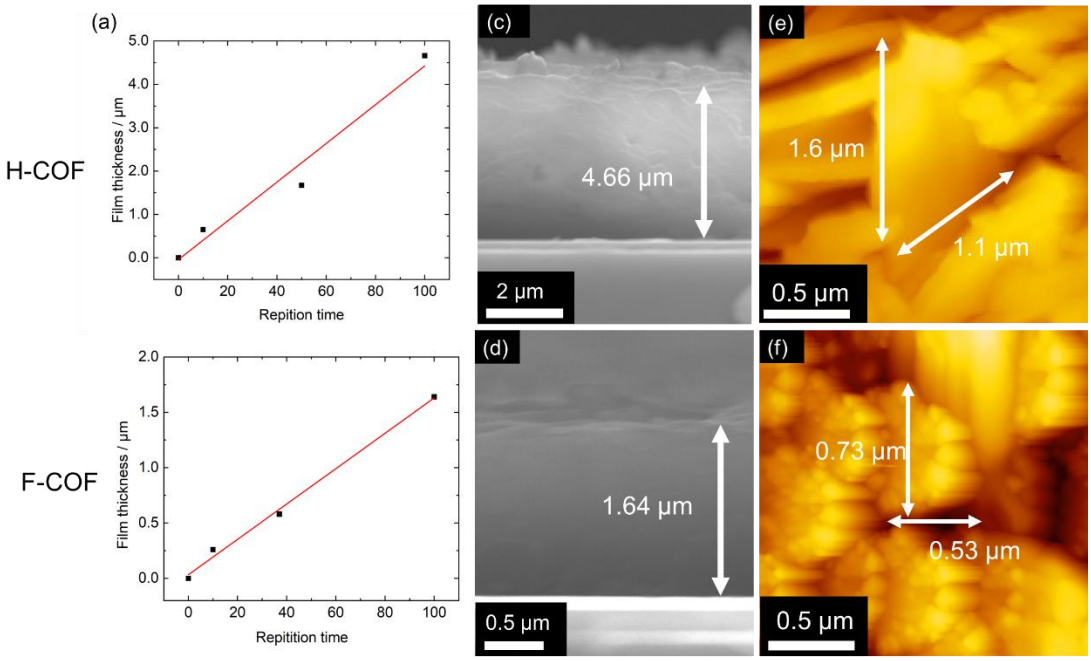

Fig. 5-2. Repetition time dependence of the film thickness of (a) H-COF and (b) F-COF films. Cross-section FE-SEM images of (c) H-COF and (d) F-COF films. AFM images of the (e) H-COF and (f) F-COF films with height profiles at the white line in Fig.

Imine formation between the amine and aldehyde moieties was evaluated using FTIR and Raman spectroscopy. From the FTIR spectra of F-COF film (Fig. 5-3a), the imine formation and precursor consumption were confirmed ("a" symbol for imine of –C=N at 1592 cm^{-1} and "b" symbol for $-NH_2$ and –CHO at 3354 cm^{-1} and 1683 cm^{-1}, respectively). The Raman spectra (Fig. 5-3b) also revealed imine formation ("a" symbol at 1592 and 1562 cm^{-1}, corresponding to aromatic C=C and imine moieties, respectively). The relatively small peak at ca. 1625 cm^{-1} can be attributed to the TAPB or F-TFPB moieties at 1610 and 1624 cm^{-1}, respectively. This result suggests that the functional groups from the precursors remained locally due to the reversibility of the imine bond.

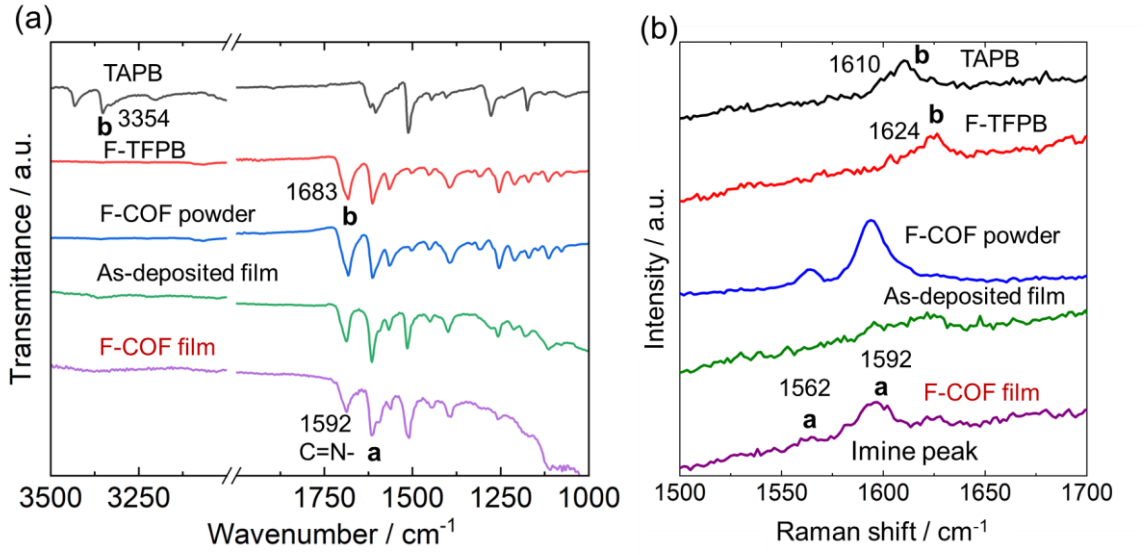

Fig. 5-3. (a) FTIR and (b) Raman spectra of the F-COF films and their precursors.

The crystallinity of the H-COF and F-COF films prepared on Si/SiO_2 substrates was confirmed by out-of-plane and in-plane XRD. The out-of-plane XRD results show that the H-COF film with a thickness of ca. 4.7 μm exhibits multiple diffraction peaks corresponding to 100, 200, 110, 210, and 310 reflections at 2θ angles of 4.0°, 7.0°, 8.2°, 10.4°, and 14.4°, respectively (Fig. 5-4a). An F-COF film with a thickness of ca. 1.6 μm also exhibited diffraction peaks corresponding to 100, 200, 110, 210, and 310 reflections at 2θ angles of 4.1°, 7.1°, 8.1°, 10.8°, and 14.5°, respectively (Fig. 5-4b). The crystalline domain sizes of H-COF and F-COF films calculated from 100 refractions using the Scherrer equation were 25.0 and 25.6 nm, respectively. The areas of the crystals on the plane parallel to 100 in the H-COF and F-COF films were estimated to be 25^2=625 and

$25.6^2 = 655$ nm^2, respectively. The pore diameters of H-COF and F-COF were ca. 2.2 nm, the area of the porous regions was estimated to be 3.14 nm^2 by assuming an ideal hexagonal shape. It was also estimated that ca. 199 and 208 pores were present in the H-COF and F-COF films, respectively. The in-plane XRD patterns of H-COF and F-COF showed 100 reflections at a $2\theta/\chi$ angle of 3.8° (Figs. 5-4c and d).

For the H-COF film, the peak intensity of 110 was greater than that of 200, but smaller than that of 210. In contrast, in the F-COF film, the peak intensities of 110 and 200 were almost the same, and the peak intensity of 110 was slightly greater than that of 210. These results can be attributed to the difference in the orientation between the H-COF and F-COF films.

In order to quantitatively estimate the crystal orientation of the COF films, the smallest mean square error (MSE) between the simulated and experimental XRD intensities was calculated. The model structure is assumed to be the co-existence of AA- and AB-stacking structures with a ratio of R_{AA} and $R_{AB} = 1\text{-}R_{AA}$, respectively. The optimal XRD patterns for H-COF and F-COF are shown in Figs. 5-4a and b, respectively (black line indicates coexisting AA and AB). The Reliability factors (Rp) for the H-COF and F-COF films were 4.01% and 4.22%, respectively. The weighted reliability factor R_{wp} was 7.45% and 7.63% for H-COF and F-COF, respectively. These R_{wp} values indicate

satisfactory fitting because R_{wp} typically ranges from 7–13% for Rietveld analysis of low-crystalline powder samples [23]. The ratios of R_{wp} to R_p for H-COF and F-COF are 1.86 and 1.81, respectively, further suggesting adequate fitting due to being below 2. The optimized Euler angles (Ψ, Θ, Φ), March–Dollase parameter of r_M, and existence ratio of the R_{AA} are summarized in Table 5-2. The ratio of AA stacking was 88.5% for the H-COF film and 99.5% for the F-COF film. As I will discuss later, DFT calculation showed that the stabilization energy of AA-stacking is greater than that of AB-stacking in H-COF and F-COF, and the difference is greater in F-COF. It reasonably accounts for the dominance of AA stacking in the present COF films, especially in F-COF. In addition, AB stacking with disordered interlayer formation easily occurs in the H-COF film compared to the F-COF film. The Initial (black line) and optimized orientations to best fit the observed XRD (red line) unit cells of H-COF and F-COF with AA- and AB-stacking models are illustrated in Fig. 5-5, suggesting a relatively strong perpendicular orientation to the substrate.

In the case of fitting without considering orientation, i.e., (Ψ,Θ,Φ)=(0,0,0) and r_M=1, the calculation converged to R_{AA}=1. The Parameters of optimized orientation to best fit experimental XRD calculated from single component stacking structures are shown in Table 5-3. A comparison of R_p and R_{wp} calculated with and without crystal

orientation is presented in Fig. 5-6. The R_{wp} was minimized when fitting was performed under the assumption of both AA and AB-stacking structures with consideration of specific orientation. This result confirmed that the fitting could be improved by accounting for multiple orientations.

Table 5-2. Optimized orientation parameters of H-COF and F-COF films calculated under co-existing of AA and AB-stackings.

COF	Stacking	Ψ / º	Θ / º	Φ / º	r_M	R_{AA} and R_{AB} /%
H-COF	AA	164.3	65.9	81.3	8.18×10^{-4}	88.5
	AB	280.4	97.1	203.6	1.92×10^{-1}	11.5
F-COF	AA	135.0	81.2	93.2	5.09×10^{-1}	99.5
	AB	304.1	100.9	35.1	2.37×10^{-3}	0.5

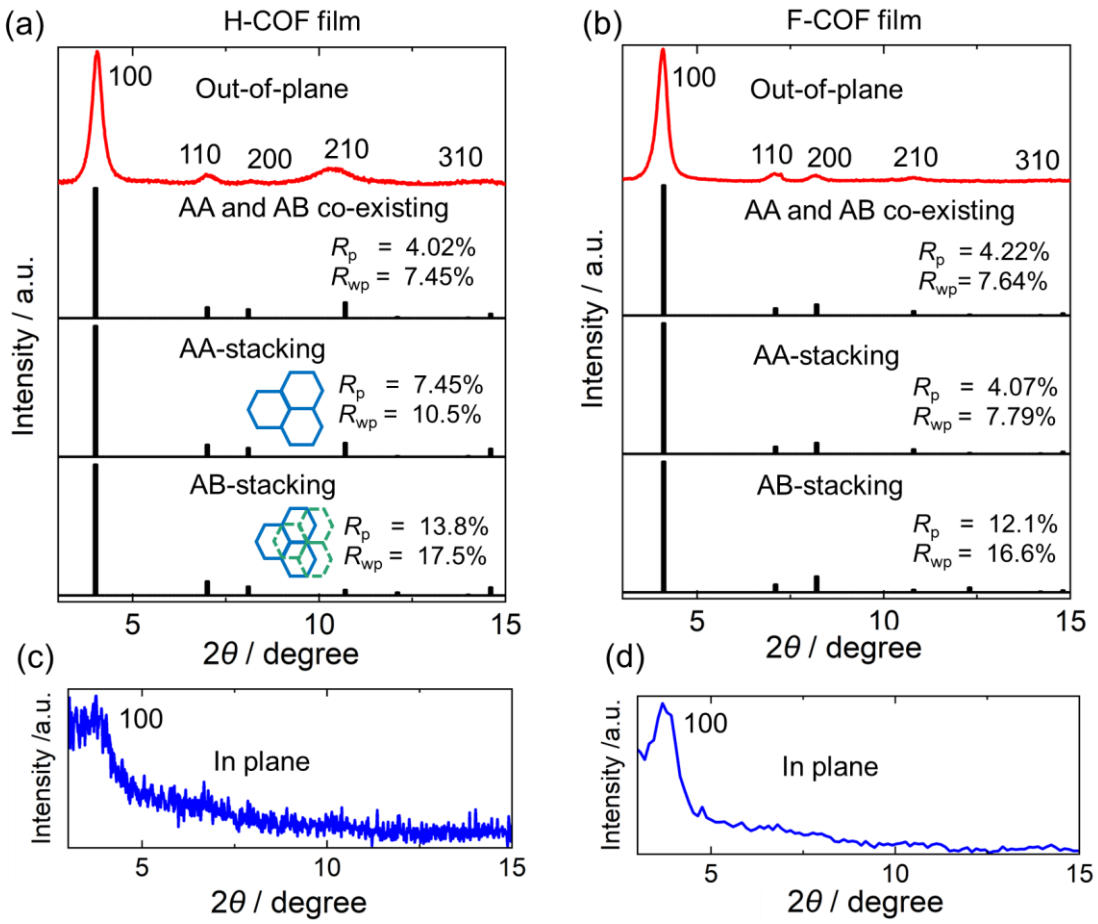

Fig. 5-4. (a) H-COF and (b) F-COF films for out-of-plane and optimized calculated XRD patterns. The calculated patterns are obtained by the structure of AA-and AB-stacking and their mixtures with optimized orientation to best fit the observed XRD patterns. In-plane XRD patterns of (c) H-COF and (d) F-COF films.

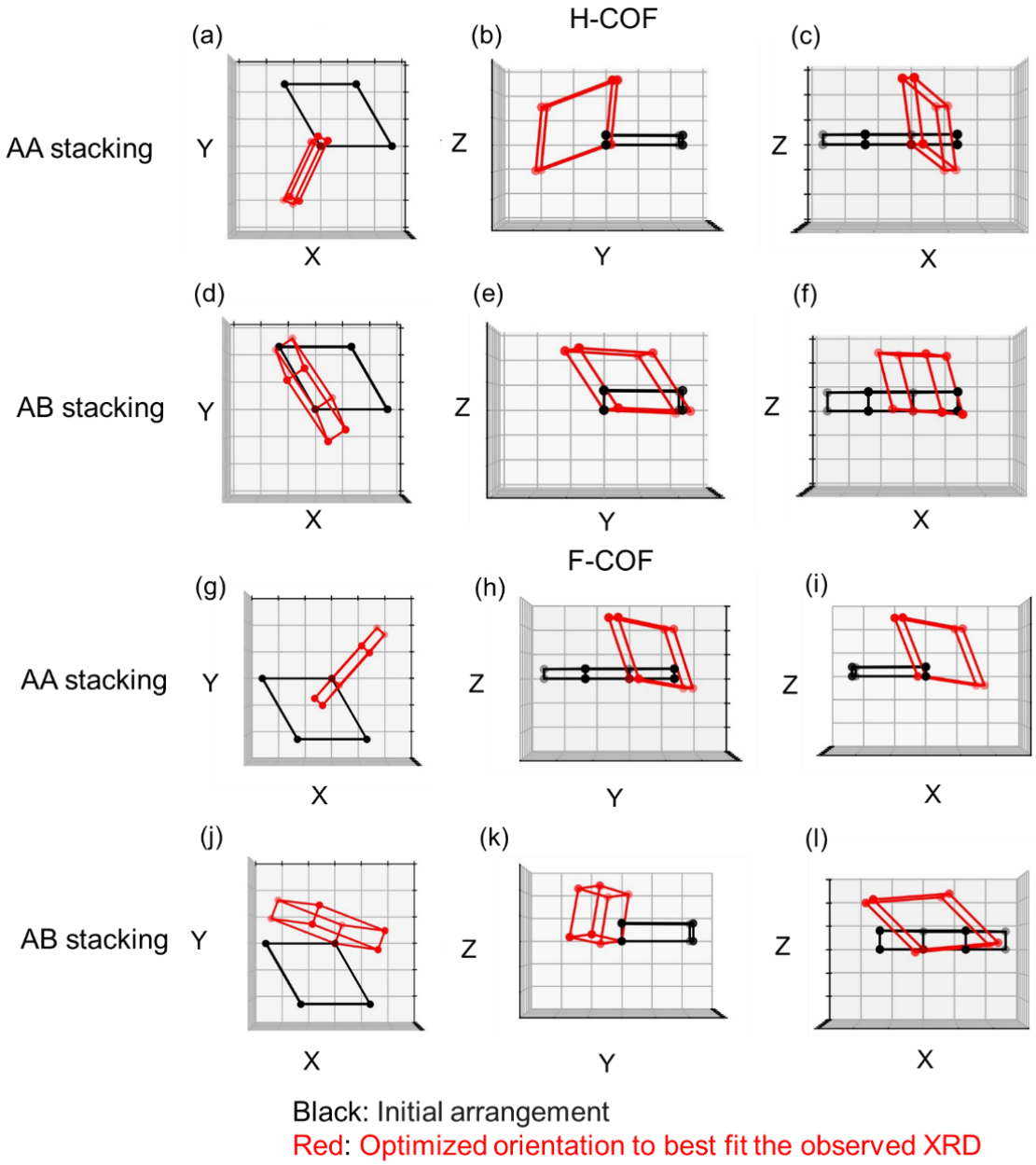

Fig. 5-5. Initial (black line) and optimized orientations to best fit the observed XRD (red line) unit cells. H-COF with AA-stacking and AB-stacking was viewed from the (a), (d) XY, (b), (e) YZ, and (c), (f) ZX planes, respectively. F-COF with AA-stacking and AB-stacking was viewed from the (g), (j) XY, (h), (k) YZ, and (i), (l) ZX planes, respectively.

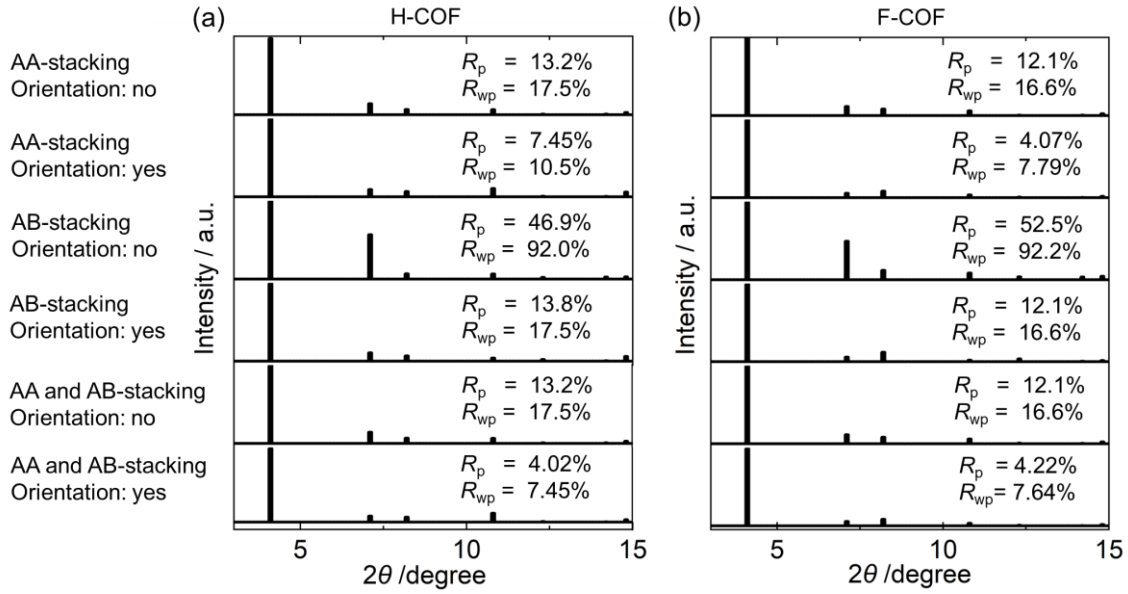

Fig. 5-6. Calculated XRD patterns of (a) H-COF and (b) F-COF with and without orientations. R_p and R_{wp} are shown in each calculated pattern.

Table 5-3. Parameters of optimized orientation to best fit experimental XRD calculated from single component stacking structures

COF	Stacking	Ψ / º	Θ / º	Φ / º	r_M
H-COF	AA	143.7	86.5	250.6	0.414
	AB	123.4	116.2	258.5	0.146
F-COF	AA	119.4	36.7	274.1	0.462
	AB	139.8	118.5	174.5	0.190

I also confirmed the differences in the crystallinity of the F-COF films based on the composition of vapors during annealing. Figure 5-7 exhibited that the appropriate composition of the mixed vapors (mesitylene: dioxane: AcOH = 9:1:1 volume ratio) is also important for the crystallization of the F-COF film.

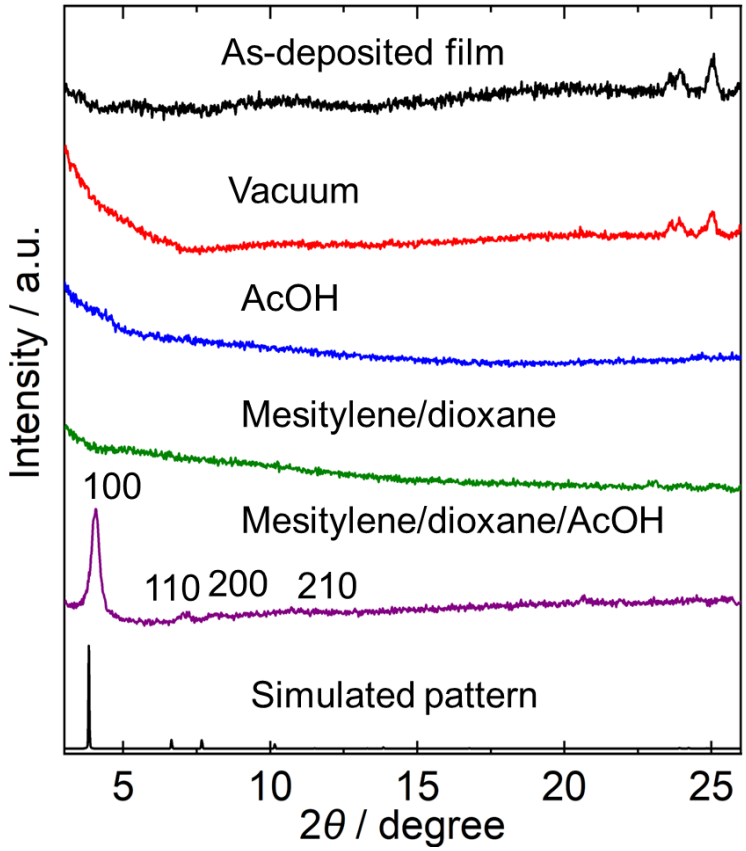

Fig. 5-7. XRD patterns of the F-COF films under various annealing conditions.

STEM was performed to examine the nanostructures of the COF films. The H-COF film exhibits a layer-stacked structure with an interlayer distance of ca. 0.35 nm, which is consistent with the DFT-simulated structure (Fig. 5-8a). The H-COF film also exhibited a lattice fringe with the average distance of vertical and horizontal lines of 1.2

and 0.45 nm, respectively (Fig. 5-8b). It is estimated that these vertical and horizontal fringes correspond to half of the a-axis (2.6/2=1.3 nm) and the tangent 52° of the c-axis (0.35×tan(52°)=0.44 nm). These lengths can be reproduced by the crystal orientation at Euler angles (Φ, Θ, Ψ) = (180°, 45°, 90°), corresponding to the crystal zone axes of 2 1 16 and 2 1 9 for AA- and AB-stacking structures, respectively. The AB-stacking simulation exhibited vertical and horizontal lines with distances of 1.3 and 0.44 nm, respectively (Fig. 5-8c). In contrast, the AA stacking simulation only presented vertical lines (Fig. 5-8d). Interestingly, only the AB stacking related structure was observed in STEM, although the XRD analysis suggested that AB-stacking merely existed in ca. 10%.

From the low-magnification STEM image of the F-COF film, a layered structure like an “onion” was observed (Fig. 5-8e). This structure was similar to the onion structure of the H-COF film[24]. The high-magnification image confirms that the interlayer distance of the F-COF film was ca. 0.35 nm (Fig. 5-8f). Since branching of layers was observed in the F-COF film, it can be noted that layer-by-layer growth proceeded. This result indicates that growing the first layer in a planar plane is a suitable strategy for synthesizing F-COF films with the layers grown parallel to the substrate.

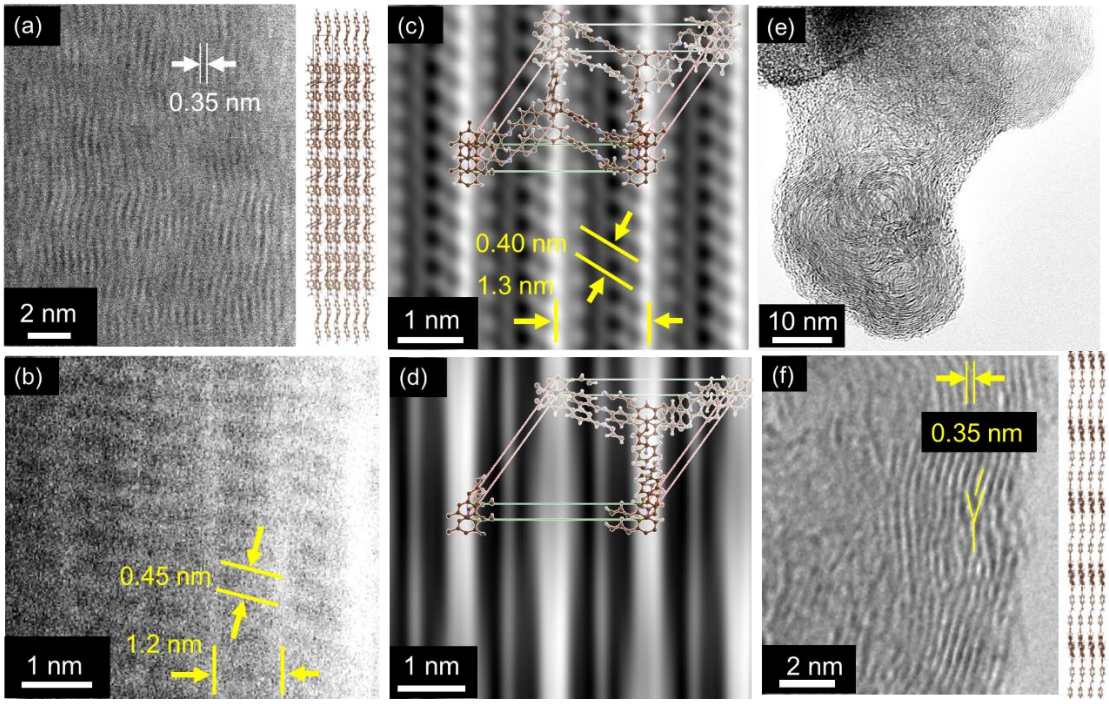

Fig. 5-8. (a) High-magnification STEM image of H-COF film with calculated layer stacking structure. (b) Lattice fringe of the H-COF film. Simulated STEM images of H-COF for (c) AB and (d) AA stacking structures obtained from the crystal orientation at Euler angles (Φ, Θ, Ψ) = (180, 45, 90). (e) Low-magnification and (f) high-magnification STEM images of the F-COF film with calculated structure. The calculated structures were visualized using the VESTA software[20].

5.3.2 Gas permeation performances

The gas permeation performances of the H-COF and F-COF films were examined using COF films directly prepared on the AAO supports. FE-SEM images of H-COF and F-COF on AAO showed no significant defects in the films, which acted as free paths for gas permeation (Fig. 5-9).

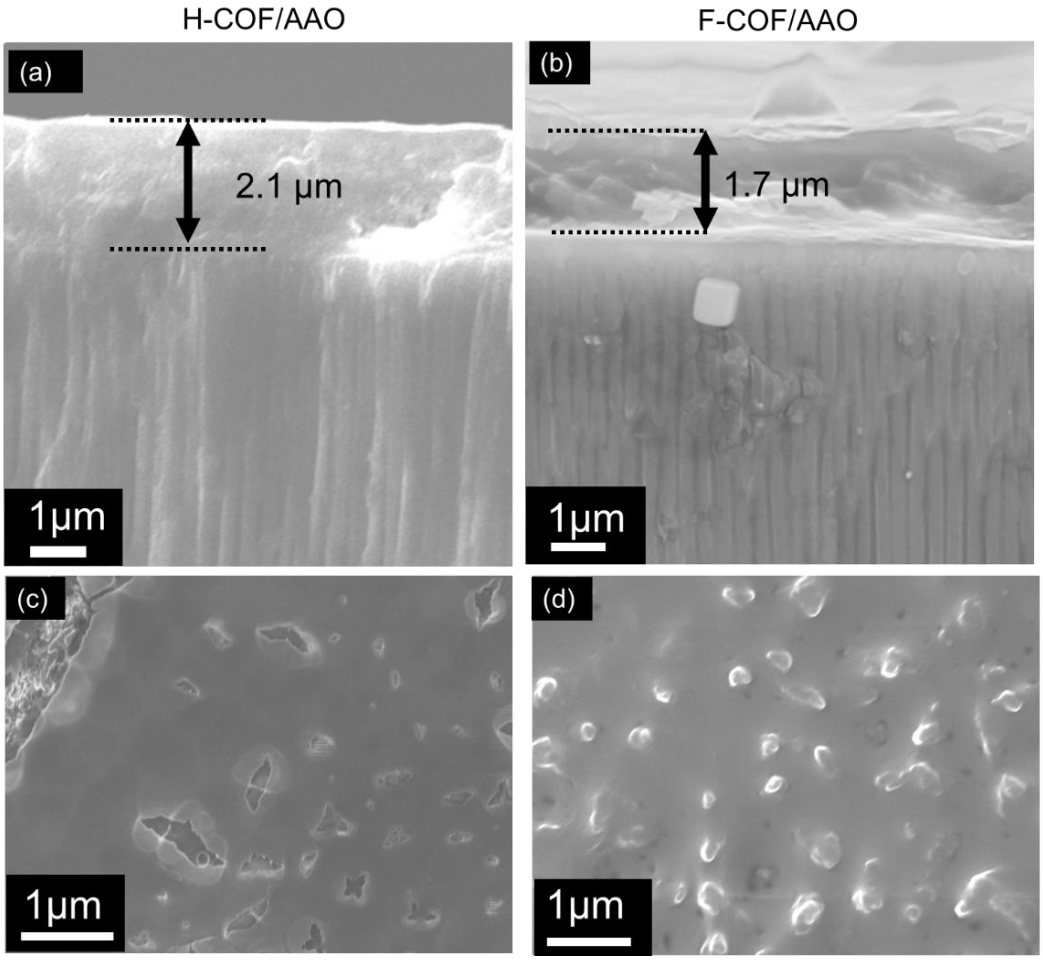

Fig. 5-9. Cross-sectional FE-SEM images of (a) H-COF and (b) F-COF films prepared on AAO supports. Top-view FE-SEM image of (c) H-COF and (d) F-COF prepared on AAO support.

Because the gas permeability of AAO was much greater than that of the H-COF and F-COF films, gas permeation through AAO was ignored. The boiling-point dependence of the gas permeabilities of the H-COF and F-COF films at a feed gas pressure of 10^4 Pa (below the saturated vapor pressure) is shown in Fig. 5-10. Both the H-COF and F-COF films exhibited a tendency to increase gas permeability by increasing the boiling point of the gases. The permeability of VOC gases such as EtOAc and MEK was up to 20 times greater than that of N_2. It has been reported that COF films with relatively large pores (ca. 2–3 nm) do not exhibit the molecular sieve effect for CO_2–N_2 or CO_2–CH_4 separation[25]. H-COF and F-COF also exhibited large pores (ca. 2.2 nm) compared to traditional polymers (several angstroms); thus, these pores acted as a gas permeation pathway without a molecular sieving effect, but by a solution–diffusion mechanism. The permeability of EtOAc for F-COF (2679 Barrer) was 2.8 times greater than that of the H-COF film (942 Barrer); otherwise, the EtOAc/N_2 permeation ratio of the F-COF film (25.8) was slightly greater than that of the H-COF film (21.4).

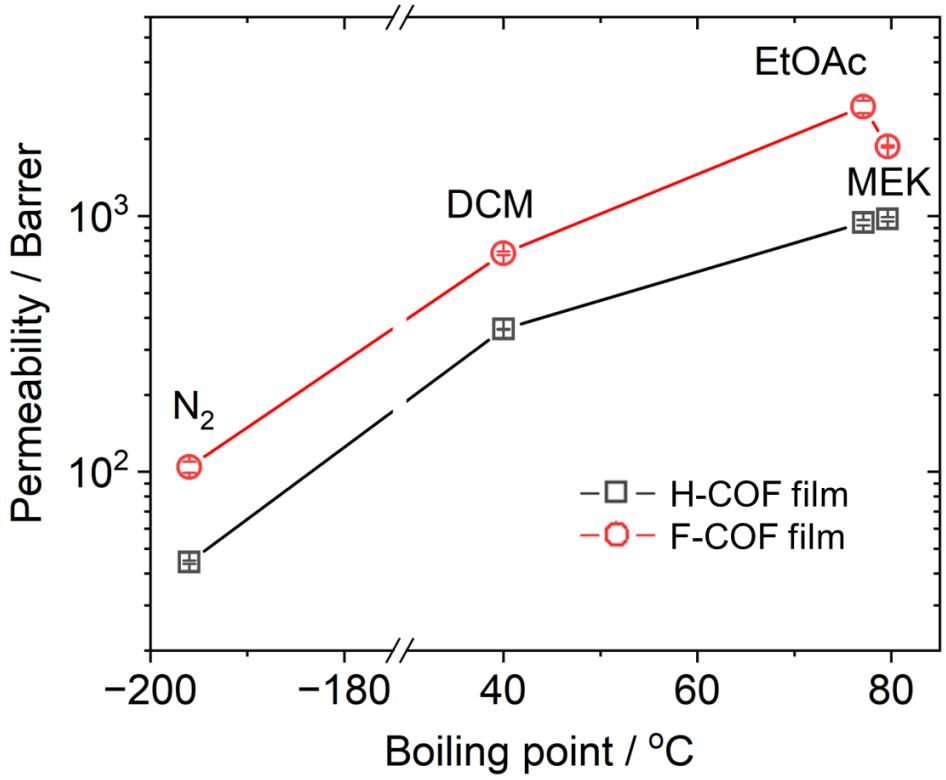

Fig. 5-10. Boiling point dependence of permeability for H-COF and F-COF films. Error bars represent standard deviation of multiple experiments.

The separation factor of the EtOAc–N_2 mixture for H-COF and F-COF (1% EtOAc in N_2 with a total feed pressure of $\times 10^4$ Pa) was 6.3 and 6.7 times lower than that of the permeation ratio of pure EtOAc and N_2 for H-COF and F-COF, respectively (Table 5-4). This result is attributed to the swelling of the polymer film[26], which increases the N_2 permeability when EtOAc permeates the COF film.

Table 5-4. EtOAc/N_2 separation factor of H-COF and F-COF film from EtOAc concentration of 1%

Sample	EtOAc/N_2 separation factor
H-COF film	3.2
F-COF film	4.1

The diffusion coefficients of the H-COF and F-COF films ranged from 10^{-14} to 10^{-13} m^2 s^{-1} order of magnitude (Fig. 5-11a). On the other hand, the solubility of VOC tended to increase with an increase in the boiling point of VOC (Fig. 5-11b). This result indicates that the permeation behavior of the H-COF and F-COF films is dominated by solubility, which is similar to that of conventional polymeric membranes.

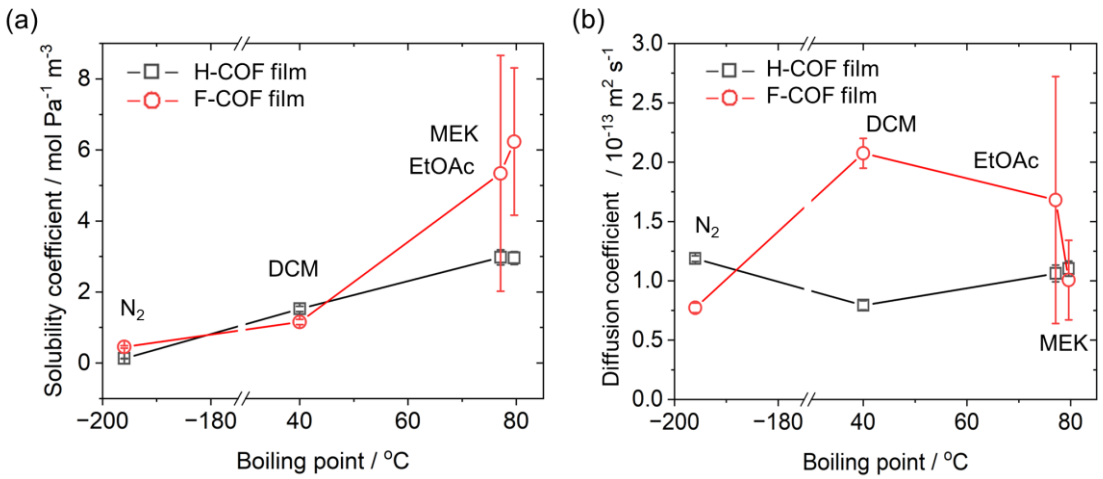

Fig. 5-11. Boiling-point dependence of (a) gas solubility coefficient for H-COF (black) and F-COF (red) films. (b) Gas diffusivity of the H-COF and F-COF films.

5.3.3 Interaction energies between VOC and COFs

The gas absorption energies and absorption sites of the H-COF and F-COF moieties were estimated using DFT-D (Fig. 5-12). The results showed that the interaction energy generally increased with increasing boiling point, indicating a high affinity of VOC for COF. The interaction energy of F-COF for EtOAc (-47.9 kJ mol^{-1}) was 8.8 times greater than that for N_2 (-5.46 kJ mol^{-1}). In comparison, the interaction energy of H-COF for EtOAc (-31.3 kJ mol^{-1}) was 4.9 times greater than that of H-COF (-6.40 kJ mol^{-1}). The significant interaction energy for F-COF was attributed to the electron-negative F atom, which increased the absorption interaction between the EtOAc and F-COF frameworks. Considering the calculations and permeation experiments, a synthetic strategy can be proposed to improve the gas permeability of COF films by increasing their interactions with VOC.

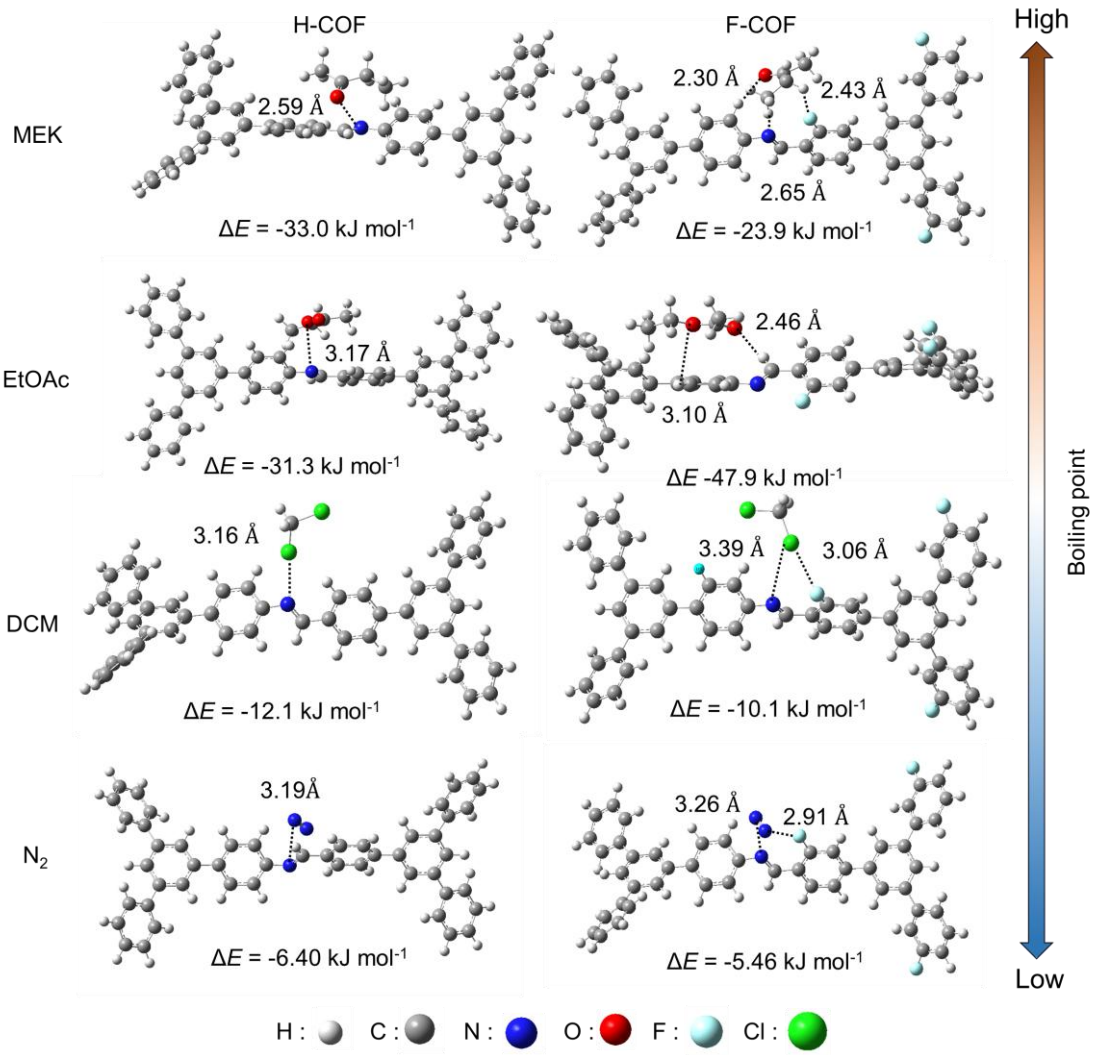

Fig. 5-12. Interaction energy between H- or F-COF and various molecules.

5.3.4 Chemical stability

The chemical stabilities of the COF films were evaluated. The XRD patterns of the COF films immersed in EtOAc, MEK, or DCM for 24 h are shown in Fig. 5-13a. The diffraction intensity from the 100 facets disappeared from the H-COF films after 24 h of immersion in each solvent. This result is attributed to the disruption of pore orientation by the incorporation of solvents in the pores[27]. However, the diffraction intensity from 100 facets in the F-COF film remained slightly decreased after 24 h of immersion (Fig. 5-13b).

The relatively high chemical stability of the F-COF films was estimated using DFT calculations. The interlayer stacking energies of the H-COF and F-COF were calculated. The stacking energy per unit area (Es) calculated using DFT-D is shown in Fig. 5-13c. H-COF and F-COF at the AA-stacking configuration have Es of -0.28 and -0.29 eV nm^{-2}, respectively. These values are consistent with the interlayer energies of the layered materials calculated using DFT-D[28]. The stacking energies of H-COF and F-COF for the AA configurations were 1.4 and 1.5 times greater than those for the AB configurations, respectively. This result suggests that AA-stacking configurations were favorably formed due to the large overlap of the aromatic moieties, consistent with the dominance of the AA-stacking fraction (R_{AA}) confirmed from XRD fitting. The interlayer

stacking energy diagrams estimated from the crystalline domain size obtained by XRD of H-COF and F-COF are shown in Fig. 5-13d. The stacking energies of the crystalline domains were assessed using the crystal areas calculated using XRD (H-COF and F-COF of 625 and 655 nm^2, respectively). The interaction energy of AA stacking for F-COF (-191 eV) was 1.1 times greater than that for H-COF (-173 eV). This result indicates that the electron-negative F atom can increase the interaction of layers[29,30] :thus, the good resistivity of the solvent incorporated into the pores induces disruption. The energy difference between the AA and AB stacking of F-COF (-191 eV) was 1.6 times greater than that of H-COF (-123 eV). This result indicates that the greater AA-stacking fraction (R_{AA}) in the F-COF film compared to the H-COF film, as determined by XRD fitting, can be attributed to the increased strong interactions in the F-COF film caused by the electronegative F atoms. Furthermore, such interlayer stabilization can contribute to the high chemical stability of the F-COF film. This enhancement of the stability of COF films through modifications in the framework structure caused is advantageous for practical applications of COF films, such as in separation for multicomponent organic vapor systems.

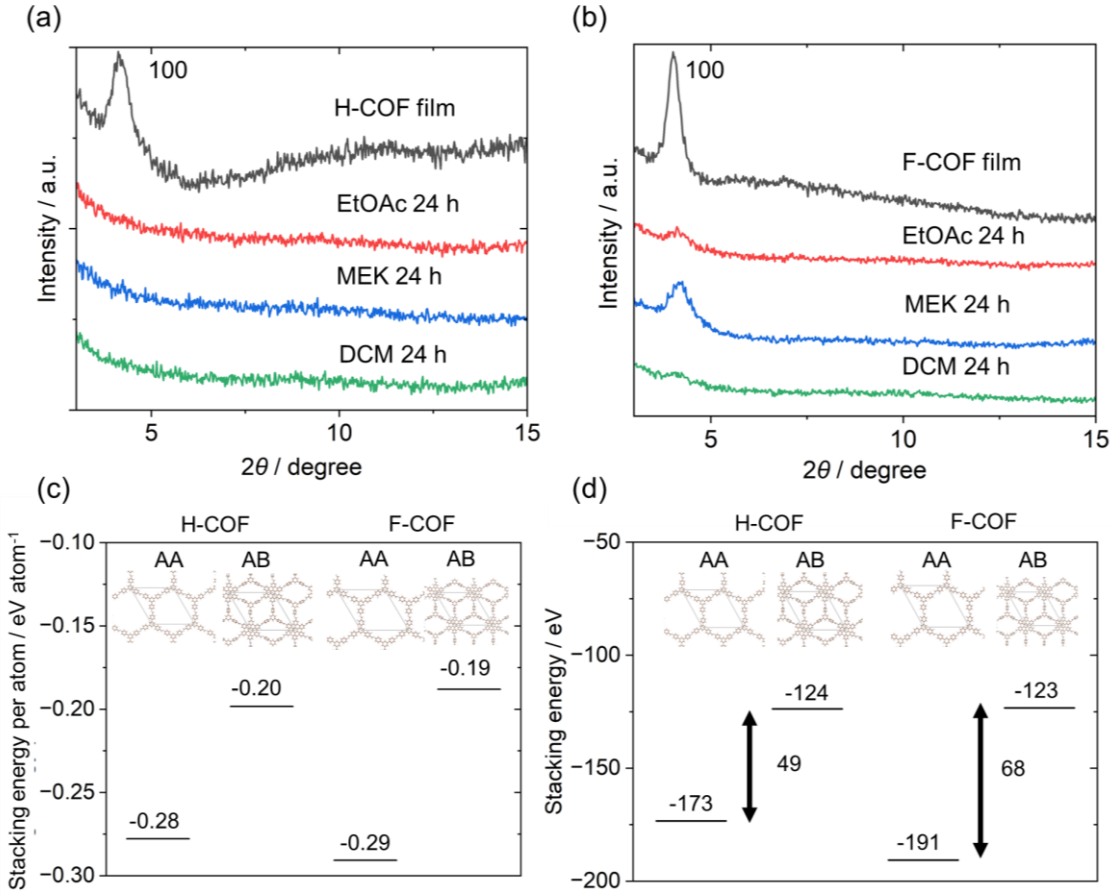

Fig. 5-13. XRD patterns of (a) H-COF and (b) F-COF films after immersion in EtOAc, MEK, or DCM for 24 h. Stacking energy diagrams of H-COF and F-COF (c) per atom (d) based on crystal domain size.

5.3.5 Comparison with the literature of VOC membrane separation properties

The VOC separation performance of the membranes reported in the literature was compared. The VOC/N_2 selectivities of the H-COF and F-COF films are not surprisingly greater than those of polymeric membranes reported in the literature, such as PDMS (Table 5-5). Further refinement of the COF design is necessary to improve VOC separation performance. For example, reducing the size of COF pores (<1 nm) is expected to introduce a size-sieving effect by increasing the diffusivity selectivity in the separation of VOCs.

Table 5-5. VOC permeation performances of the literature membranes

Name	Gas	Permeability of faster gas	Selectivity	Ref.
PDMS–ZIF	EtOAc/N_2	ca. 10000 Barrer	ca. 150	[5]
PDMS	EtOAc/N_2	11000 Barrer	40	[2]
PDMS–PVDF	EtOAc/N_2	100–200 mL min^{-1}	13–100	[31]
Trip-BTDA–PI	N_2/cyclohexane	N_2 of 60 L/(m^2·h)	99	[4]
PDMS–polyamide	Cyclohexane / N_2	ca. 7800 Barrer	ca. 48	[1]
PDMS	DCM/N_2	42600 Barrer	142	[32]
Pebax–ECuCOF-2wt%	Toluene /*n*-heptane	937 g m^{-2} h^{-1}	4.7	[14]
Pebax–TpPa-COOH	Toluene/N_2	2000 Barrer	674	[15]
H-COF	EtOAc/N_2	942 Barrer	21	**This work**
	MEK/N_2	972 Barrer	22	
	DCM/N_2	361 Barrer	8.2	
F-COF	EtOAc/N_2	2679 Barrer	26	**This work**
	MEK/N_2	1872 Barrer	18	
	DCM/N_2	715 Barrer	6.9	

5.4 Conclusion

This chapter presents the versatility of alternating vapor deposition for the preparation of functionalized COF films for VOC and N_2 separation. Structural analysis confirmed the formation of imine bonds and successful synthesis of COF films with a well-defined layered stacking orientation. Based on the comparison of simulation and experimental results, it was suggested that more than 99% of the crystal structure in the F-COF film exhibited AA stacking, which was induced by relatively strong interlayer interactions due to the electron negative F atom. The ratio of AB-stacking (disordered layer structure) in H-COF films was greater than that of F-COF films, which also confirmed by directly observing of AB-stacking structure using STEM. Both the H-COF and F-COF films exhibited considerable VOC/N_2 selectivity. In particular, the gas permeability of the F-COF film was greater than that of the H-COF film due to the increased interaction between the VOC and COF frameworks. In addition, the F-COF film possessed improved chemical stability in VOC solvents due to the enhanced stacking caused by the interaction of F atoms. This research opens a new avenue for synthesizing a COF film through the vapor phase for practical gas separation applications, including VOC.

References

[1] B. Shen, S. Zhao, X. Yang, M. Carta, H. Zhou, W. Jin, Relation between permeate pressure and operational parameters in VOC/nitrogen separation by a PDMS composite membrane, Sep. Purif. Technol. 280 (2022) 119974.

[2] W. Yang, H. Zhou, C. Zong, Y. Li, W. Jin, Study on membrane performance in vapor permeation of VOC/N_2 mixtures via modified constant volume/variable pressure method, Sep. Purif. Technol. 200 (2018) 273–283.

[3] X. Feng, S. Sourirajan, H. Tezel, T. Matsuura, Separation of organic vapor from air by aromatic polyimide membranes, J. Appl. Polym. Sci. 43 (1991) 1071–1079.

[4] C. Zhang, X. Gao, J. Qin, Q. Guo, H. Zhou, W. Jin, Microporous polyimide VOC-rejective membrane for the separation of nitrogen/VOC mixture, J. Hazard. Mater. 402 (2021) 123817.

[5] F. Şahin, B. Topuz, H. Kalıpçılar, ZIF filled PDMS mixed matrix membranes for separation of solvent vapors from nitrogen, J. Memb. Sci. 598 (2020) 117792.

[6] B. Ozturk, C. Kuru, H. Aykac, S. Kaya, VOC separation using immobilized liquid membranes impregnated with oils, Sep. Purif. Technol. 153 (2015) 1–6.

[7] G. Sui, J. Li, A. Ito, Separation of VOC vapor from air by a surface-soaked liquid membrane module using triethylene glycol, Sep. Purif. Technol. 68 (2009) 283–287.

[8] D.W. Burke, Z. Jiang, A.G. Livingston, W.R. Dichtel, 2D covalent organic framework membranes for liquid-phase molecular separations: State of the field, common pitfalls, and future opportunities, Adv. Mater. 36 (2024) e2300525.

[9] Z. Zhang, H. Yang, C. Cao, Y. Liu, S. Liang, M. Wang, H. Wang, X. Cao, F. Pan, H. Wu, Z. Jiang, Vapor-liquid interfacial polymerization of covalent organic framework membranes for efficient alcohol dehydration, J. Memb. Sci. 641 (2022) 119905.

[10] K. Banjerdteerakul, H. Peng, K. Li, Covalent organic frameworks based membranes for separation of azeotropic solvent mixtures by pervaporation, J. Memb. Sci. 678 (2023) 121679.

[11] G. Wu, X. Lu, Y. Li, Z. Jia, X. Cao, B. Wang, P. Zhang, Two-dimensional covalent organic frameworks (COF-LZU1) based mixed matrix membranes for pervaporation, Sep. Purif. Technol. 241 (2020) 116406.

[12] L. Zhang, L. Wang, N. Wang, H. Guo, W.-H. Zhang, X. Li, S. Ji, Q.-F. An, Covalent organic frameworks hybird membrane with optimized mass transport nanochannel for aromatic/aliphatic mixture pervaporation, J. Memb. Sci. 598 (2020) 117652.

[13] H. Yang, H. Wu, Y. Zhao, M. Wang, Y. Song, X. Cheng, H. Wang, X. Cao, F. Pan, Z. Jiang, Ultrathin heterostructured covalent organic framework membranes with interfacial molecular sieving capacity for fast water-selective permeation, J. Mater. Chem. A 8 (2020) 19328–19336.

[14] J. Du, S. Liang, M. Wang, Y. Wang, T. Yi, Z. Zhang, F. Pan, Z. Jiang, Metal-covalent organic framework nanosheets engineered facilitated transport membranes for toluene/n-heptane separation, J. Memb. Sci. 683 (2023) 121840.

[15] J. Zhao, J. Liu, Y. Wang, J. Du, Z. Zhu, Y. Wang, J. Zhao, M. Long, F. Pan, Z. Jiang, Covalent organic frameworks filled Pebax hybrid membrane for efficient toluene/N_2 separation, J. Memb. Sci. 700 (2024) 122676.

[16] S.B. Alahakoon, G.T. McCandless, A.A.K. Karunathilake, C.M. Thompson, R.A. Smaldone, Enhanced structural organization in covalent organic frameworks through fluorination, Chemistry 23 (2017) 4255–4259.

[17] G. Kresse, J. Hafner, Ab initio molecular dynamics for liquid metals, Phys. Rev. B 47 (1993) 558–561.

[18] J.P. Perdew, K. Burke, M. Ernzerhof, Generalized gradient approximation made simple, Phys. Rev. Lett. 77 (1996) 3865–3868.

[19] S. Grimme, J. Antony, S. Ehrlich, H. Krieg, A consistent and accurate ab initio parametrization of density functional dispersion correction (DFT-D) for the 94 elements H-Pu, J. Chem. Phys. 132 (2010) 154104.

[20] K. Momma, F. Izumi, *VESTA*: a three-dimensional visualization system for electronic and structural analysis, J. Appl. Crystallogr. 41 (2008) 653–658.

[21] P.J. Brown, A.G. Fox, E.N. Maslen, M.A. O'Keefe, B.T.M. Willis, Intensity of diffracted intensities, in: International tables for crystallography, international union of crystallography, Chester, England, 2006: pp. 554–595.

[22] Y. Seto, M. Ohtsuka, ReciPro: free and open-source multipurpose crystallographic software integrating a crystal model database and viewer, diffraction and microscopy simulators, and diffraction data analysis tools, J. Appl. Crystallogr. 55 (2022) 397–

410.

[23] 葛巻 貴大, 粉末 X 線回折法 基礎講座 第 5 回定量分析, リガクジャーナル 53 (2022) 10-15.

[24] Q. Zheng, X. Li, Q. Zhang, D. Lee, H. Mao, C. Yang, K.C. Bustillo, J.A. Reimer, Y. Liu, J. Jiang, H. Zheng, A covalent organic framework onion structure, Mater. Today 60 (2022) 98–105.

[25] J.E. Lopez-Cazares, K. Kim, J.Y.S. Lin, K. Jin, Gas permeation and separation characteristics of microporous TpHz COF membranes synthesized by substrate-assisted interfacial polymerization, Ind. Eng. Chem. Res. 63 (2024) 3684–3694.

[26] L. Liu, A. Chakma, X. Feng, D. Lawless, Separation of VOCs from N_2using poly(ether block amide) membranes, Can. J. Chem. Eng. 87 (2009) 456–465.

[27] G. Cheng, C. Sui, W. Hao, J. Li, Y. Zhao, L. Miao, G. Zhao, J. Li, Y. Sang, C. Zhao, L. Wen, X. He, C. Wang, Ultra-strong Janus covalent organic framework membrane with smart response to organic vapor, Small 20 (2024) 2401635.

[28] P. Tao, H.-H. Guo, T. Yang, Z.-D. Zhang, Stacking stability of MoS_2 bilayer: An ab initio study, Chin. Physics B 23 (2014) 106801.

[29] S.B. Alahakoon, G. Occhialini, G.T. McCandless, A.A.K. Karunathilake, S.O. Nielsen, R.A. Smaldone, Experimental and theoretical insight into the effect of fluorine substituents on the properties of azine linked covalent organic frameworks, Cryst. Eng. Comm. 19 (2017) 4882–4885.

[30] W.A. Braunecker, K.E. Hurst, K.G. Ray, Z.R. Owczarczyk, M.B. Martinez, N. Leick, A. Keuhlen, A. Sellinger, J.C. Johnson, Phenyl/perfluorophenyl stacking interactions enhance structural order in two-dimensional covalent organic frameworks, Cryst. Growth Des. 18 (2018) 4160–4166.

[31] H. Zhen, S.M.J. Jang, W.K. Teo, K. Li, Modified silicone-PVDF composite hollow-fiber membrane preparation and its application in VOC separation, J. Appl. Polym. Sci. 99 (2006) 2497–2503.

[32] H. Paul, C. Philipsen, F.J. Gerner, H. Strathmann, Removal of organic vapors from air by selective membrane permeation, J. Memb. Sci. 36 (1988) 363–372.

Chapter 6 General Conclusion

This thesis aims to provide insights into gas separation membranes using new materials based on covalent organic frameworks. This thesis concludes by summarizing the main results as follows:

In Chapter 2, I evaluate the feasibility of membrane separation for CO_2 separation, especially based on the direct air capture (DAC) process, which has been overlooked. Two systems, vacuum swing and continuous pumping, were considered. The energy efficiency was estimated using classical mixing entropy calculation. The results showed that membranes with CO_2 separation factors greater than 1000 can capture CO_2 with maximum efficiencies of 0.50 GJ/tonCO_2, which is thermodynamically superior to other methods such as adsorption (0.7–50 GJ/ton) and cryogenic (0.8–1.7 GJ/ton). In previous works, membrane separation was considered only for the application of highly concentrated CO_2 sources such as flue gas (CO_2 concentration of ca. 15%). In this chapter, I propose that the membrane process can be applied to DAC if membranes with drastically greater separation factors (ideally over 10000) can be synthesized in the future.

In Chapter 3, I developed a method for synthesizing COF films using alternating vapor deposition polymerization followed by vacuum annealing. My method allows

precise control of the composition and thickness of the COF film, which is difficult to achieve using conventional COF film synthetic methods. It was found that vacuum annealing conditions play an important role in forming the COF network structure. The optimal condition was a relatively short annealing time at high temperatures (400 °C, 10 min), which provided partially oriented pores with entangled networks. The solubility and diffusivity parameters of the COF films were estimated by numerical analysis of CO_2/N_2 permeation measurements. This method is applicable not only to COF films but also to ultrathin films, which makes it difficult to measure the gas sorption directly. The analysis indicated that the greater solubility of CO_2 compared with N_2 in the COF films significantly contributed to the fast permeation of CO_2. I also found that the oriented pore region in the COF films contributed to an increase in CO_2 diffusivity, indicating that if the crystallinity of the COF can be improved, the CO_2 permeability can increase. My careful investigation, combining experimental and theoretical approaches, provided the sophistication of COF films and roadmaps for their CO_2–N_2 separation applications.

In Chapter 4, the crystallization of COF films and their effects on CO_2/CH_4 separation were discussed. Neat crystalline COF films can be synthesized by alternating vapor deposition followed by annealing in an appropriate solvent vapor. The solvent-vapor-annealed COF film exhibited good crystallinity compared to the vacuum-annealed

COF film. The solvent-vapor-annealed film formed an "onion"-like structure without a rolling mode, such as spiral growth, suggesting that the film growth proceeds in a layer-by-layer manner. This result suggests the possibility of arbitrarily controlling the orientation of the COF film when a flat COF monolayer is formed on the substrate. The CO_2/CH_4 separation performance of the COF film was found to be 3.6 times greater than that before solvent vapor annealing. This result indicates that the density of the COF film significantly impacts CO_2/CH_4 separation performance. This study contributes to the experimental confirmation of the correlation between pore orientation and CO_2 permeation performance, i.e., the crystalline COF film is effective for CO_2–CH_4 separation applications.

In Chapter 5, the effect of the functional groups in the COF on the VOC/N_2 separation properties was examined. The fluorinated COF, named after the F-COF film, also exhibited good crystallinity with a layered stacking structure by solvent vapor-induced crystallization. Based on structural analysis combining experiments and simulations, I quantitatively estimated the difference in interlayer stacking patterns between H-COF and F-COF membranes. I found that H-COF films contain ca. 10% AB-stacking, whereas F-COF films contain more than 99% AA-stacking structure. The VOC permeability of the F-COF films was 18–25 times greater than that of N_2, indicating

moderate selectivity of the film for VOC separation. The VOC or N_2 permeability of the F-COF films was greater than that of the H-COF films due to the increased interaction between the gas and COF frameworks by introducing the electron-negative F atom. These results show that COF films can be applied to separating gaseous VOCs and N_2, which have been overlooked in the literature. My research can expand the potential of COF films for various gas separations, such as toxic BF_3, F_2, or hydrocarbons, which are expected to reach future research targets. The VOC/N_2 separation performance of the prepared COF films did not exceed that of conventional polymeric membranes. It is hoped that the structure of the COF can be finely tuned by choosing appropriate precursor molecules to further improve the VOC separation properties.

This thesis obtained two main perspectives: the feasibility of membrane gas separation and the exploration of the gas separation properties of COF films. The former insight indicates the importance of further research focused on improving gas selectivity. Notably, the advancement of gas separation membranes is the realization of DAC using a membrane process. The latter insight clarifies the gas separation function of the new COF film material in detail. My research provides insight into the preparation procedure and improvement of the gas permeation properties, which can apply not only to COF but also to new materials in the future.

Appendix

Publications related to this thesis

[1] Masaki Kato, Teruki Ando, Cho Rong Kim, Seiya Yokokura, Hiroki Waizumi, and Toshihiro Shimada, Thermodynamic efficiency of membrane separation of dilute gas: estimation for CO_2 direct air capture application, J. Membr. Sci. Lett. 4 (2024) 100085. (Chapter 2)

[2] Masaki Kato, Ryo Ota, Takashi Endo, Takashi Yanase, Taro Nagahama, and Toshihiro Shimada, Free-standing nanometer-thick covalent organic framework films for separating CO_2 and N_2, ACS Appl. Nano Mater. 5 (2022) 2367–2374. (Chapter 3)

[3] Masaki Kato, Takashi Yanase, Hiroki Waizumi, Seiya Yokokura, and Toshihiro Shimada, Solvent-vapor-assisted crystallization of covalent organic framework films for CO_2/CH_4 separation, Chem. Lett. 53 (2024) upae191. (Chapter 4)

[4] Masaki Kato, Ryo Ota, Ayaka Kakizawa, Takashi Yanase, Hiroki Waizumi, Seiya Yokokura, and Toshihiro Shimada, Fluorinated covalent organic framework films for efficient VOC/N_2 separation, manuscript in preparation. (Chapter 5)

Other publications

査読付き総説

[1] 加藤 将貴, 柳瀬 隆, 島田 敏宏, 交互蒸着重合法により作製した共有結合性有機構造体自立膜の構造と気体分離機能, 表面と真空, 66 (2023) 393–398.

[2] 加藤 将貴, 柳瀬 隆, 島田 敏宏, 交互蒸着重合法による共有結合性有機構造体 (COF) 膜作製法の開発と CO_2 分離性能の評価, 膜, 48 (2023) 119–125.

Presentations

国内会議

[1] 加藤 将貴, 安藤 輝紀, 和泉 廣樹, 横倉 聖也, 島田 敏宏,「気体透過測定と分子動力学計算を用いたイオン液体膜の CO_2 透過性解析」第８５回応用物理学会秋季学術講演会 (2024)（ポスター）

[2] 加藤 将貴, 和泉 廣樹, 横倉 聖也, 島田 敏宏,「二次元 COF 膜の構造と気体分離機能」日本化学会北海道支部 2024 年夏季研究発表会, (2024)（口頭）

[3] 加藤 将貴, 横倉 聖也, 島田 敏宏,「交互蒸着と溶媒蒸気アニールを用いて作製した二次元共有結合性有機構造体膜の構造」第 8 4 回応用物理学会秋季学術講演会 (2023)（口頭）

[4] 加藤 将貴, 柳瀬 隆, 横倉 聖也, 長浜 太郎, 島田 敏宏,「交互蒸着重合法を用いて作製した共有結合性有機構造体膜の溶媒アニールによる秩序化」第 30 回有機結晶シンポジウム (2022)（口頭）

[5] 加藤 将貴, 柳瀬 隆, 横倉 聖也, 長浜 太郎, 島田 敏宏,「交互蒸着重合法を用いて作製した共有結合性有機構造体膜への溶媒アニールの効果」第 83 回応用物理学会秋季学術講演会 (2022)（口頭）

[6] 加藤 将貴, 柳瀬 隆, 長浜 太郎, 島田 敏宏,「交互蒸着法により作製した共有結合性有機構造体自立膜:構造評価と CO_2 分離機能」2021 年日本表面真空学会学術講演会 (2021)（口頭）

[7] 加藤 将貴, 柳瀬 隆, 長浜 太郎, 島田 敏宏,「交互蒸着法を用いた自立する共有結合性有機構造体膜の作製」第 82 回応用物理学会秋季学術講演会 (2021)（口頭）

[8] 加藤 将貴, 柳瀬 隆, 長浜 太郎, 島田 敏宏,「交互蒸着法を用いた共有結合性有機構造体膜の作製」第 68 回応用物理学会春季学術講演会 (2021)（口頭）

[9] 加藤 将貴、柳瀬 隆、長浜 太郎、島田 敏宏,「交互蒸着法を用いた共有結合性有機構造体（COF)膜の作製」2020 年度日本表面真空学会東北・北海道支部学術講演会 (2021)（口頭）

[10] 加藤 将貴, 柳瀬隆, 長浜太郎, 島田敏宏,「交互蒸着法を用いた共有結合性有機構造体膜の作製」日本セラミックス協会東北北海道支部　北海道地区セミナー (2020)（口頭）

International Conference

[1] Masaki Kato, “Vapor-phase synthesis of crystalline two-dimensional covalent organic framework films”, A3 foresight symposium 2023 (2023). (poster)

[2] Masaki Kato, Takashi Yanase, Seiya Yokokura, Taro Nagahama, and Toshihiro Shimada, ”Development of preparation method of covalent organic framework films using alternating deposition polymerization”, A3 foresight symposium 2022 (2022). (poster)

[3] Masaki Kato, Takashi Yanase, Seiya Yokokura, Taro Nagahama, and Toshihiro Shimada, “Covalent organic framework films synthesized by alternating deposition polymerization: Structure and CO_2/N_2 separation mechanism analysis”, IVC-22 (2022).

(poster)

[4] Masaki Kato, Takashi Yanase, Seiya Yokokura, Taro Nagahama, and Toshihiro Shimada, “Free-standing nanometer-thick covalent organic framework films prepared via alternating deposition polymerization for CO_2/N_2 separation”, ISOME-2022 (2022). (poster)

[5] Masaki Kato, Takashi Yanase, Taro Nagahama and Toshihiro Shimada, “Structural Analysis of Free-standing covalent organic frameworks prepared via alternating deposition for CO_2 separation”, ALC-21 (2021). (poster)

Awards

令和 2 年度　日本表面真空学会東北・北海道支部学術講演会　講演奨励賞
令和 4 年度　日本表面真空学会学術講演会　講演奨励賞 (スチューデント部門)

Acknowledgments

I would like to extend my great thanks to my supervisor, Prof. T. Shimada, for his tremendous support, such as continuous guidance for experiments, writing a paper, and encouraging research. I also appreciate the deputy supervisor of Prof. Y. Hasegawa and Prof. K. Sada who provided valuable insights into this thesis.

I am deeply grateful to Prof. T. Yanase (Toho Univ.), who significantly contributed to the construction of the vapor deposition polymerization system. I also thank Prof. T. Nagahama (Yamaguchi Univ.), Prof. S. Yokokura, and Prof. H. Waizumi who discussed with me to refine the research.

I would like to express my gratitude to N. Clément (LAAS-CNRS) for giving me the opportunity to engage in research on molecular dynamics simulations in France. I am deeply grateful to Dr. S. Grall and Dr. S. Li for their tremendous support during my stay and research in Toulouse.

I would like to thank Mr. R. Ota for STEM observation and analysis. I also thank Prof. T. Endo, Prof. Y. Wang, Dr. T. Yoshizawa, Mr. K. Suzuki, Mr. S. Kimura, Mr. A. Sawa, Mr. S. Harada, and Ms. S. Yoshida who supported to operate the NMR, AFM, FE-SEM, IR, Raman, XRD, SAXS and TEM observations.

Thank you very much to my colleagues in the solid-state chemistry laboratory. I especially appreciate Dr. C. R. Kim and Mr. T. Ando for the vigorous discussions in Chapter 2. I also thank Ms. A. Kakizawa, who searched for optimal experimental conditions in Chapter 5.

Finally, I would like to thank my family for their support and understanding.

2025

Masaki KATO